SANDIA REPORT

SAND2006-4387
Unlimited Release
Printed July 2006

Phase Transformation of "Chem-prep" PZT 95/5-2Nb HF1035 Ceramic Under Quasi-static Loading Conditions

Moo Y. Lee, Stephen T. Montgomery, John H. Hofer, and Diane A. Meier

Prepared by
Sandia National Laboratories
Albuquerque, New Mexico 87185

Sandia is a multiprogram laboratory operated by Sandia Corporation,
a Lockheed Martin Company, for the United States Department of Energy's
National Nuclear Security Administration under Contract DE-AC04-94AL85000.

Issued by Sandia National Laboratories, operated for the United States Department of Energy by Sandia Corporation.

Available to DOE and DOE contractors from
U.S. Department of Energy
Office of Scientific and Technical Information
P.O. Box 62
Oak Ridge, TN 37831

Telephone: (865)576-8401
Facsimile: (865)576-5728
E-Mail: reports@adonis.osti.gov
Online ordering: http://www.osti.gov/bridge

Available to the public from
U.S. Department of Commerce
National Technical Information Service
5285 Port Royal Rd
Springfield, VA 22161

Telephone: (800)553-6847
Facsimile: (703)605-6900
E-Mail: orders@ntis.fedworld.gov
Online order: http://www.ntis.gov/help/ordermethods.asp?loc=7-4-0#online

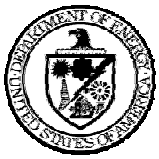

SAND2006-4387
Unlimited Release
Printed July 2006

Phase Transformation of "Chem-prep" PZT 95/5-2Nb HF1035 Ceramic Under Quasi-static Loading Conditions

Moo Y. Lee
Geomechanics Department

Stephen T. Montgomery
NG Design Science and Engineering Department

John H. Hofer, and Diane A. Meier
Geomechanics Department

Sandia National Laboratories
P.O. Box 5800
Albuquerque, NM 87185

ABSTRACT

Specimens of poled and unpoled "chem-prep" PNZT ceramic from batch HF1035 were tested under hydrostatic, uniaxial, and constant stress difference loading conditions at –55, 25, and 75°C. The objective of this experimental study was to characterize the mechanical properties and conditions for the ferroelectric (FE) to antiferroelectric (AFE) phase transformations of this "chem-prep" PNZT ceramic to aid grain-scale modeling efforts in developing and testing realistic response models for use in simulation codes. As seen from a previously characterized material (batch HF803), poled ceramic from HF1035 was seen to undergo anisotropic deformation during the transition from a FE to an AFE phase. Also, the phase transformation was found to be permanent for the two low temperature conditions, whereas the transformation can be completely reversed at the highest temperature. The rates of increase in the phase transformation pressures with temperature were practically identical for both unpoled and poled PNZT HF1035 specimens. We observed that temperature spread the phase transformation over mean stress analogous to the observed spread over mean stress due to shear stress. Additionally, for poled ceramic samples, the FE to AFE phase transformation was seen to occur when the normal compressive stress, acting perpendicular to a crystallographic plane about the polar axis, equals the hydrostatic pressure at which the transformation otherwise takes place.

ACKNOWLEDGEMENTS

The authors would like to acknowledge Thomas Pfeifle and Steven Sobolik for their critical review of this report. The authors also thank Jeffrey Keck for overseeing fabrication of the PNZT specimens.

Table of Contents

Figures

Tables

1. Introduction

Sandia has developed a new process for making PZT 95/5-2Nb ceramic using chemically precipitated, calcined and agglomerated powder (Voigt *et al*., 1999). This niobium-doped lead-zirconate-titanate ceramic (refered to as "PNZT" in this report) serves well as the active electrical element in ferroelectric explosive power supplies (Lysne and Percival, 1975; Bauer *et al*., 1976). Under explosive loading, poled ferroelectric (FE) PNZT transforms to an antiferroelectric (AFE) polymorph, rapidly releasing its bound surface charge and producing pulsed currents and voltages that are very large in magnitude (Fritz and Keck, 1978). An understanding of the electromechanical response and phase transformation of PNZT during complex loading must be understood to design and model shock-wave activated ferroelectric power sources effectively.

The ASC (Advanced Simulation and Computing) project "Grain-Scale Shock Response of PZT 95/5-2Nb Ceramic" is developing microstructural-scale models and codes (Brannon *et al.*, 2001) to accomplish the goal of understanding how the PNZT material is affected by coupled dynamic loading conditions. The pressure-induced FE to AFE phase transformation in "chem-prep" PNZT was investigated for poled and unpoled "chem-prep" ceramics sampled from HF803 and the results are published elsewhere (Lee *et al*., 2003, 2004). The mechanical behavior for each of these formulations was examined in conjunction with the polymorphic phase transformation as a function of mean stress, shear stress, and temperature (Lee *et al*., 2003, 2004).

The stress-strain behavior of "chem-prep" PNZT HF803 under different loading paths was found to be similar to those of "mixed-oxide" PNZT such as HF424 (e.g. Zeuch *et al.*, 1999b). The phase transformation from FE to AFE occurs in unpoled ceramic with an abrupt change in volumetric strain (reduction in volume physically) of about 0.7 % when the maximum compressive stress, regardless of loading paths, equals the hydrostatic pressure at which the transformation takes place. The pressure (P_u^H) required for the onset of phase transformation for unpoled HF803 ceramic with respect to temperature is represented by the best-fit line, P_u^H (MPa) = 227 + 0.76 T (°C). We also confirmed that increasing shear stress lowers the mean stress and the volumetric strain required to trigger phase transformation. The deformation of unpoled HF803 ceramic was seen to be isotropic for all loading conditions not inducing the FE to AFE phase transformation. Under hydrostatic loading conditions the deformation through the phase transformation was also seen to be isotropic. However, under non-hydrostatic loading conditions the deformation of the ceramic through the phase transformation was seen to be anisotropic with the mechanical properties of the ceramic remaining anisotropic after unloading.

Unlike the unpoled HF803 ceramic, in the poled HF803 ceramic the deformation was anisotropic even through the transition from the FE to the AFE phase under hydrostatic loading. This is due to anisotropy induced through poling the ceramic. The lateral strain measured parallel to the poling direction was typically 35 % greater than the strain measured perpendicular to the poling direction. The pressure (P_p^H) required for the onset of phase transformation for the poled HF803 ceramic with respect to temperature is

obtained as P_p^H (MPa) = 261 + 0.74 T (°C). We also observed that the FE to AFE phase transformation occurred in poled ceramic when the normal compressive stress, acting perpendicular to a crystallographic plane about the polar axis, equaled the hydrostatic pressure at which the transformation otherwise took place.

We also found common feature of the mechanical response for both unpoled and poled PNZT HF803 ceramics. The rates of increase in the phase transformation pressures with temperature changes were practically identical (0.76 MPa/°C for unpoled HF803 and 0.74 MPa/°C for poled HF803). Also, at higher temperatures, a spread in the transformation across the mean stress, was seen that was similar to the spread in the transformation with mean stress seen when a shear stress is present. We also found that at the lower bound (-55°C) of the tested temperature range, the phase transformation is permanent and irreversible, whereas, at the upper bound (75°C) of the temperature, the phase transformation is completely reversible as the stress causing phase transformation is removed.

Ceramic from HF803 used in the previous investigations exhibited a pressure-induced FE to AFE phase transformation near the higher limit of desired phase transformation pressures. The thrust of this experimental study was to extend our previous observations to another "chem-prep" PNZT composition which falls near the lower limit for range of desired phase transformation pressure. We selected material from HF1035 which exhibits a phase transformation pressure of 207 MPa (Yang, 2004). Hydrostatic compression (HC) tests were conducted across the FE-AFE boundary to examine the temperature influence on the phase transformation of the HF1035 ceramics. Uniaxial compression (UC) tests were conducted in the same temperature range to observe the superposed strains from dipole switching (Fritz and Keck, 1978; Fritz, 1979) interacting with transformation strains**.** A series of constant-stress-difference (CSD) tests was conducted at two stress differences (50 and 100 MPa) and in a temperature range of -55 to 75°C to investigate the effect of shear stress on the FE to AFE phase transformation.

2. Sample Preparation and Characterization

2.1 Sample material

The PNZT ceramic specimens were produced based on the Transferred Sandia Process (TSP). This is an up-scaled chemical preparation process for the synthesis of PNZT powder (U.S. Patent No. 5,908,802 by Voigt *et al.*, 1999). Figure 1 shows the flow diagram for key steps in the solution synthesis of PNZT.

Calcinated TSP80 powder was mixed with 15 μm Lucite pore former in preparing the material of HF1035. The average density of the material from HF1035 was 7.335 g/cm^3 compared to 7.358 g/cm^3 for HF803. The hydrostatic depoling pressure was found to be 207 (±2) MPa compared to 303 (±2) MPa for HF803. The average charge release was

31.10 (±0.28) μC/cm^2 for HF1035 compared to 31.9 (±0.2) μC/cm^2 for HF803 (Yang, 2003).

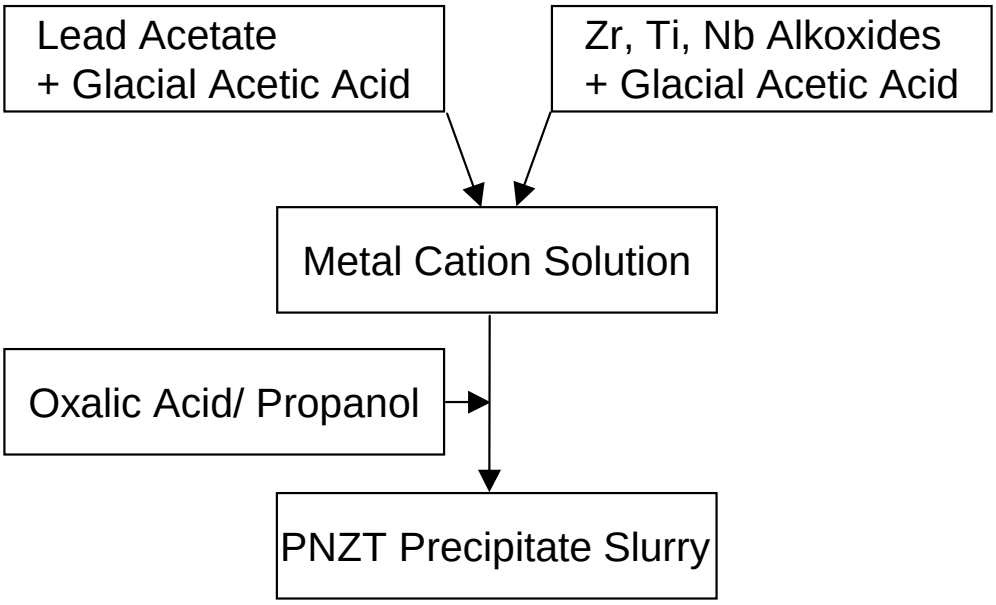

Figure 1. Overview of powder synthesis processing of PNZT (after Voigt *et al.*, 1999, U.S. Patent #5,908,802)

2.2 Sample preparation

Poled and unpoled PNZT samples in the form of rectangular parallelepipeds having nominal dimensions of 10.8 × 10.8 × 25.4 mm were fabricated from slugs of HF1035 material. The dimensions fall within the range of nominal length-to-width ratio (2 to 2.5), which assures uniform stress and strain measured in the middle of the sample. The ends of the specimen were ground flat within 0.003 mm tolerance. All samples were visually inspected for significant flaws and general straightness of the surfaces. The physical dimensions of each specimen are listed in Table 1 with the assigned test types and conditions.

To create the poled PNZT samples for material from HF1035, an electrode silver paste (Dupont 7095) was applied to two opposing rectangular faces of the unpoled specimens. The specimens were then fired at 600^{o}C for approximately 20 minutes. The electroded specimens were removed from the fire and "hot-poled" at 105^{o}C under the electronic bias of 20 KV (Zeuch *et al.*, 1995; Yang *et al.*, 2003), corresponding to an electric field of approximately 2 KV/mm. In the case of the unpoled PNZT samples, a conductive epoxy (CircuitWorks 2400) was spread evenly on two opposing faces of the specimen so that the capacitance across the sample could be measured (Lee *et al.*, 2004).

Table 1. List of mechanical tests conducted for "chem-prep" PNZT-HF1035 ceramic.

Specimen no.	Polarization type	Test type	T (ºC)	σ_1 . σ_3 (MPa)	Length (cm)	Width (cm)	Height (cm)	Weight (g)	Density (g/cm^3)
PNZT-1035-08	Unpoled	HC	-55	0	1.077	1.080	2.539	21.81	7.39
PNZT-1035-05	Unpoled	HC	-35	0	1.080	1.077	2.537	21.74	7.37
PNZT-1035-04	Unpoled	HC	-15	0	1.077	1.080	2.537	21.78	7.38
PNZT-1035-03	Unpoled	HC	5	0	1.078	1.077	2.537	21.73	7.37
PNZT-1035-01	Unpoled	HC	25	0	1.080	1.077	2.540	21.78	7.38
PNZT-1035-09	Unpoled	HC	50	0	1.080	1.077	2.537	21.77	7.38
PNZT-1035-12	Unpoled	HC	75	0	1.077	1.080	2.537	21.82	7.40
PNZT-1035-11	Unpoled	UC	-55	σ_1	1.080	1.080	2.540	21.67	7.32
PNZT-1035-13	Unpoled	UC	25	σ_1	1.077	1.080	2.537	21.82	7.40
PNZT-1035-17	Unpoled	CSD	-55	50	1.077	1.080	2.537	21.82	7.40
PNZT-1035-18*	Unpoled	CSD	-55	100	1.078	1.077	2.537	21.80	7.40
PNZT-1035-15	Unpoled	CSD	25	50	1.078	1.076	2.537	21.69	7.37
PNZT-1035-16*	Unpoled	CSD	25	100	1.077	1.078	2.537	21.79	7.40
PNZT-1035-19	Unpoled	CSD	75	50	1.077	1.080	2.536	21.77	7.38
PNZT-1035-20*	Unpoled	CSD	75	100	1.080	1.080	2.537	21.82	7.38
PNZT-1035-33	Poled	HC	-55	0	1.082	1.078	2.539	21.85	7.38
PNZT-1035-32	Poled	HC	-35	0	1.082	1.077	2.537	21.82	7.38
PNZT-1035-30	Poled	HC	-15	0	1.082	1.080	2.537	21.84	7.37
PNZT-1035-29	Poled	HC	5	0	1.083	1.080	2.537	21.79	7.34
PNZT-1035-31	Poled	HC	25	0	1.080	1.078	2.537	21.82	7.39
PNZT-1035-34	Poled	HC	50	0	1.082	1.080	2.537	21.81	7.36
PNZT-1035-35	Poled	HC	75	0	1.083	1.078	2.540	21.81	7.35
PNZT-1035-38	Poled	UC	-55	σ_1	1.083	1.080	2.527	21.80	7.38
PNZT-1035-37	Poled	UC	25	σ_1	1.083	1.080	2.539	21.79	7.34
PNZT-1035-39	Poled	UC	75	σ_1	1.083	1.077	2.527	21.80	7.39
PNZT-1035-45	Poled	CSD	-55	50	1.080	1.080	2.536	21.81	7.38
PNZT-1035-46*	Poled	CSD	-55	100	1.082	1.074	2.537	21.73	7.37
PNZT-1035-44	Poled	CSD	25	50	1.083	1.080	2.537	21.81	7.35
PNZT-1035-43	Poled	CSD	25	100	1.083	1.080	2.537	21.68	7.31
PNZT-1035-47	Poled	CSD	75	50	1.082	1.078	2.537	21.82	7.37
PNZT-1035-48	Poled	CSD	75	100	1.085	1.080	2.537	21.81	7.34

T-Temperature

HC-Hydrostatic Compression ; UC-Uniaxial Compression; CSD-Constant Stress Difference

σ_1-maximum principal stress (axial stress); σ_3-minor principal stress (confining pressure)

*-Incipient phase transformation before reaching the preset 100 MPa stress difference.

A typical instrumented specimen is shown in Figure 2a. Two orthogonal sets of axial and lateral strain gages were mounted at mid-height on opposite sides of the specimen (180^{o} apart). The axial and lateral gages were oriented to be parallel and perpendicular to the axis of the specimen, respectively. The instrumented specimens with strain gages were placed between upper and lower silicon carbide (SiC-N) end-caps. The specimen assemblies were coated with an approximately 1-mm thick impervious polyurethane membrane. The flexible membrane allowed the confining pressure to be applied uniformly to the surfaces of the specimen and at the same time, it prevented the confining fluid from infiltrating the specimen. To maintain uniform thickness of the membrane, the specimen was rotated in a lathe while the membrane cured. The specimen was aligned such that the centerline of the long axis of the assembly was oriented parallel with the axis of rotation of the lathe (Lee *et al.*, 2004).

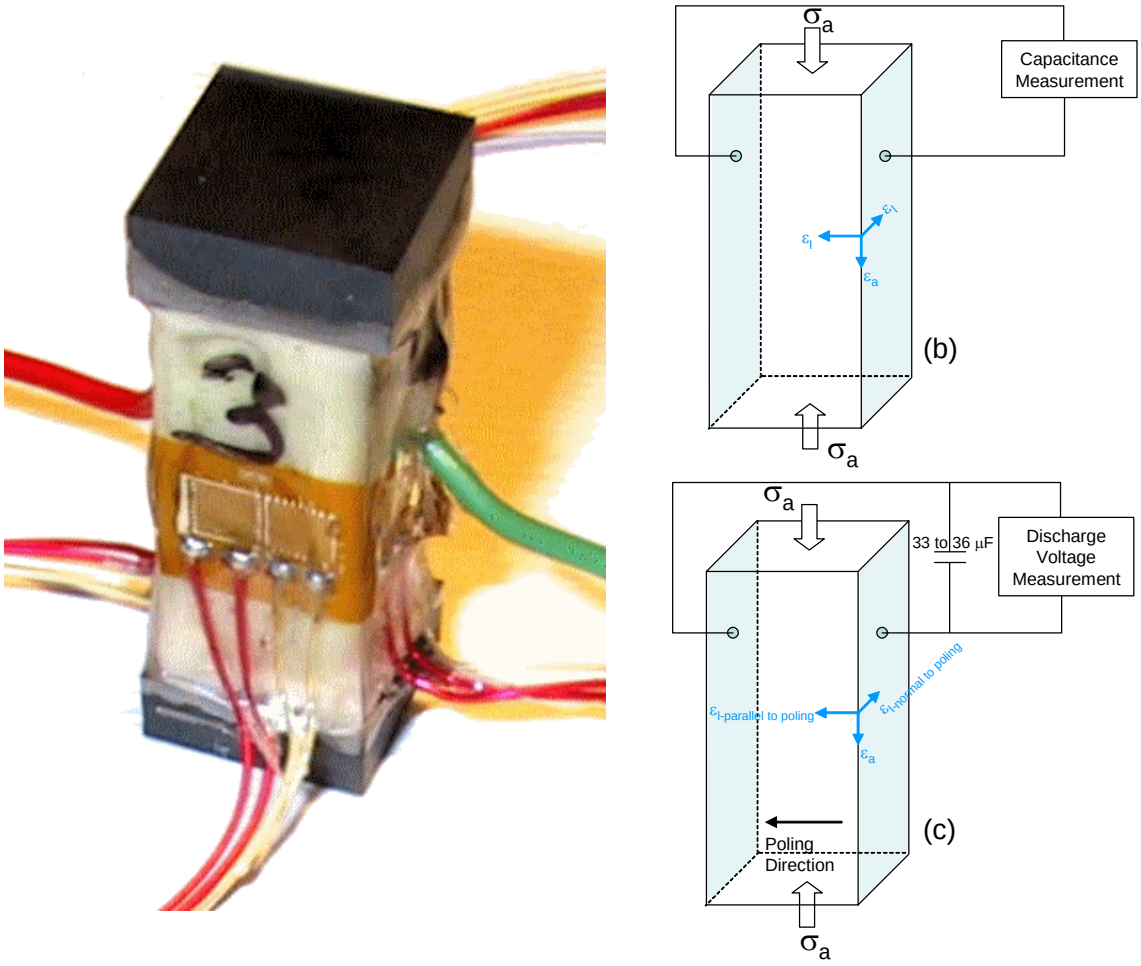

Figure 2. A typical poled "chem-prep" PNZT specimen instrumented with two pairs of axial and lateral strain gages. The specimen is placed between two silicon carbide (SiC-N) end-caps and the assembly is coated with a polyurethane membrane to prevent the confining fluid from infiltrating into the specimen (a); Configuration of strain gages and capacitance measurements for unpoled specimen (b); Configuration of strain gages with respect to poling direction and measurement of discharge voltage for poled specimen (c).

For unpoled specimens (Figure 2b), strains were measured in axial and lateral directions. For poled specimens (Figure 2c), additional strain gages were mounted on the electroded faces of the specimen, enabling measurements of lateral strain normal ($\varepsilon_{l\ -\ \text{normal to poling}}$) to, as well as parallel ($\varepsilon_{l\ -\ \text{parallel to poling}}$) with the poling direction. The discharge voltage that occurs during the phase transformation was measured using the circuitry shown in Figure 2c (Zeuch *et al.*, 1995). The charge release from the specimen was drained to a capacitor where the stored voltage was measured. The confining pressure was measured using a pressure transducer mounted on the hydraulic line used to pressurize the hydraulic fluid in the vessel. In addition, capacitance changes were also measured perpendicular to the loading direction to detect any dimensional changes due to dipole reorientation.

2.3 Experimental set-up and procedure

An externally cooled High-Pressure Low-Temperature (HPLT) triaxial pressure vessel (Zeuch *et al.*, 1999c) was used to examine responses of the PNZT HF1035 ceramic specimens under hydrostatic and constant stress difference conditions. The same triaxial pressure vessel has been used to characterize other materials such as ALOX (alumina-loaded Epoxy) and frozen soil (Lee *et al.*, 2002). The pressure vessel was composed of HF9-4-20 alloy steel and equipped with twelve coaxial feed-throughs. The vessel is capable of operating at a temperature range of -65 to 150°C and confining pressures up to 500 MPa. Figure 3 shows the schematic of the instrumented PNZT specimen with the HPLT triaxial pressure vessel. Owing to the extreme operating conditions in pressure and in temperature and the likelihood of high piston-seal friction, internal load and strain measurements were made.

To achieve the lower testing temperatures, the pressure vessel was externally cooled by circulating liquid nitrogen through conduits mounted on the outside of the vessel. Elevated testing temperatures were obtained through the use of an internal heating coil that surrounded the specimen. Internal data collected during testing consist of pressure, axial and lateral strains, temperature, the axial load on the specimen, discharge voltage for the poled specimens, and the capacitance variation for the unpoled specimens. The data were transmitted from the internal transducers to the external data acquisition system via electrical leads connected to coaxial feed-throughs.

For uniaxial compression experiments, an environmental chamber was added to a 0.1 MN servo-controlled loading machine (Figure 4). The temperature changes in the chamber were controlled by heating elements and a forced circulation of liquid nitrogen. The thermocouple, placed inside the chamber close to the specimen, constantly measured the air temperature and provided feedback signal to the temperature controller. Two through-wall ports, opened in the vertical direction of the chamber, accommodated the loading pistons.

The instrumented specimen (Figure 2a) was placed between the upper and lower loading pistons and loaded until it failed. The axial and lateral deformations were measured from a pair of axial and lateral strain gages, respectively. A pair of acoustic transducers measured changes of P-wave velocities perpendicular to the loading direction. The data acquisition system for measuring P-wave velocities was based on an 8-bit wave-form digitizer at sampling rates up to 5×10^9 samples/s.

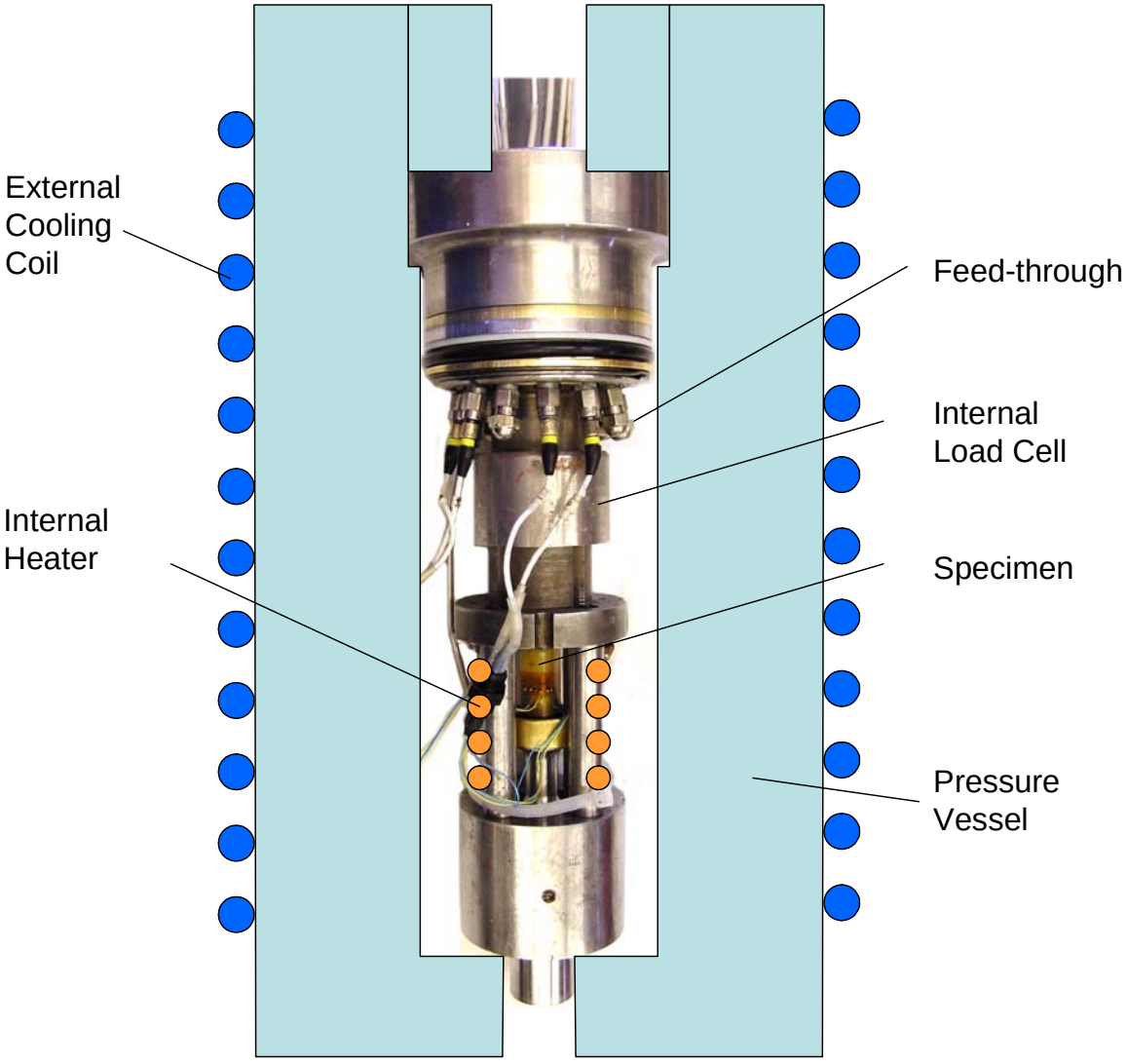

Figure 3. Externally cooled High-Pressure-Low-Temperature (HPLT) cell and an assembly of PNZT specimen.

Figure 4. A uniaxial compression test set-up consisting of a 0.1 MN load-frame and environmental chamber for temperature control.

2.3 Test types and loading paths

Three different loading paths were used to characterize the poled and unpoled ceramic samples from HF1035: hydrostatic compression (HC), uniaxial compression (UC), and constant stress difference (CSD). Figure 5 shows the appropriate loading path for each testing condition in terms of the maximum (σ_1) and the minimum (σ_3) principal stresses, respectively. A Mohr diagram is used to show variations of mean stress (the center of the Mohr circle) and shear stress (the radius of the Mohr circle) for each test condition. In this report, the so called "rock mechanics sign convention" is used. That is, forces are reckoned positive when compressive (Jaeger and Cook, 1979). For the HC loading condition, the principal stresses were all equal, but simultaneously increasing ($\sigma_1 = \sigma_2 = \sigma_3 = \mathbf{P}$). The dashed line, denoted HC, in Figure 5 shows the stress path for the hydrostatic compression test. As shown in the Mohr diagram for HC, there is no difference between

σ_1 and the mean stress σ_m. During HC testing, σ_m is increased while τ (the shear stress) is suppressed. For the UC loading condition, the axial stress was applied along the long axis of the specimen without a confining pressure ($\sigma_2 = \sigma_3 = \mathbf{P} = 0$) until the specimen failed. The loading path of the uniaxial compression (UC) test is shown as the thick vertical line denoted UC in Figure 5. In UC testing, both σ_m and τ increase as the test progresses. For the constant stress difference (CSD) loading condition, the specimen was initially loaded hydrostatically to a target mean stress less than the expected phase transformation pressure. Then, the stress difference $\sigma_1 - \sigma_3 = \sigma_d$ was created by increasing σ_1 while the confining pressure was held constant. Once the targeted σ_d is reached, the axial stress (σ_1) and the confining pressure ($\sigma_2 = \sigma_3 = \mathbf{P}$) were raised at the same rate to maintain σ_d as constant. The CSD loading path is represented by a thin solid line denoted CSD in Figure 5. In the CSD test condition, σ_m is increased while τ is held constant. By running multiple tests with different σ_d values, effects of τ on the phase transformation can be studied.

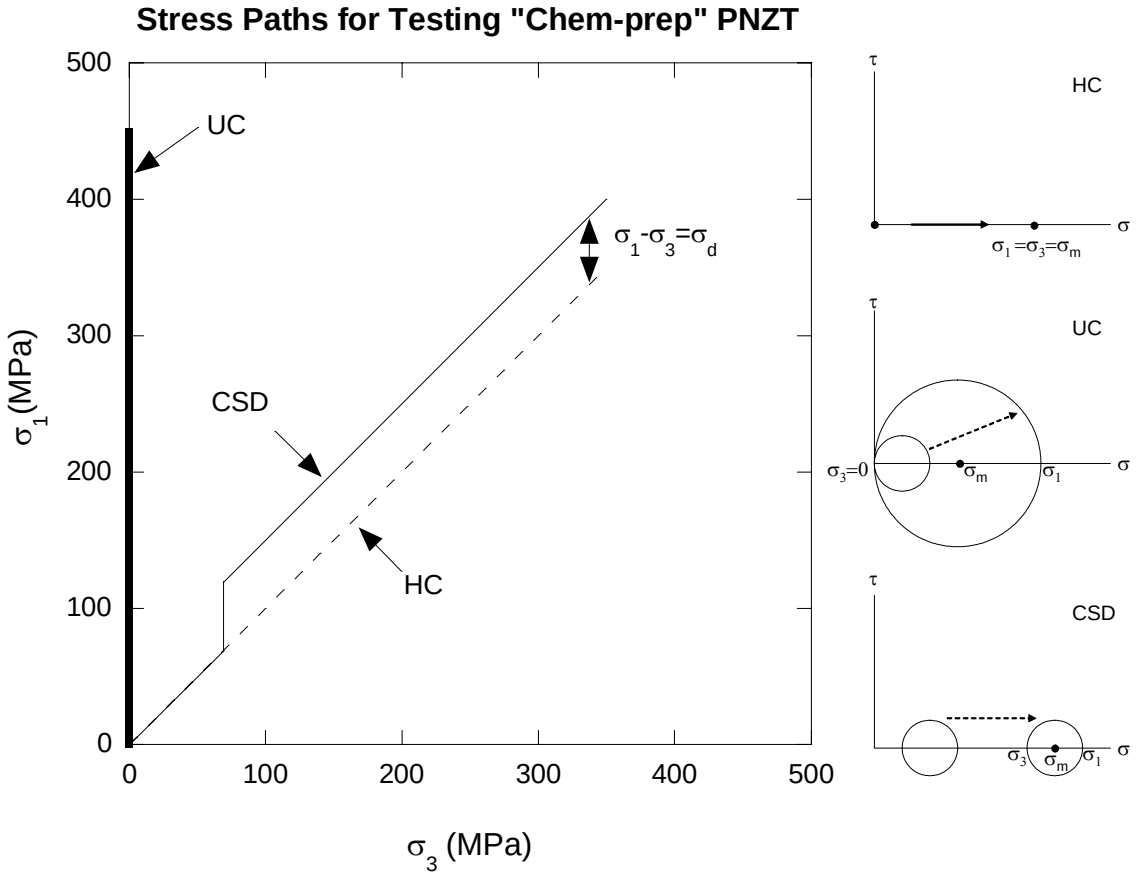

Figure 5. Three quasi-static loading paths, designed for characterization of the electro-mechanical responses of the "chem-prep" PNZT, are shown in the principal stress domain (UC for Uniaxial Compression, HC for Hydrostatic Compression, and CSD for Constant Stress Difference). The stress difference (σ_d) is shown as the difference between the axial stress (σ_1) and the confining pressure ($\sigma_2 = \sigma_3 = \mathbf{P}$). The stress conditions are also shown in the Mohr diagram.

3. Experimental characterization of unpoled "chem-prep" HF1035 ceramic

3.1 Hydrostatic compression test

The mechanical behavior of unpoled "chem-prep" PNZT under hydrostatic loading was studied using a pressure (P)-volumetric strain (ε_v) plot. The test records for all tested specimens are shown in Appendix A. The hydrostatic pressure ($\sigma_1=\sigma_2=\sigma_3=P$) was applied at a constant rate (~0.69 MPa/s) up to 500 MPa. At a specific hydrostatic pressure (P_u^H)[1], the PNZT ceramic undergoes a phase transformation from a FE rhombohedral perovskite structure to an AFE orthorhombic structure. The first segment of the P- ε_v plot, defined by a straight line with a bulk modulus of K_F as a slope, represents the mechanical behavior of PNZT in the FE phase (Figure 6). This linear increase of ε_v as a function of P continues until the hydrostatic pressure reaches the critical phase transformation pressure P_u^H and the corresponding volumetric strain ε_{vu}^H. The critical pressure of the phase transformation is marked by a sudden increase in volumetric strain (or reduction in volume), shown as a nearly horizontal line, by 0.7 to 0.8%. After completion of FE to AFE phase transformation, P-ε_v plot show a rather straight line with a bulk modulus K_A as a slope in the AFE phase.

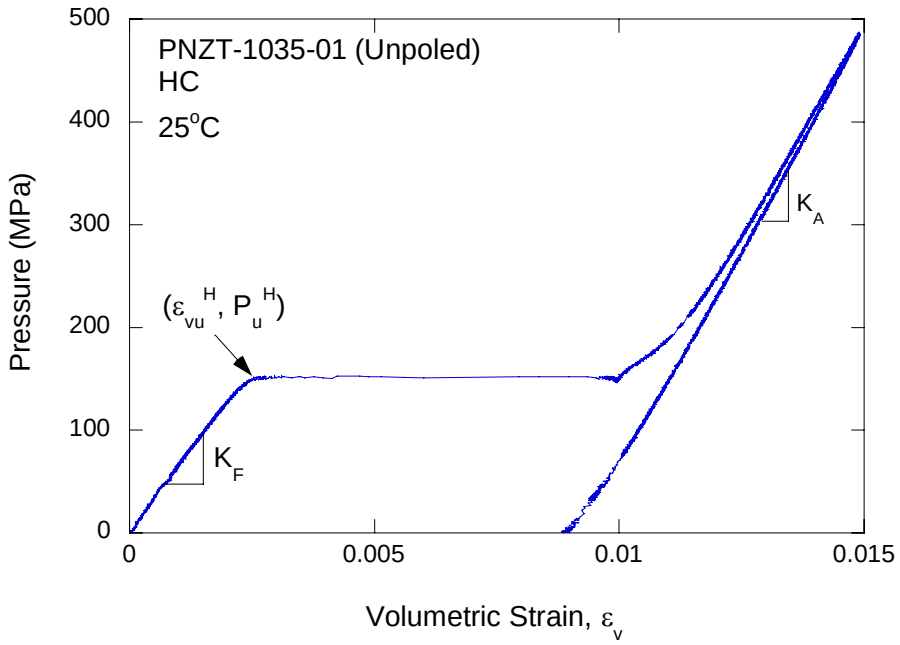

Figure 6. Quantitative description of phase transformation in unpoled "chem-prep" PNZT under hydrostatic loading. Initiation of phase transformation is represented by the point shown by the volumetric strain ε_{vu}^H and P_u^H. K_F represents the bulk modulus of the ceramic in FE phase and K_A represents the bulk modulus of the ceramic in AFE phase.

[1] We use a subscript **u** or **p** to represent phases describing the unpoled or poled ceramic and a superscript **H**, **U**, or **CSD** to denote the type of test (HC, UC, or CSD as described previously).

Hydrostatic compression experiments, carried out on unpoled PNZT ceramic from HF1035, were performed across the FE-AFE boundary in approximately 20°C increments within the temperature range of -55 to 75°C and the maximum pressure up to 500 MPa. Figure 6 shows a typical record obtained at an ambient temperature of 25°C. The unpoled PNZT HF1035 underwent a distinct FE to AFE transformation at a hydrostatic pressure of approximately 151 MPa.

Figure 7 shows a typical record obtained from a specimen for PNZT-1035-12 at an elevated temperature of 75°C. At this temperature, the transition from the FE to the AFE phase in PNZT is rather gradual compared to the transition at the ambient and lower temperatures. To help assist in identifying the phase transformation; we also used capacitance measurements across two randomly chosen opposing faces of the specimen. For unpoled ceramic, no directional properties exist. Therefore, two randomly chosen opposing surfaces should yield the same capacitance changes if the distances between those two faces are approximately equal. Figure 7 indicates that the transformation pressure, P_u^H, determined from the volumetric strain is identical to that from the capacitance measurement. Upon depressurization, the volumetric strain was partially recovered on unloading indicating that at elevated temperatures, the phase transformation is reversible (a transformation from the AFE phase to the FE) when the applied hydrostatic pressure was removed. The AFE to FE phase transformation on unloading is shown again as a reduction in volumetric strain (increase in volume) in the P-ε_v plot but occurs at a lower pressure than the FE to AFE transition on loading. At low to ambient temperatures (e.g. Figure 6), the FE to AFE transformation was locked in and the "chem-prep" PNZT ceramic did not revert to the FE phase even after the hydrostatic pressure that had caused the FE to AFE transformation was removed. All P- ε_v test plots of the seven unpoled ceramics tested are shown in Appendix A1.

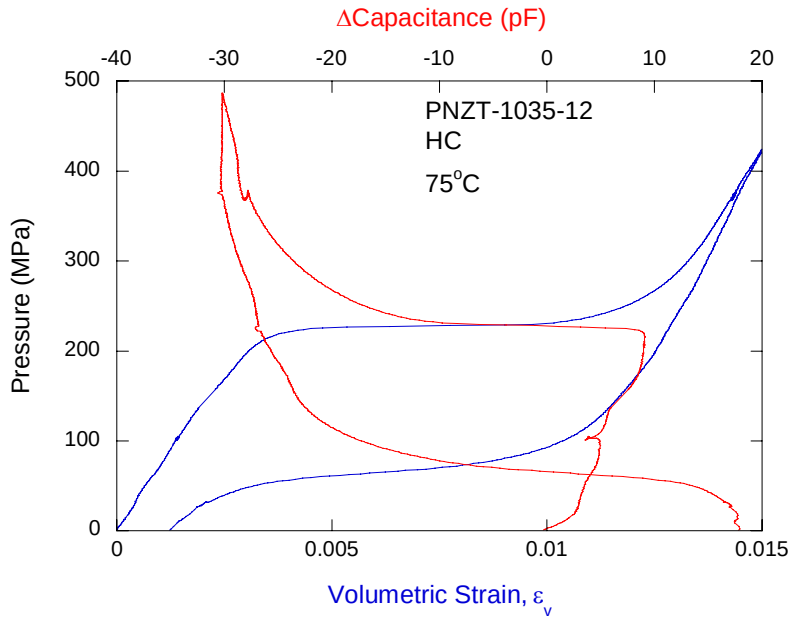

Figure 7. Pressure versus Volumetric Strain and Pressure versus Capacitance Change plots obtained during hydrostatic compression of PNZT HF1035-12 at an elevated temperature of 75°C.

Variation of pressure required for the onset of the FE to AFE phase transformation was seen to depend on temperature. As shown in Figure 8, the phase transformation pressure increases as the temperature increases. Variation of P_u^H with respect to temperature is well represented by a second-order polynomial function of temperature. The best-fit regression curve is:

$$P_u^H \text{ (MPa)} = 130 + 0.84\ T\ (^oC) + 0.0051\ T^2(^oC) \qquad (1)$$

where the phase transformation pressure P_u^H is in MPa and T is temperature measure using the Celsius scale.

The curved shape of the phase boundary shown in Figure 9 corroborates well with the previous findings in "mixed-oxide" ceramic in the phase diagram (Fritz and Keck, 1978). While there was an observed decrease in the bulk moduli with increasing temperature in HF803 ceramics (Lee *et al.*, 2003), no significant variation in K_A or K_F with temperature in HF1035 ceramic (Figures 10 and 11) was seen. If the data from the apparent outliers at -55ºC in FE phase and -55ºC and -35ºC in AFE phase are discarded, the bulk moduli can be represented as follows.

$$K_F \text{ (GPa)} = 68.7 \pm 2.3 \text{ (GPa)}$$
$$K_A \text{ (GPa)} = 90 \pm 2.2 \text{ (GPa)} \qquad (2)$$

A detailed quantitative description of phase transformation in the unpoled PNZT-HF1035 ceramics under hydrostatic loading is summarized in Table 2.

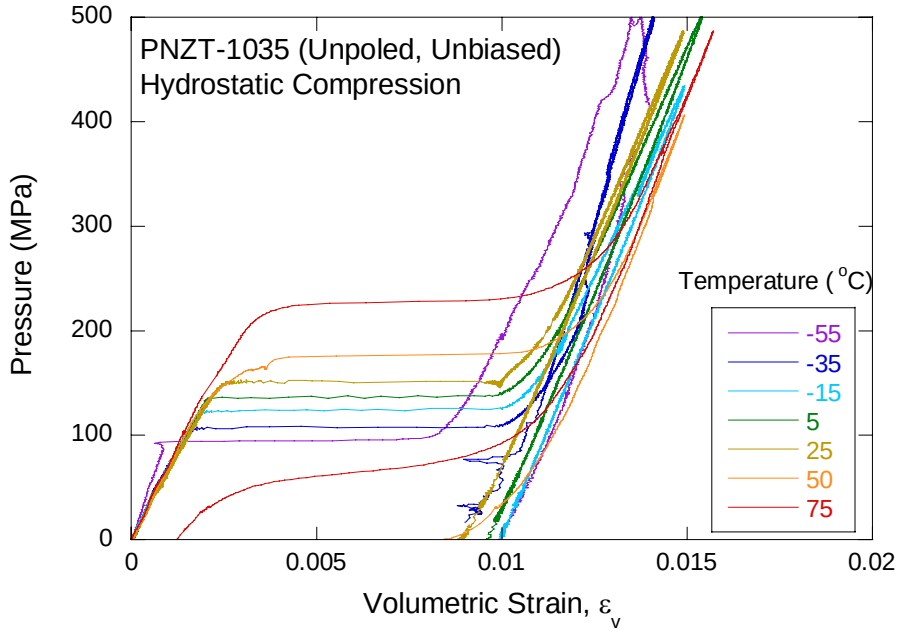

Figure 8. Superimposed pressure versus volumetric strain (ε_v) plots for the hydrostatic compression tests on unpoled PNZT-HF1035 specimens at temperatures ranging from –55 to 75ºC.

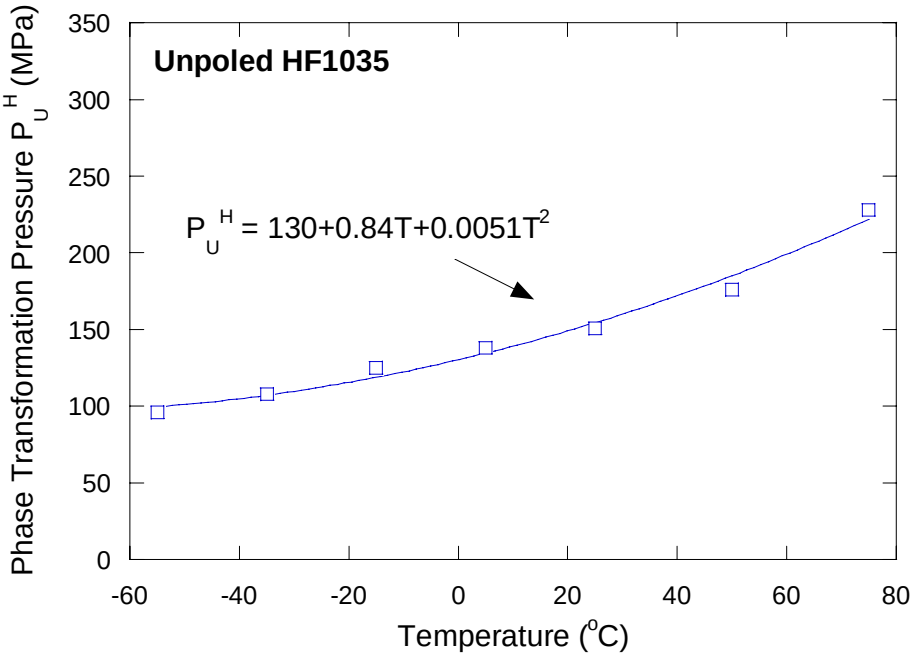

Figure 9. Phase boundaries of unpoled "chem-prep" PNZT HF1035 ceramic at temperatures ranging from -55 to 75°C and pressures 100 to 230 MPa (P_u^H – Phase transformation pressure under hydrostatic compression for unpoled PNZT HF1035).

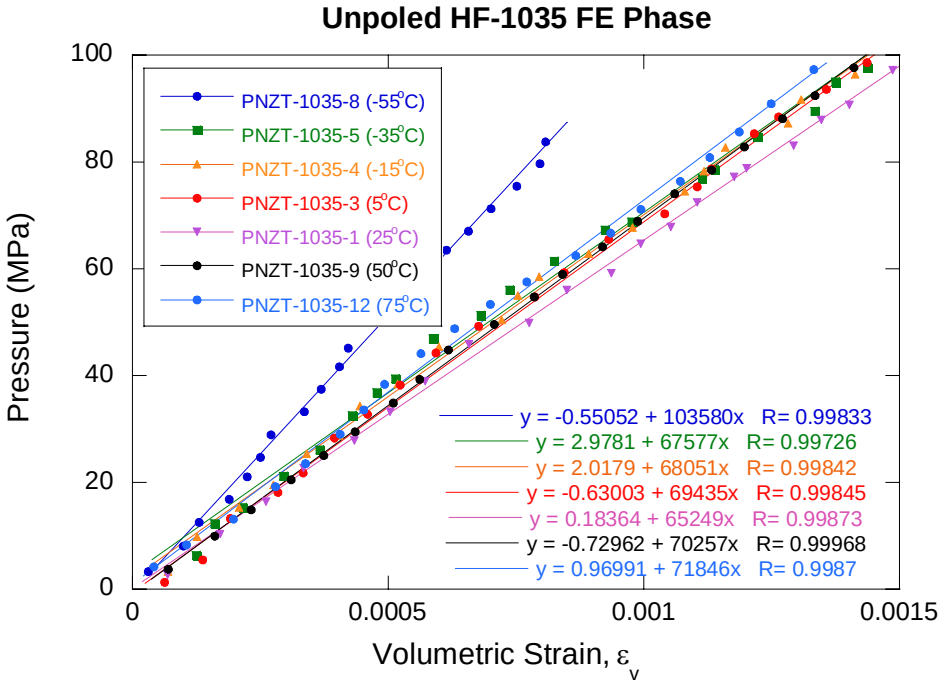

Figure 10. Bulk modulus of unpoled "chem-prep" PNZT HF1035 ceramic in the FE phase obtained from linear fits to the pressure versus volumetric strain (ε_v) prior to the onset of the transformation to the AFE phase.

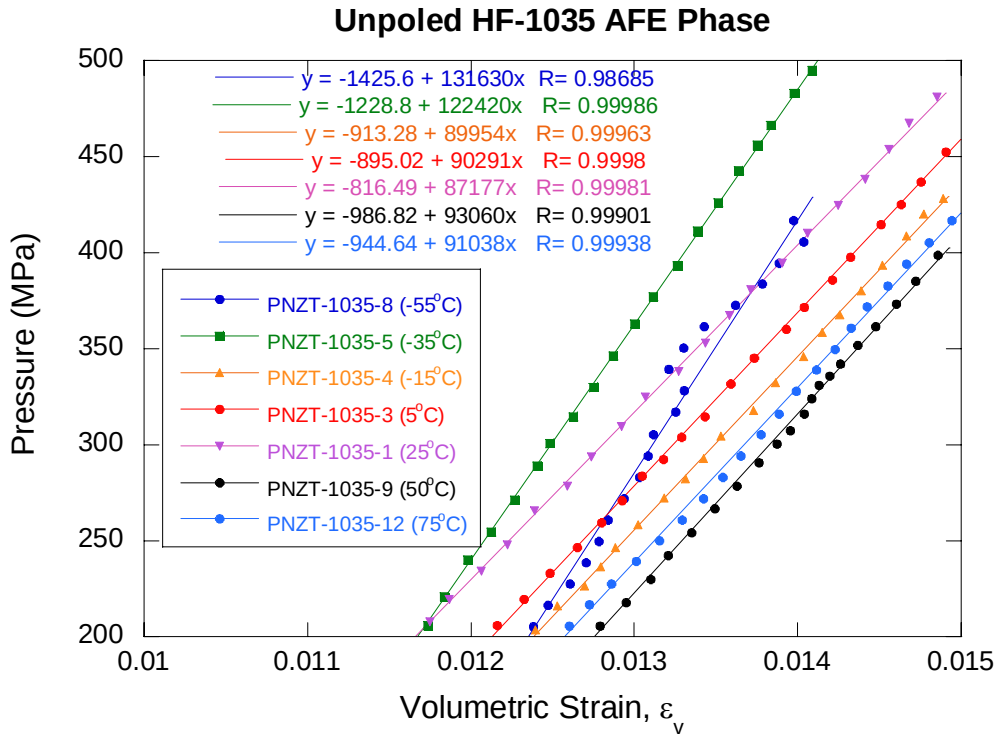

Figure 11. Bulk modulus of unpoled "chem-prep" PNZT HF1035 ceramic in the AFE phase obtained from linear fits to the pressure versus volumetric strain (ε_v) curve after the transformation to the AFE phase.

Table 2. Summary of hydrostatic compression (HC) tests on unpoled "chem-prep" PNZT-HF1035.

Specimen no.	Polarization	Temperature (°C)	K_F (GPa)	K_A (GPa)	ε_{vu}^H	P_u^H (MPa)
PNZT-1035-08	Unpoled	-55	NA	NA	0.0007	96
PNZT-1035-05	Unpoled	-35	68	122	0.0017	108
PNZT-1035-04	Unpoled	-15	68	90	0.0019	125
PNZT-1035-03	Unpoled	5	69	90	0.0021	138
PNZT-1035-01	Unpoled	25	65	87	0.0026	151
PNZT-1035-09	Unpoled	50	70	93	NA	176
PNZT-1035-12	Unpoled	75	72	91	0.0037	228

K_F - bulk modulus in FE (ferroelectric) phase

K_A - bulk modulus in AFE (antiferroelectric) phase

P_u^H - pressure for FE to AFE phase transformation in unpoled ceramic under hydrostatic compression

ε_{vu}^H - volumetric strain in unpoled ceramic at P_u^H

3.2 Unconfined uniaxial compression test

To study the effect of the maximum principal stress (σ_1) on the FE to AFE phase transformation in unpoled "chem-prep" PNZT HF1035 ceramic, we carried out two uniaxial compression (UC) tests at temperatures of -55 and 25°C. The specimens were prepared in the identical parallelepiped shape using the same specifications outlined for the hydrostatic compression (HC) specimens.

In UC tests, the axial strain, ε_a, and the lateral strain, ε_l, were measured from two pairs of axial and lateral strain gages. In addition, capacitance changes were measured between the randomly chosen two opposing faces of the specimen in order to determine the axial stress, $\sigma_{U1}{}^{U}$, required for the FE to AFE phase transformation under a uniaxial stress condition. In addition, the P-wave velocities (Fritz, 1979) normalized to the baseline P-wave velocity measurement for the unstrained PNZT ceramic were also measured to observe a possible domain orientation in the FE phase before the AFE phase is reached. A typical UC experiment conducted on unpoled PNZT HF1035 ceramic is shown in Figures 12 and 13. The test records from all UC tests are shown in Appendix B-1.

Our uniaxial compression tests based on stress-strain plots show nonlinear behavior before the phase transformation at $\sigma_{U1}{}^{U}$. At ambient temperature, the FE to AFE phase transformation was gradual. The capacitance measurement gave similar indication of FE-AFE phase transformation observed in strain measurement. The normalized P-wave velocity measurement did not give a clear indication of dipole reorientation due to imbedded scatter in the measurement itself. There was no obvious indication of dipole reorientation in the stress-strain, stress-capacitance, and stress-normalized P-velocity plots. Table 3 summarizes two uniaxial compression tests at two different temperatures. As the temperature increased from -55º to 25ºC, $\sigma_{U1}{}^{U}$ increased about 5%. This rate was slightly smaller than the rate observed in $P_U{}^{H}$ under HC condition. The maximum stress, $\sigma_{U1}{}^{U}$, required for phase transformation under uniaxial compression agreed well with $P_U{}^{H}$, the FE to AFE phase transformation pressure, measured under HC condition. However, the mean stress, $\sigma_{Um}{}^{U}$, required for FE to AFE phase transformation under uniaxial loading condition was about one third of $P_U{}^{H}$.

$$\sigma_{U1}{}^{U} (\equiv 3\sigma_{Um}{}^{U}) \approx P_U{}^{H} \qquad (3)$$

Thus, the phase transformation in unpoled PNZT ceramic occurs when the maximum principal stress is approximately equal to the phase transformation pressure required under the hydrostatic loading condition.

Table 3. Summary of phase transformation in unpoled "chem-prep" PNZT-HF1035 under uniaxial compression (UC).

Specimen no.	Polarization	Temperature (ºC)	σ_{U1}^{U} (MPa)	σ_{Um}^{U} (MPa)	P_U^H (MPa)
PNZT-1035-11	Unpoled	-55	95	32	96
PNZT-1035-13	Unpoled	25	143	48	151

σ_{U1}^{U} - maximum stress required for FE to AFE phase transformation of unpoled ceramic under uniaxial compression

σ_{Um}^{U} - mean stress required for FE to AFE phase transformation of unpoled ceramic under uniaxial compression

P_U^H - FE to AFE phase transformation pressure of unpoled ceramic under hydrostatic compression

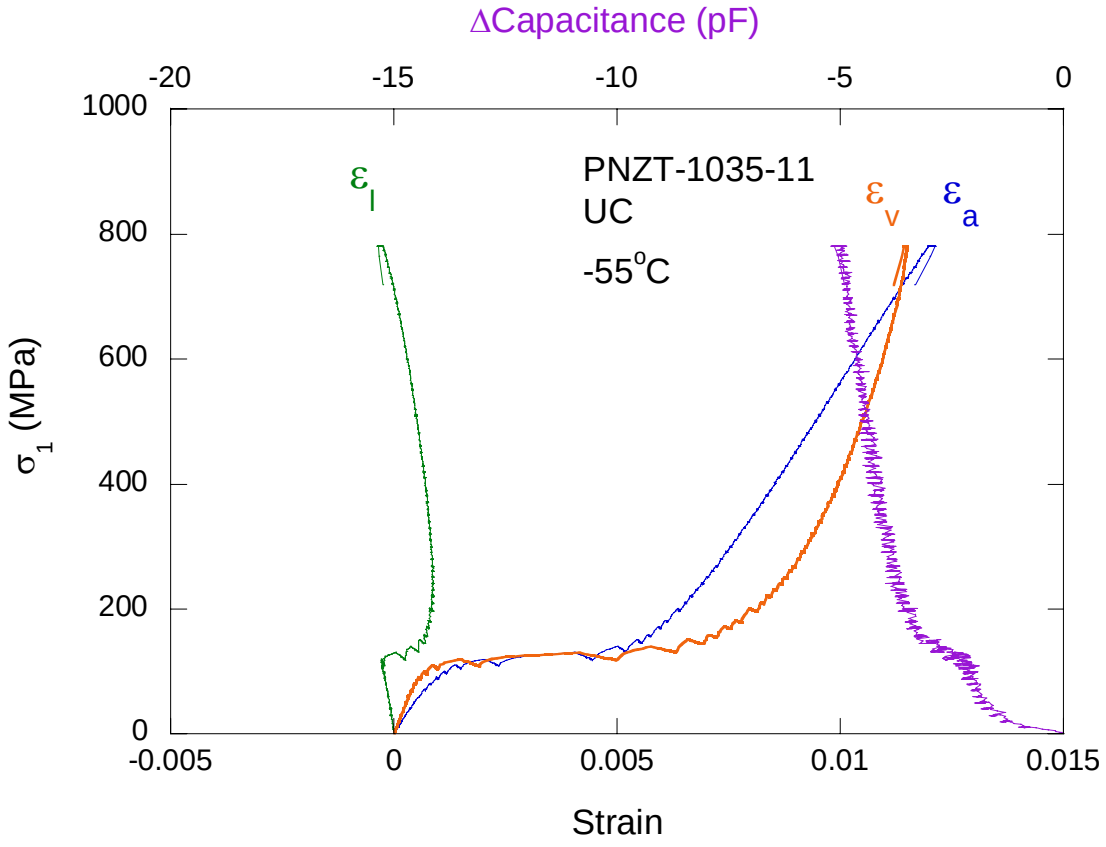

Figure 12. Typical uniaxial compression test with strain and capacitance measurements conducted on an unpoled "chem-prep" PNZT HF1035-11 specimen at -55°C.

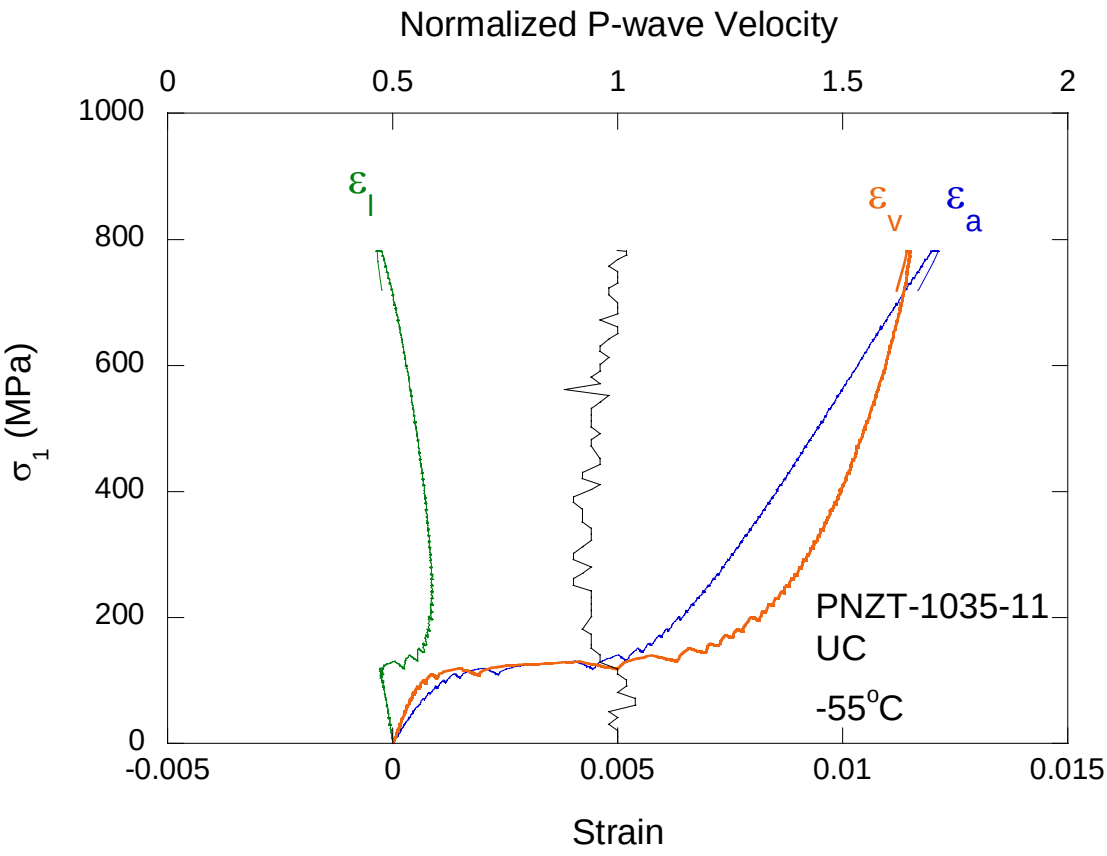

Figure 13. Typical uniaxial compression test with strain and normalized P-wave velocity measurements conducted on an unpoled "chem-prep" PNZT HF1035-11 specimen at -55°C.

3.3 Constant stress difference test

To characterize the effect of shear stress on the phase transformation of "chem-prep" PNZT ceramic from HF1035, a series of Constant-Stress-Difference (CSD) tests (Zeuch *et al.*, 1999a) was conducted for two stress differences: 50 and 100 MPa. In addition, the result from the HC tests was used as a baseline (σ_d=0) of the CSD test. These stress differences were applied for three different temperatures: -55, 25, and 75°C. The specimens were prepared according to the same procedure and specifications for preparing the HC and UC specimens as described in previous sections.

A typical loading path for the CSD test is shown in Figure 14. The PNZT-1035-15 specimen was hydrostatically compressed, then confining pressure was held constant and the axial stress was increased to create 50 MPa stress difference. After the stress difference of 50 MPa was created both σ_1 and σ_3 were raised at the same rate, up to about 300 MPa, past the expected phase transformation pressure. The unloading was taken following the exact reverse path used for loading. Appendix C shows the loading paths and stress-strain plots for the CSD testing.

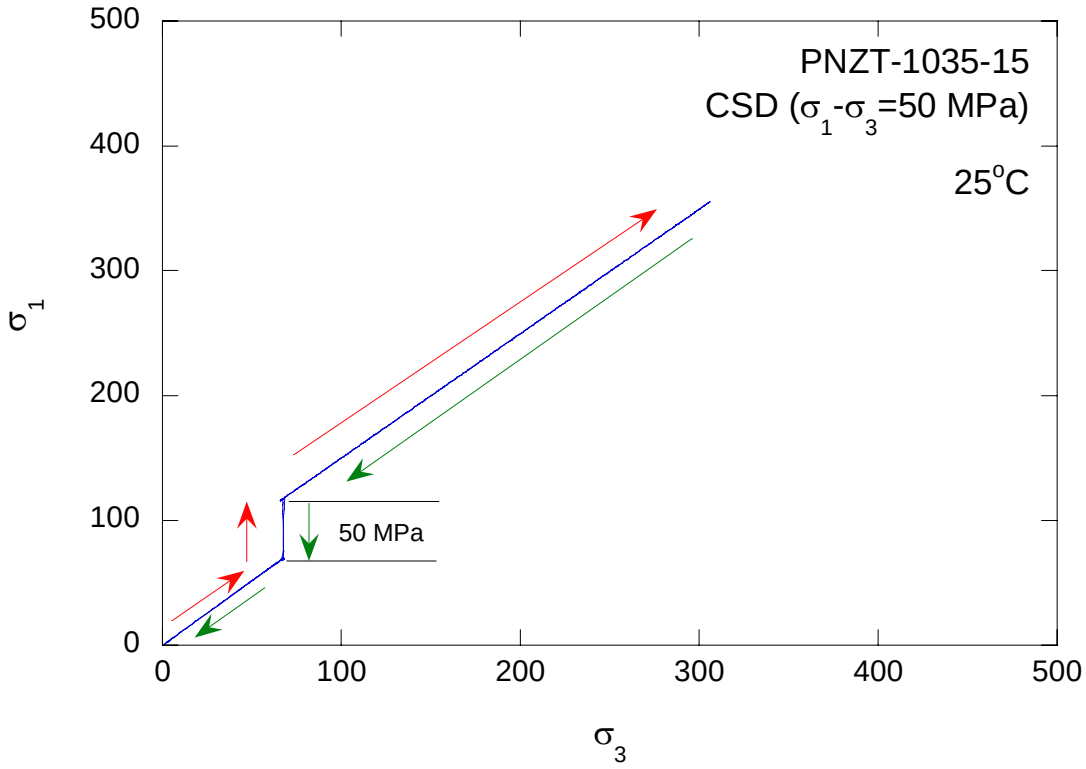

Figure 14. A loading path obtained from the Constant Stress Difference (CSD) test PNZT-1035-15 conducted at 50 MPa stress difference ($\sigma_d=\sigma_1-\sigma_3$). The unloading path is not discernable from the loading path since the unloading path exactly followed the loading path in reverse direction.

Figures 15 and 16 show the complete σ_1-ε and σ_3-ε plots obtained from PNZT-1035-15 experiment, respectively. As in the HC tests, the phase transformation is indicated as an abrupt increase in strains approximately at 168 MPa of σ_1 or 118 MPa of σ_3.

For a low temperature CSD test (PNZT-1035-18), we observed phase transformation before the set σ_d (=100 MPa) was reached. Figure 17 shows incipient phase transformation just after the axial stress is increased to create the stress difference but before the set σ_d was created. The incipient phase transformation is indicated as an abrupt increase in the axial strain (or sudden shrinkage in the specimen length) before σ_d reaches the planned 100 MPa. The test record from the incipient phase transformation are also listed in Appendix C-1 but the data are not analyzed for studying effects of shear stress on the phase transformation in unpoled PNZT HF1035 ceramic.

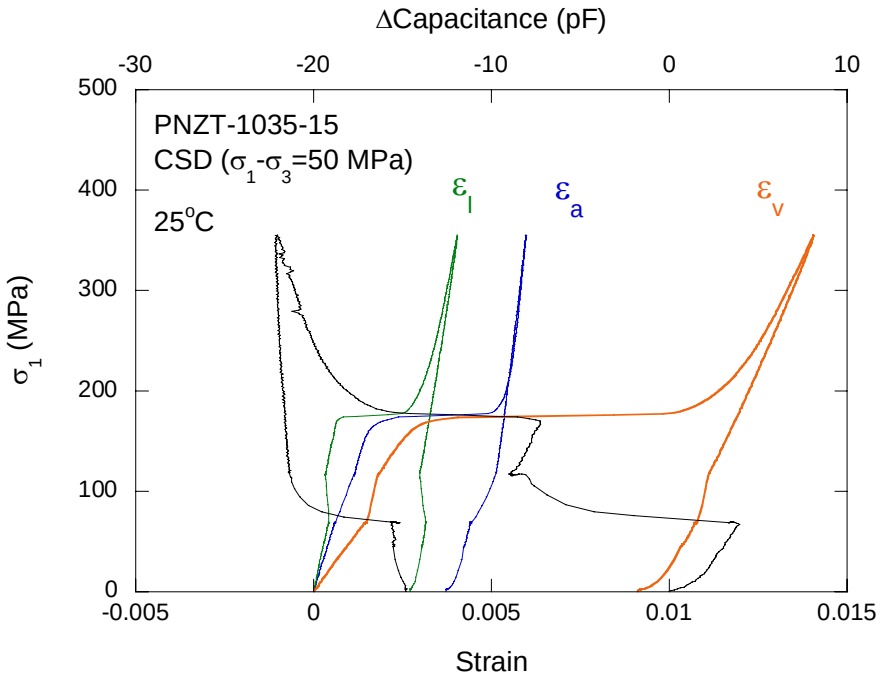

Figure 15. Maximum compressive stress (σ_1)-strain and σ_1-Δcapacitance responses of the unpoled "chem-prep" PNZT-1035-15 under a constant stress difference (CSD) loading condition. Initiation of phase transformation is represented by a sudden increase in axial (ε_a), lateral (ε_l), and volumetric (ε_v) strains and a decrease in capacitance around 168 MPa of σ_1.

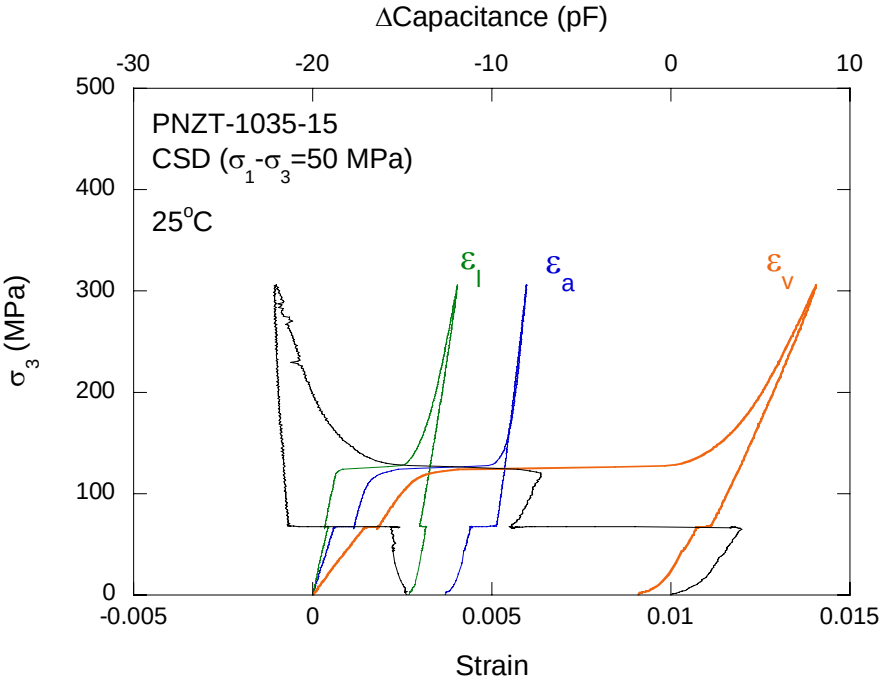

Figure 16. Minimum compressive stress (σ_3)-strain responses of the unpoled "chem-prep" PNZT-1035-15 under a constant stress difference (CSD) loading condition. Initiation of phase transformation is represented by a sudden increase in axial (ε_a), lateral (ε_l), and volumetric (ε_v) strains and a decrease in capacitance around 118 MPa of σ_3.

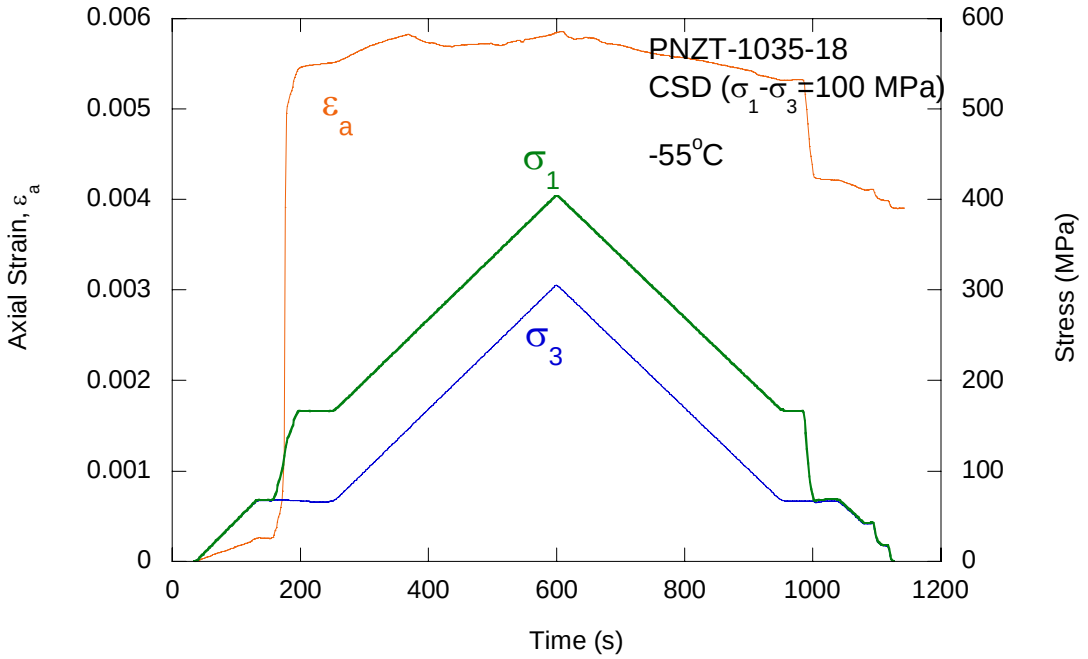

Figure 17. Strain histories of the unpoled "chem-prep" PNZT-1035-18 specimen under a constant stress difference (CSD) test condition. The initiation of phase transformation is represented by a sudden increase in the axial strain (ε_a) before the preset stress difference (σ_d=100 MPa) is reached.

Table 4. Summary of phase transformation in unpoled "chem-prep" PNZT-HF1035 under Constant Stress Difference (CSD) loading.

Specimen no.	Polarization	Temperature (°C)	σ_d (MPa)	σ_{U3}^{CSD} (MPa)	σ_{U1}^{CSD} (MPa)	σ_{Um}^{CSD} (MPa)
PNZT-1035-08	Unpoled	-55	0	96	96	96
PNZT-1035-17	Unpoled	-55	50	67	117	84
PNZT-1035-18*	Unpoled	-55	100	NA	NA 0	NA
PNZT-1035-01	Unpoled	25	0	151	151	151
PNZT-1035-15	Unpoled	25	50	118	168	135
PNZT-1035-16	Unpoled	25	100	75	175	108
PNZT-1035-12	Unpoled	75	0	228	228	228
PNZT-1035-19	Unpoled	75	50	221	271	238
PNZT-1035-20	Unpoled	75	100	208	308	241

σ_d - stress difference between the maximum (σ_1) and the minimum (σ_3) compressive stresses

σ_{Um}^{CSD} - mean stress ($\sigma_{U1}^{CSD} + 2\sigma_{U3}^{CSD}$) / 3

σ_{U1}^{CSD} -maximum compressive stress for FE to AFE phase transformation under CSD compression

σ_{U3}^{CSD} -minimum compressive stress for FE to AFE phase transformation under CSD compression

*-Incipient phase transformation before initiation of CSD testing

Table 4 shows the effect of temperature on the critical stresses required for the phase transformation of the "chem-prep" PNZT-HF1035 under a CSD condition. Both the maximum principal stress (σ_{U1}^{CSD}) and the mean stress (σ_{Um}^{CSD}) for the FE to AFE phase transformation increased with temperature for the same σ_d level. This trend is consistent with the temperature effect found in HF803 (Lee *et al.*, 2003). If we assume that the phase transformation occurs when the maximum compressive stress reaches the hydrostatic pressure at which transformation would otherwise take place in hydrostatic compression, then the mean stress, σ_{Um}^{CSD}, at transformation can be represented as follows (Zeuch *et al.*, 1999b):

$$\begin{aligned} \sigma_{Um}^{CSD} &= \frac{(\sigma_{U1}^{CSD} + 2\sigma_3)}{3} \\ &= \frac{\sigma_{U1}^{CSD} + 2(\sigma_{U1}^{CSD} - \sigma_d)}{3} \\ &= \sigma_{U1}^{CSD} - \frac{2\sigma_d}{3} \end{aligned} \qquad (4)$$

Equation 4 shows that the mean stress required for transformation will be lowered by two-thirds of σ_d. The test results from the low (-55ºC) and the ambient (25ºC) temperatures generally support the maximum stress criterion for phase transformation in HF1035. Figure 18 shows the effects of increasing σ_d or shear stress on the phase transformation at ambient temperature. Increasing σ_d from 0 to 100 MPa clearly decreases σ_{Um}^{CSD}. However, at the elevated temperature (75ºC), σ_{Um}^{CSD} did not decrease as suggested in Equation 4. At high temperature, a transition from the FE to the AFE phase under a CSD test condition is rather gradual compared to the transition at ambient or lower temperature. It appears that we may have overestimated σ_{U1}^{CSD} (or σ_{U3}^{CSD}) in PNZT-1035-19 and PNZT-1035-20 with σ_d of 50 and 100 MPa, respectively.

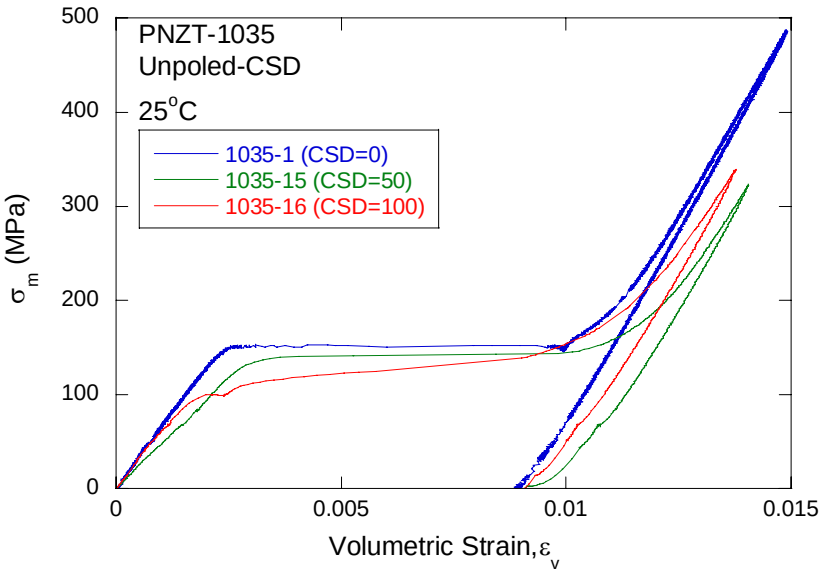

Figure 18. Volumetric strain (ε_v)-mean stress (σ_m) responses of the unpoled "chem-prep" PNZT-HF1035 specimens under a constant stress difference (CSD) loading path.

4. Experimental characterization of poled "chem-prep" HF1035 ceramic

4.1 Hydrostatic compression test

In poled PNZT, the electric field used for polarization causes an adaptation of the ferroelectric domain structure within the material, for which the spontaneous polarization within the domain is aligned more closely to the direction of the electric field. Internal stress and grain boundary clamping within the ceramic prevent perfect alignment of the ferroelectric domains with the applied field. As a consequence, when the electric field is removed, a remanent polarization having a value less than that of the spontaneous polarization in ferroelectric domain remains and binds charge to electrodes on the surface of the ceramic. If the hydrostatic pressure is increased past the critical pressure required for phase transformation to AFE state, this bound charge can be released to generate current and voltage.

Figure 19 shows typical strain versus pressure plots under increasing hydrostatic pressure for the poled "chem-prep" PNZT-1035-31 specimen. All tests on poled PNZT HF1035 were conducted into low impedance circuits and consequently no significant electric fields were generated within the material. The axial strain (ε_a) was measured by a pair of strain gages. The response of each strain gage was similar, so only the average value of the strains is presented in the plot. Also shown are the values of the lateral strain measured parallel ($\varepsilon_{1\text{-parallel to poling}}$) and normal ($\varepsilon_{1\text{-normal to poling}}$) to the poling direction. The configuration of strain measurements with respect to loading and poling directions are shown in Figure 2c.

Similar to the unpoled PNZT HF1035 ceramic, the poled ceramic indicates a transition from a FE rhombohedral pervoskite structure to an AFE orthorhombic structure by a sudden increase in strain. The sudden increase in strain is shown as horizontal lines in Figure 19. The phase transformation pressures corresponding to the horizontal lines were all identical for different strain indicators. All three horizontal lines are shown essentially as a single line during transformation. The poled PNZT ceramic does, however, show a deviation from the typical response of the unpoled ceramic in that it demonstrates anisotropic strain behavior in the AFE phase. In the case of the poled PNZT HF1035, $\varepsilon_{l\text{-parallel to poling}}$ was greater than $\varepsilon_{l\text{-normal to poling}}$ by approximately 35% (Figure 19). This distinctive and repeatable anisotropic strain behavior is caused by a preferred crystallographic orientation and locked-in, intra- and inter-granular strains created by poling (Zeuch *et al.*, 1999a). The degree of anisotropy of the HF1035 ceramic in lateral strains was approximately same as the one obtained for different batches of PNZT during previous experiments (Zeuch *et al.*, 1995 for HF424 and Lee *et al.*, 2004 for HF803).

Figure 20 shows the strain histories under increasing hydrostatic pressures for the same specimen PNZT-1035-31 shown in Figure 19. The FE to AFE phase transformation is marked by the vertical lines at the depoling pressure, P_p^H. In this time-base plot, the anisotropic strain response of the poled PNZT HF1035 in AFE phase is represented as $\varepsilon_{l\text{-}}$

$_{\text{parallel to poling}}$ showing about 35% higher than $\varepsilon_{\text{l-normal to poling}}$. In the FE phase, differences among ε_a, $\varepsilon_{\text{l-parallel to poling}}$, and $\varepsilon_{\text{l-normal to poling}}$ are insignificant suggesting isotropic strain behavior.

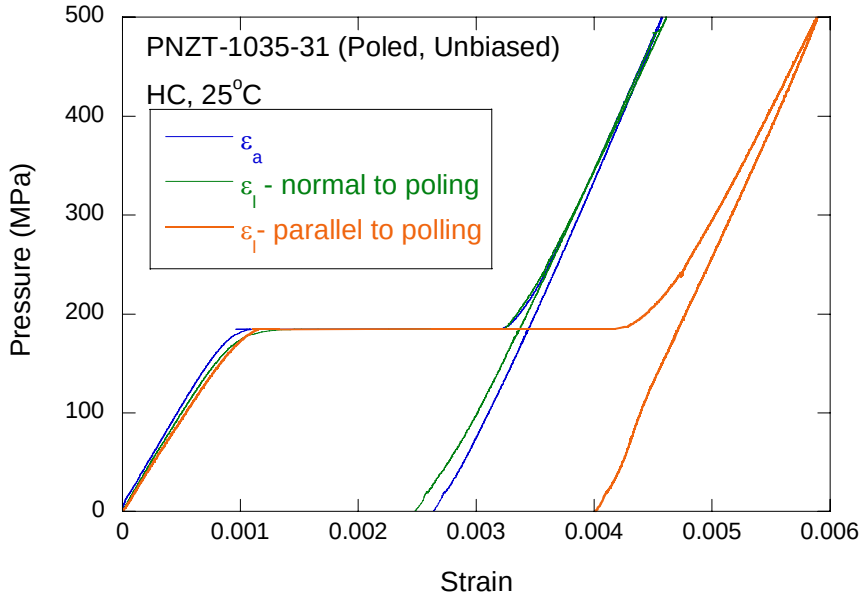

Figure 19. Anisotropic strain behavior in antiferroelectric phase of the poled "chem-prep" PNZT-1035-31 specimen under a hydrostatic loading condition (ε_a – axial strain; $\varepsilon_{\text{l-parallel to poling}}$ – lateral strain parallel to poling direction, and $\varepsilon_{\text{l-normal to poling}}$ – lateral strain perpendicular to poling direction).

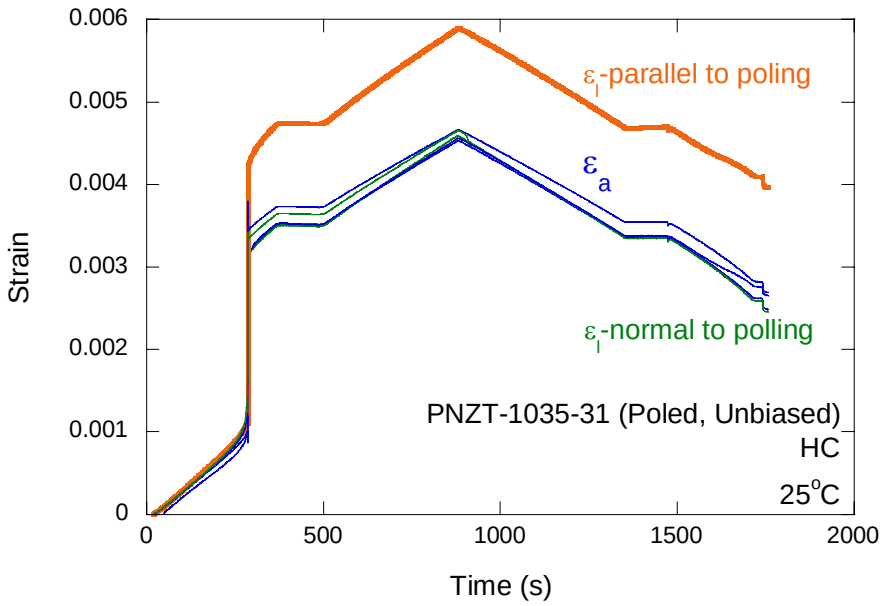

Figure 20. Strain histories of the poled "chem-prep" PNZT-1035-31 specimen under a hydrostatic loading condition. The initiation of phase transformation is represented by a sudden increase in strains (ε_a – axial strain; $\varepsilon_{\text{l-parallel to poling}}$ – lateral strain parallel to poling direction, and $\varepsilon_{\text{l-normal to poling}}$ – lateral strain perpendicular to poling direction).

In poled PNZT ceramics, the charge release, measured across the poling direction at depoling pressure, can be used to confirm the FE to AFE phase transformation. As the hydrostatic pressure is reaching the critical pressure, the volumetric strain ($\varepsilon_v = \varepsilon_a + \varepsilon_{l\text{-parallel to poling}} + \varepsilon_{l\text{-normal to poling}}$) suddenly increases at the phase transformation pressure, P_P^H. At the same time the poled ceramic discharges the bound charge showing as another straight line in the discharge versus pressure plot. Figure 21 confirms that sudden increases in ε_v and in discharge voltage were observed at the exact same P_p^H.

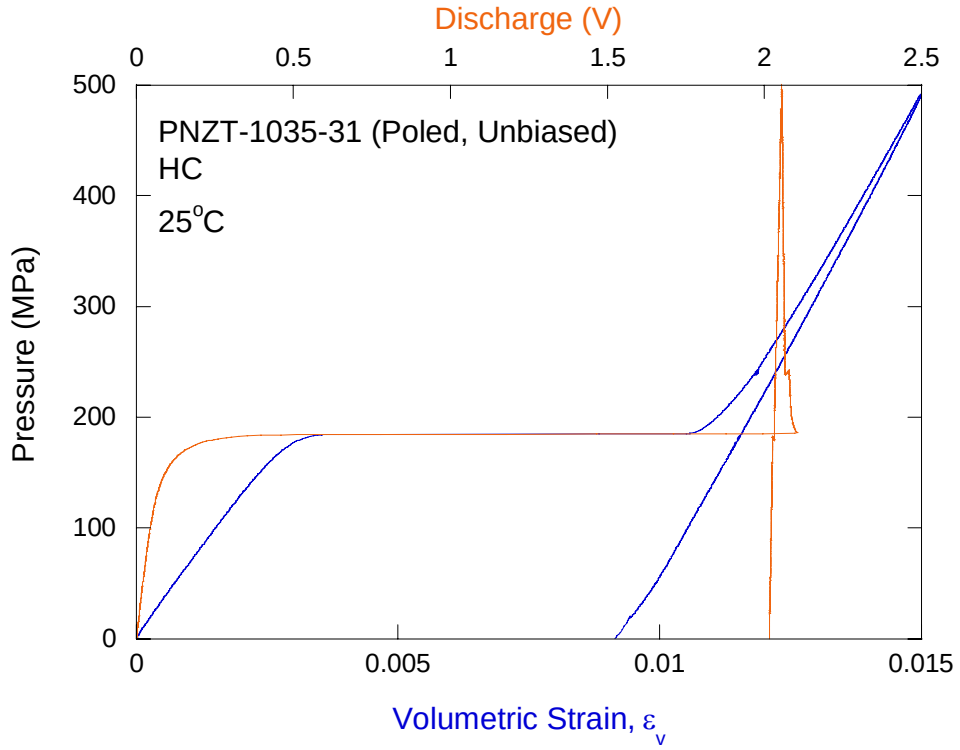

Figure 21. Volumetric strain (ε_v) versus pressure and discharge voltage versus pressure plots for the poled "chem-prep" PNZT-1035-31 specimen under a hydrostatic loading condition. The initiation of phase transformation is represented by a sudden increase in volumetric strain and discharge voltage.

As shown in Figures 22 and 23, the depoling pressure, P_P^H, increases as the temperature increases. Variations of P_P^H with respect to temperature are well represented by a second-order polynomial function of temperature. The best-fit curve is:

$$P_P^H \text{ (MPa)} = 174 + 0.56\ T\ (^oC) + 0.0049\ T^2(^oC) \qquad (5)$$

where the depoling pressures P_P^H is in MPa and T is temperature in degree C.

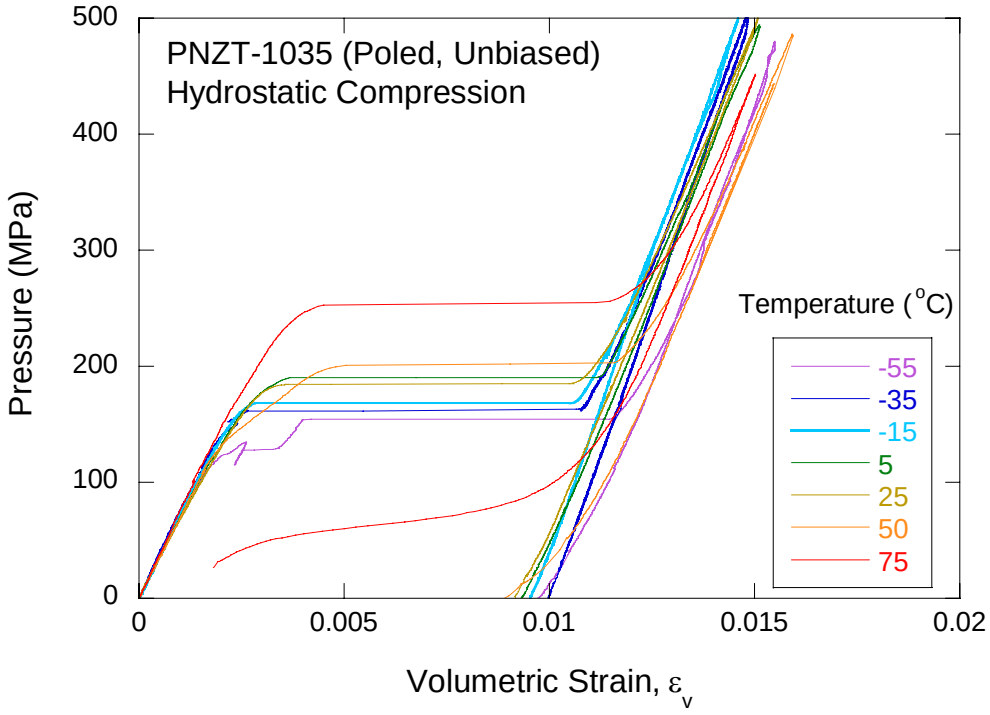

Figure 22. Superimposed volumetric strain (ε_v) versus pressure plots for the hydrostatic compression tests on poled "chem-prep" PNZT-HF1035 specimens at temperatures ranging from –55 to 75°C.

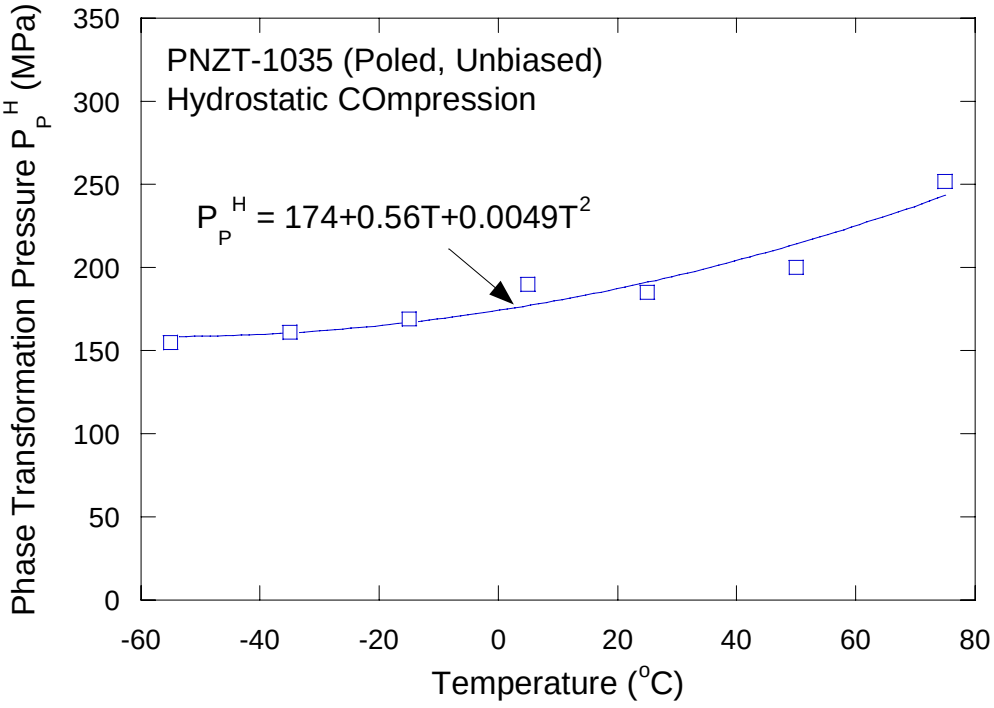

Figure 23. Variation of phase transformation pressure, P_P^H, for poled "chem-prep" PNZT-HF1035 ceramic with temperature, T.

Variations of bulk moduli K_F and K_A in poled HF1035 ceramic are shown in Figures 24 and 25. As in the unpoled HF1035, it appears that bulk moduli are not dependent on temperature and can be represented as the following mean values.

$$K_F \text{ (GPa)} = 70.9 \pm 3.1 \text{ (GPa)}$$
$$K_A \text{ (GPa)} = 94.0 \pm 6.0 \text{ (GPa)} \qquad (6)$$

It is also noted that K_A was significantly larger than K_F. The values of bulk moduli in poled HF1035 are about 3 to 4% higher than those in the unpoled HF1035. A detailed quantitative description of phase transformation in the poled PNZT-HF1035 ceramic under hydrostatic loading is summarized in Table 5.

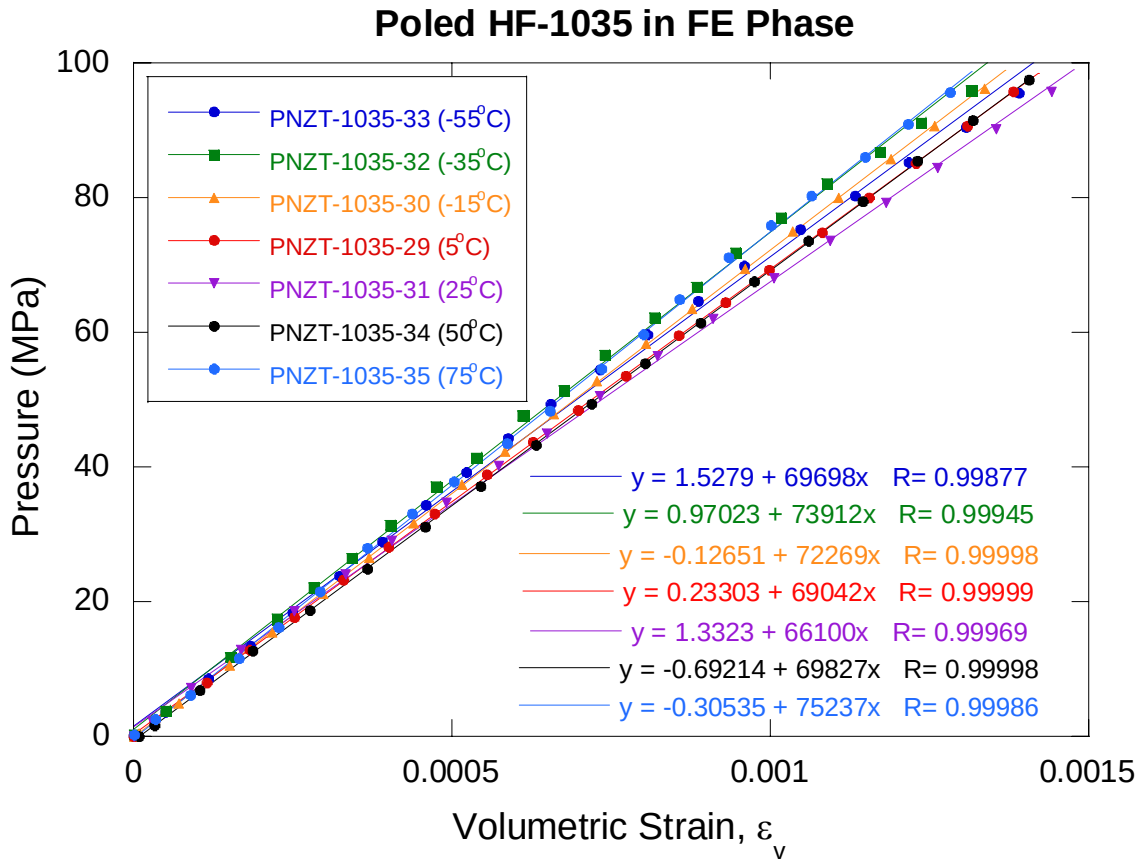

Figure 24. Bulk modulus of poled "chem-prep" PNZT-HF1035 ceramic in the FE phase obtained from linear fits to the pressure versus measured volumetric strain (ε_v) prior to the onset of the transformation to the AFE phase.

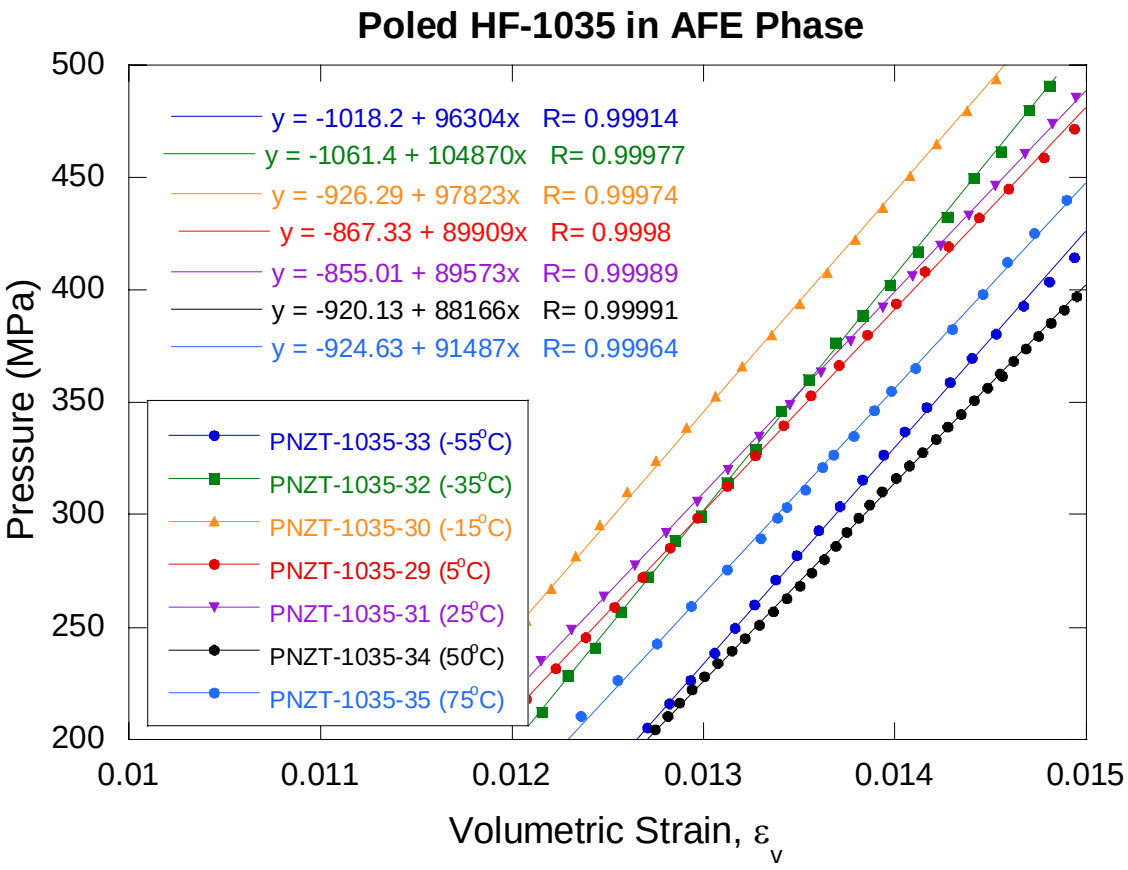

Figure 25. Bulk modulus of poled "chem-prep" PNZT-HF1035 ceramic in the AFE phase obtained from linear fits to the pressure versus measured of volumetric strain (ε_v) curve in antiferroelectric phase after the transformation to the AFE phase.

Table 5. Summary of phase transformation in poled "chem-prep" PNZT-HF1035 under hydrostatic compression (HC).

Specimen no.	Polarization	Temperature (°C)	K_F (GPa)	K_A (GPa)	ε_v^H	P_P^H (MPa)
PNZT-1035-33	Poled	-55	70	96	NA	155
PNZT-1035-32	Poled	-35	74	105	0.0027	161
PNZT-1035-30	Poled	-15	72	98	0.0028	169
PNZT-1035-29	Poled	5	69	90	0.0036	190
PNZT-1035-31	Poled	25	66	90	0.0034	185
PNZT-1035-34	Poled	50	70	88	NA	200
PNZT-1035-35	Poled	75	75	91	0.0045	252

K_F - bulk modulus in FE (ferroelectric) phase

K_A - bulk modulus in AFE (antiferroelectric) phase

P_u^H - pressure for FE to AFE phase transformation under hydrostatic compression

ε_{vu}^H - volumetric strain at P_u^H

The location of the phase boundaries for "chem-prep" PNZT-HF1035 in temperature-pressure space has been determined from the hydrostatic compression experiments. Figure 26 shows the results from HF1035 combined with our earlier tests on HF803 (Lee *et al.*, 2003 and 2004). As shown in previous Equations 1 and 5, the relationships between temperature and phase transformation pressure appear to be non-linear in the case of the poled and unpoled ceramics of "chem-prep" PNZT-HF1035 (Figure 26). However, the FE-AFE phase relationships for the PNZT-HF803 that falls at the high end of the depoling pressure range was found to be linear (Lee *et al.*, 2003 and 2004):

$$P_u^H \text{ (MPa)} = 227 + 0.76\ T\ (^oC) \quad \text{for unpoled HF803} \qquad (7)$$

$$P_p^H \text{ (MPa)} = 261 + 0.74\ T\ (^oC) \quad \text{for poled HF803} \qquad (8)$$

where P_u^H and P_p^H are the unpoled and poled phase transformation pressures in MPa, respectively, and T is temperature in °C.

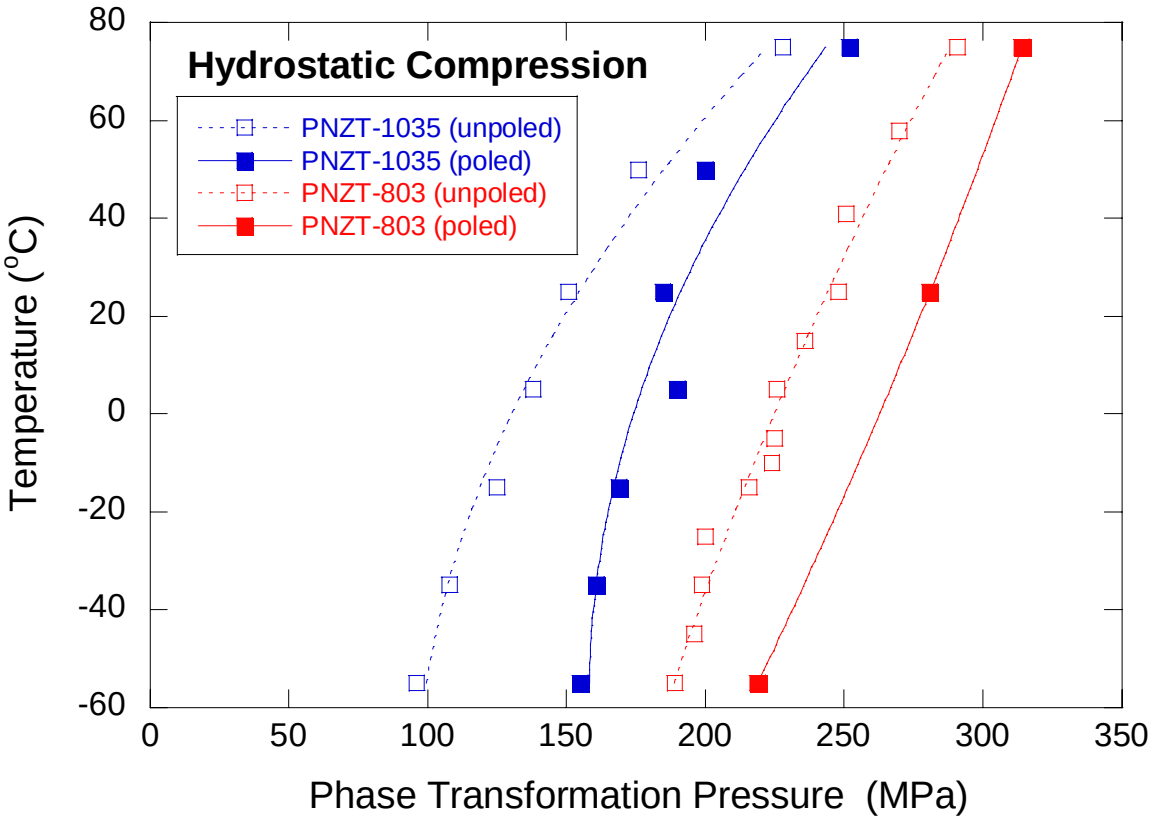

Figure 26. Phase boundaries of "chem-prep" PNZT-HF1035 and HF803 ceramics in temperature-pressure space.

4.2 Unconfined uniaxial compression test

Three uniaxial compression (UC) tests were carried out on poled "chem-prep" PNZT-HF1035 ceramic at temperatures of -55, 25, and 75°C. Figures 27 and 28 are typical stress versus stain plots from the uniaxial compression test of the poled PNZT-1035-38 specimen. The uniaxial compressive stress (σ_a) was applied along the long axis of the specimen. The stress was plotted against ε_a, $\varepsilon_{\text{l-parallel to poling}}$, and $\varepsilon_{\text{l-normal to poling}}$, respectively. The discharge voltage and the normalized P-wave velocity were also plotted against σ_a. These two plots were compared with the stress-strain plot to identify the phase transformation pressure in the UC tests. All three test records from UC testing of the poled "chem-prep" PNZT-HF1035 ceramic are shown in Appendix B-2.

Unlike the distinctive phase transformation shown in the HC tests, strains and discharge voltage in the poled HF1035 ceramic were increasing gradually as the axial stress (σ_a) was increased during the UC tests. Axial strain (ε_a) increased linearly with the axial stress until the phase transformation occurred as indicated by the gradual increase in discharge voltage. The lateral strain changes slope as a result of superposition of both dilatational lateral strains caused by the shear stress at low mean stress and the strains produced during the FE to AFE phase transformation (Lee *et al.*, 2004). Table 6 summarizes the uniaxial compression tests for poled "chem-prep" PNZT-HF1035 ceramic. The maximum stress, $\sigma_{P1}{}^{U}$, required for phase transformation under the UC condition is within 17% of the FE to AFE phase transformation pressure, $P_P{}^{H}$, measured under hydrostatic compression. Due to gradual changes in strain without a distinct inflection point, the selected maximum stress and the calculated mean stress values for FE to AFE phase transformation under uniaxial compression may contain significant uncertainties. As in the unpoled PNZT-HF1035 ceramic, the phase transformation in poled PNZT ceramic occurs when $\sigma_{P1}{}^{U}$ is approximately equal to $P_P{}^{H}$ required under the hydrostatic loading condition.

$$\sigma_{P1}{}^{U} (\equiv 3\sigma_{Pm}{}^{U}) \approx P_U{}^{H} \qquad (9)$$

Therefore, the overall maximum principal stress rather than the mean stress ($\sigma_1=\sigma_a=3\sigma_m$) appears to be the controlling stress for phase transformation in PNZT.

Table 6. Summary of phase transformation in poled "chem-prep" PNZT-HF1035 under uniaxial compression (UC).

Specimen no.	Polarization	Temperature (ºC)	$\sigma_{p1}{}^{U}$ (MPa)	$\sigma_{pm}{}^{U}$ (MPa)	$P_p{}^{H}$ (MPa)
PNZT-1035-38	Poled	-55	130	43	155
PNZT-0035-37	Poled	25	190	63	185
PNZT-1035-39	Poled	75	280	93	252

$\sigma_{P1}{}^{U}$ - maximum stress required for FE to AFE phase transformation of poled ceramic under uniaxial compression

$\sigma_{Pm}{}^{U}$ - mean stress required for FE to AFE phase transformation of poled ceramic under uniaxial compression

$P_P{}^{H}$ - FE to AFE phase transformation pressure of poled ceramic under hydrostatic compression

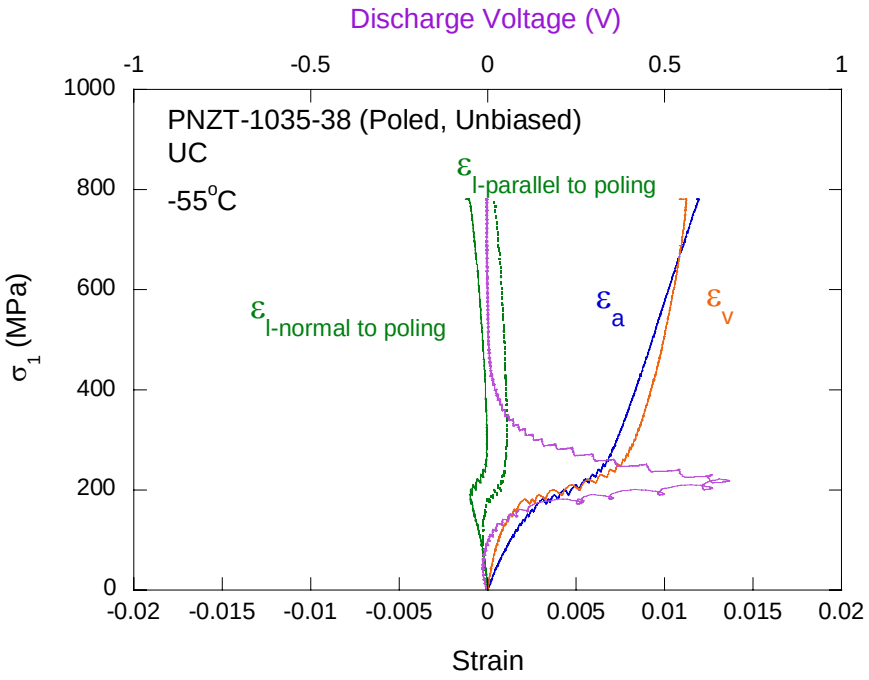

Figure 27. Typical uniaxial compression test conducted on a poled "chem-prep" PNZT-HF1035 ceramic. The maximum principal stress (σ_1) is plotted against the axial (ε_a), lateral (ε_l), and volumetric (ε_v) strains. The axial stress is also plotted against the discharge voltage.

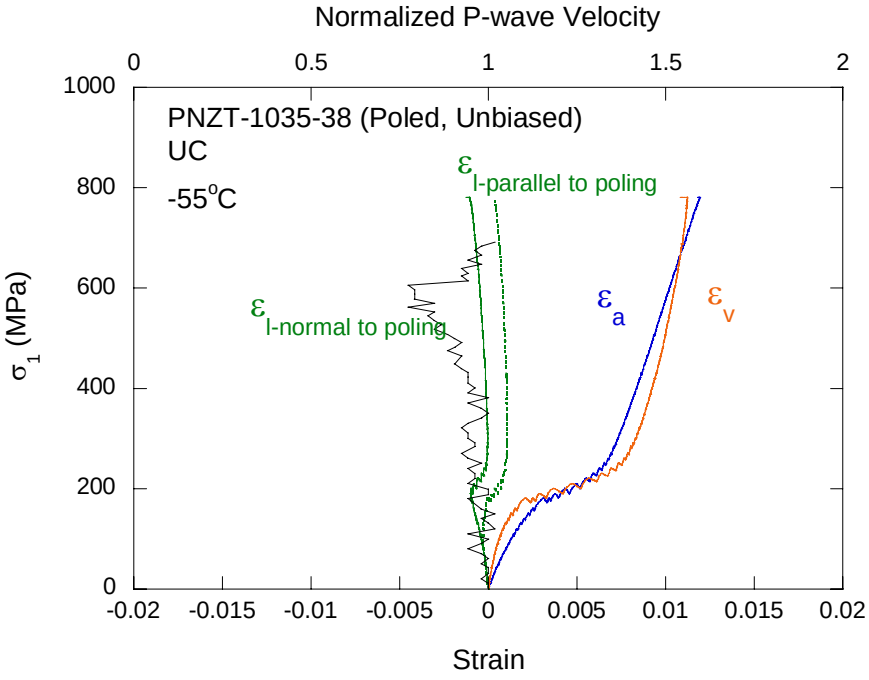

Figure 28. Typical uniaxial compression test conducted on a poled "chem-prep" PNZT-HF1035 ceramic. The maximum principal stress (σ_1) is plotted against the axial (ε_a), lateral (ε_l), and volumetric (ε_v) strains. The axial stress is also plotted against the normalized P-wave velocity.

4.3 Constant stress difference test

The effects of shear stress and temperature on poled "chem-prep" PNZT-HF1035 ceramic were investigated at two stress differences (σ_d=50 and 100 MPa) and three temperatures (-55, 25, and 75°C). The results from the poled HC tests were combined with the results from CSD tests to give baseline data for zero stress difference (σ_d=0). The specimens were prepared according to the same procedure and specifications used for the unpoled ceramic. An example of the CSD loading path is shown in Figure 29. The PNZT-1035-45 specimen was loaded hydrostatically to 69 MPa. This pressure is below the expected depoling pressure (P_p^H ~155 MPa at -55°C) determined from the HC tests on the poled HF1035 ceramic. With the confining pressure ($P=\sigma_2=\sigma_3$) held constant, additional load was applied along the long axis of the specimen to create the stress difference (e.g., $\sigma_d=\sigma_1-\sigma_3$=50 MPa). Then, both the maximum principal stress (σ_1) applied in the long axis of the specimen and the confining pressure ($\sigma_2=\sigma_3$) were increased simultaneously at the same rate of 0.69 MPa/s to maintain the stress difference constant while increasing the mean stress (σ_m). Appendix C-2 shows the loading paths used for all poled CSD testing and the stress-strain records with respect to σ_1 and σ_3, respectively.

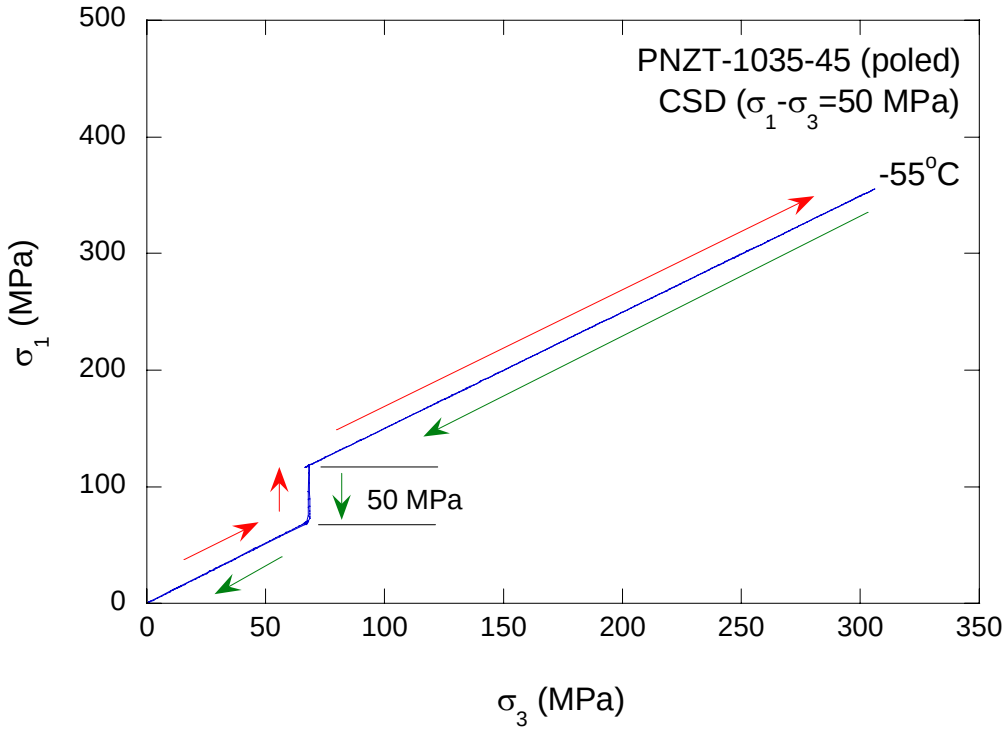

Figure 29. A loading path from the Constant Stress Difference test in poled "chem-prep" PNZT HF1035-46 specimen with a 50 MPa stress difference.

The primary difference between the poled and the unpoled CSD tests was anisotropic strain behavior of the lateral strains with respect to the poling direction. Therefore, additional lateral strain gages were used to measure $\varepsilon_{\text{l-parallel to poling}}$ and $\varepsilon_{\text{l-normal to poling}}$, independently. Figures 30 and 31 show changes of ε_a, $\varepsilon_{\text{l-parallel to poling}}$, and $\varepsilon_{\text{l-normal to poling}}$ with respect to σ_1 and σ_3 under CSD loading. As in the HC and unpoled CSD tests, a sudden increase in volumetric strain ($\varepsilon_v = \varepsilon_a + \varepsilon_{\text{l-parallel to poling}} + \varepsilon_{\text{l-normal to poling}}$) of the specimen indicates the FE to AFE transition. Figures 30 and 31 also show that the pressure level for phase transformation is in good agreement with the depoling pressure identified from the strain-discharge voltage plot.

Table 7 summarizes the results from the CSD tests conducted on the poled "chem-prep" PNZT-HF1035 ceramic. Results from the HC tests (PNZT-1035-33, 31, and 35) are also included to show the baseline case (σ_d=0 MPa) for CSD loading. At each temperature, a consistent increase of σ_d (or shear stress) was observed for increasing σ_{P1}^{CSD}, the maximum principal stress required for FE to AFE phase transformation under CSD stress condition. Table 7 also shows the effect of temperature on the critical stresses required for the phase transformation. If the tests conducted for the same stress difference (e.g., σ_d=50 MPa) are chosen, both σ_{P3}^{CSD} and σ_{P1}^{CSD} increase with the temperature. As suggested from Equation 4 and the result from the unpoled HF1035, the mean stress, σ_{Pm}^{CSD}, for transformation of the poled ceramic, will be lowered by two-thirds of σ_d. As in the unpoled HF1035, the test results from the low (-55ºC) and the ambient (25ºC) temperatures generally support the maximum stress criterion for phase transformation. However, at the elevated temperature (75ºC) σ_{Pm}^{CSD} did not decrease monotonically as σ_d increased.

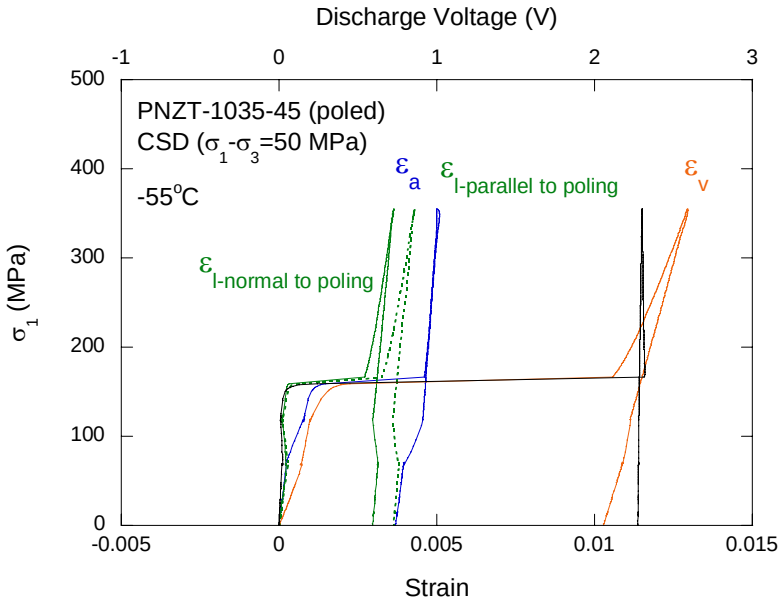

Figure 30. Maximum compressive stress (σ_1)-strain responses of the poled "chem-prep" PNZT-HF1035 under constant stress difference (CSD) loading. Initiation of phase transformation is represented by a sudden increase in axial (ε_a), lateral (ε_l), and volumetric (ε_v) strains around 165 MPa of σ_1. Increase in discharge voltage confirms phase transformation.

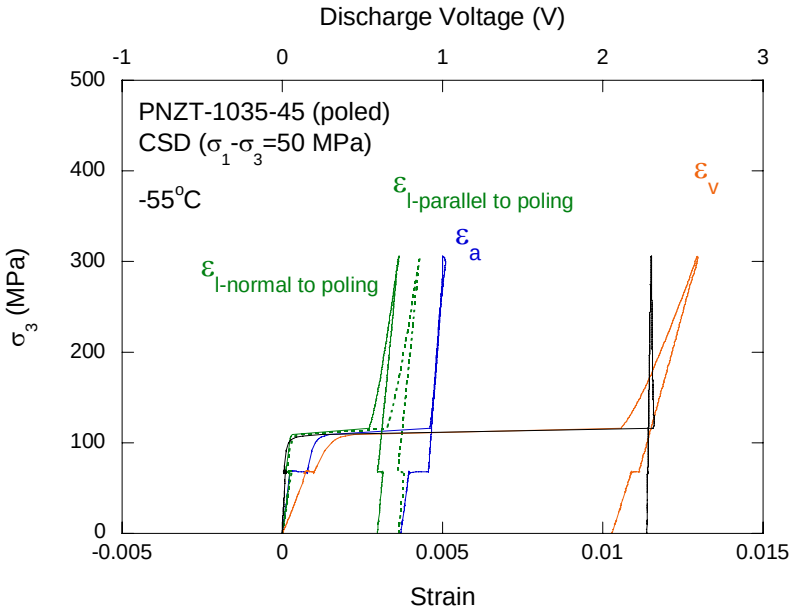

Figure 31. Minimum compressive stress (σ_3)-strain responses of the poled "chem-prep" PNZT-HF1035 under constant stress difference (CSD) loading. Initiation of phase transformation is represented by a sudden increase in axial (ε_a), lateral (ε_l), and volumetric (ε_v) strains around 115 MPa of σ_3. Increase in discharge voltage confirms phase transformation.

Table 7. Summary of phase transformation in poled "chem-prep" PNZT-HF1035 under Constant Stress Difference (CSD) loading.

Specimen no.	Polarization	Temperature (^{o}C)	σ_d (MPa)	σ_{P3}^{CSD} (MPa)	σ_{P1}^{CSD} (MPa)	σ_{Pm}^{CSD} (MPa)
PNZT-1035-33	Poled	-55	0	155	155	155
PNZT-1035-45	Poled	-55	50	115	165	132
PNZT-1035-46*	Poled	-55	100	67	167	100
PNZT-1035-31	Poled	25	0	185	185	185
PNZT-1035-44	Poled	25	50	154	204	171
PNZT-1035-43	Poled	25	100	NA	NA	NA
PNZT-1035-35	Poled	75	0	252	252	252
PNZT-1035-47	Poled	75	50	275	325	292
PNZT-1035-48	Poled	75	100	219	319	252

σ_d - stress difference between the maximum (σ_1) and the minimum (σ_3) compressive stresses

σ_{Pm}^{CSD} - mean stress, $(\sigma_{P1}^{CSD} + 2\sigma_{P3}^{CSD}) / 3$

σ_{P1}^{CSD} -maximum compressive stress for FE to AFE phase transformation under CSD compression

σ_{P3}^{CSD} -minimum compressive stress for FE to AFE phase transformation under CSD compression

*-Phase transformation occurred before the initiation of CSD testing

Due to a preferential crystallographic orientation caused by preferential domain alignment in poled ceramics, not only the magnitude of σ_{P1}^{CSD} but also its directional relationship to the crystallographic plane about the polar axis becomes important. Figure 32 shows a schematic of a poled ceramic specimen under a triaxial stress condition ($\sigma_1 > \sigma_2 = \sigma_3$).

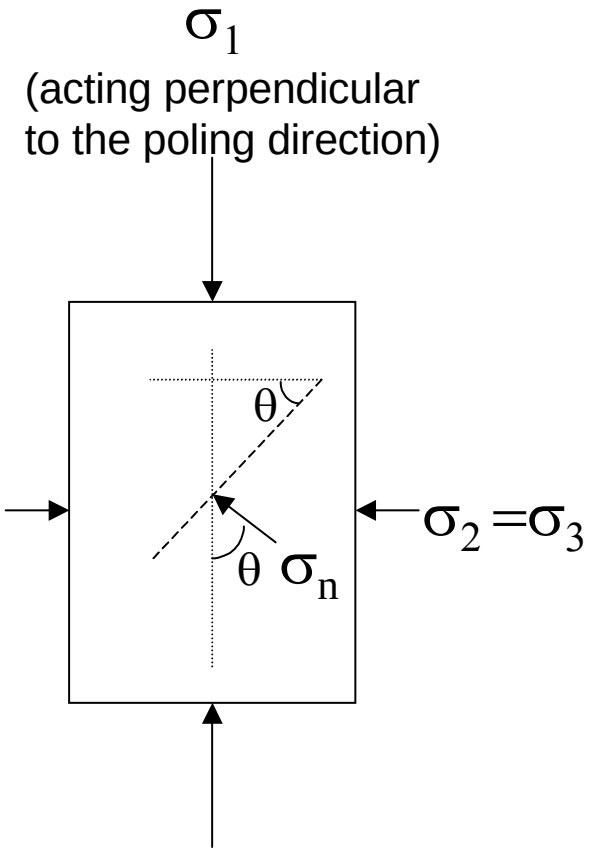

Figure 32. Schematic of a poled ceramic under a triaxial stress condition. σ_1, σ_2, and σ_3 are the maximum, intermediate, and minimum principal stresses, respectively. σ_n is the stress acting normal to the crystallographic plane dipping θ from the poling direction.

We assume that the transformation occurs when the normal compressive stress (σ_n) reaches the hydrostatic pressure (P_P^H) at which the FE to AFE transformation would otherwise take place.

$$\sigma_n = \frac{\sigma_1 + \sigma_3}{2} + \frac{\sigma_1 - \sigma_3}{2}\cos 2\theta \qquad (10)$$

$$\sigma_n = P_P{}^H \qquad (11)$$

Then, the maximum principal stress (σ_{P1}^{CSD}) at the FE to AFE transformation can be represented in terms of the stress difference (σ_d).

$$P_P{}^H = \frac{\sigma_{P1}^{CSD} + \sigma_{P3}^{CSD}}{2} + \frac{\sigma_{P1}^{CSD} - \sigma_{P3}^{CSD}}{2}\cos 2\theta \tag{12}$$

$$P_P{}^H = \frac{\sigma_{P1}^{CSD} + (\sigma_{P1}^{CSD} - \sigma_d)}{2} + \frac{\sigma_d}{2}\cos 2\theta \tag{13}$$

$$\sigma_{P1}^{CSD} = P_P^H + \frac{1-\cos 2\theta}{2}\sigma_d \tag{14}$$

Equation (14) is a general formula of phase transformation both for the unpoled and for the poled ceramic. For an unpoled ceramic, no preferential crystallographic plane exists about the polar axis. Therefore, some crystallographic plane exists oriented perpendicular to σ_1 (or $\theta = 0$). Thus, the following FE to AFE criterion for the unpoled ceramic is derived from the general criterion shown in equation (14).

$$\sigma_{U1}^{CSD} = P_u^H \tag{15}$$

Equation (15) confirms the earlier experimental results (Zeuch *et al.*, 1999a): phase transformation from FE to AFE occurs in unpoled ceramic when the maximum compressive stress equals the hydrostatic pressure at which the transformation otherwise takes place. For a poled ceramic, however, a preferential crystallographic plane ($\theta \neq 0$) exists about the polar axis. Thus, the general criterion as shown in equation (14) becomes the phase transformation criterion for the poled ceramic.

5. Conclusions

Specimens of unpoled and poled PNZT ceramics, taken from batch HF1035 were tested under three different quasi-static loading conditions: hydrostatic compression, uniaxial compression, and constant stress difference loading. The mechanical and electrical response during phase transformation from a ferroelectric (FE) rhombohedral perovskite structure to an antiferroelectric (AFE) orthorhombic structure were investigated over a range of temperatures, with the lowest being -55°C and the highest 75°C . The results are summarized as follows:

- The FE to AFE phase transformation in "chem-prep" PNZT-HF1035 is marked by a sudden increase (decrease in volume) of 0.7 to 0.8% of volumetric strain.

- The curved shape of the phase boundary compares well with the previous findings in "mixed-oxide" ceramic in the phase diagram (Fritz and Keck, 1978).

- The variations of pressures (P_u^H and P_P^H) required for FE to AFE phase transformation depend on temperature.

  P_U^H (MPa) = 130 + 0.84 T (ºC) + 0.0051 T^2 (ºC) for unpoled
  P_P^H (MPa) = 174 + 0.56 T (ºC) + 0.0049 T^2 (ºC) for poled

- We have not observed significant dependency of bulk moduli K_F in FE state and K_A in AFE state with temperature in HF1035 ceramics. The bulk moduli can be represented as follows.

  K_F (GPa) = 68.7±2.3 (GPa) for unpoled and in FE state
  K_A (GPa) = 90.0±2.2 (GPa) for unpoled and in AFE state
  K_F (GPa) = 70.9±3.1 (GPa) for poled and in FE state
  K_A (GPa) = 94.0±6.0 (GPa) for poled and in AFE state

- The FE to AFE phase transformation occurs in the poled "chem-prep" PNZT ceramic when the normal compressive stress (σ_n) acting perpendicular to a crystallographic plane dipping θ from the poling direction, equals the hydrostatic pressure (P_p^H) at which the transformation otherwise takes place. This criterion can be represented in terms of the maximum principal stress (σ_{1P}^{CSD}) at transformation and the stress difference (σ_d):

$$\sigma_{1P}^{CSD} = P_p^H + \frac{1-\cos 2\theta}{2}\sigma_d$$

- The poled "chem-prep" PNZT HF1035 ceramic undergoes anisotropic deformation in the AFE structure. The lateral strain parallel to the poling

direction ($\varepsilon_{l\text{-parallel to poling}}$) is typically 35% greater than the strain perpendicular to the poling direction ($\varepsilon_{l\text{-normal to poling}}$) for the poled PNZT-HF1035 ceramic.

- At the low temperature boundary of -55°C, the FE to AFE phase transformation is permanent and irreversible. However, at higher temperatures (75°C), the phase transformation is completely reversible from AFE to FE as the stress causing the phase transformation is removed.

- The effect of temperature on spreading the range of mean stress required for completing the phase transformation appears to be analogous to the effect of shear stress.

- The uniaxial compression test shows that the controlling stress for phase transformation is the maximum compressive stress.

- Under constant temperature conditions, increasing shear stress lowers the mean stress and the volumetric strain required to trigger phase transformation.

References

Bauer, F., K. Vollrath, Y. Fetiveau and L. Eyraud (1976), *Ferroelectric ceramics: application to mechanical energy conversion under shock compression*, Ferroelectrics, **10**: 61-64.

Brannon, R. M., Montgomery, S. T., Aidun, J. B., and A. C. Robinson (2001), *Macro- and meso-scale modeling of PZT ferroelectric ceramics*, 12th Biennial International Conference of the American Physical Society Topical Group on Shock Compression on Condensed Matter, Atlanta, GA.

Fritz, I. J., and J. D. Keck (1978), *Pressure-temperature phase diagrams for several modified lead zirconate ceramics*, J. Phys. Chem. Solids, **39.** 1163-1167.

Fritz, I. J. (1979), *Stress effects in two modified lead zirconate titanate ferroelectric ceramics*, J. Appl. Phys. **50** (8): 5265-5271.

Jaeger, J.C. and N.G.W., Cook (1969), Fundamentals of Rock Mechanics, 102-106, Methuen, London, England.

Lee, M. Y., Montgomery, S. T., Hofer, J. H. and D. H. Zeuch (2003), *Hydrostatic, uniaxial, and triaxial compression tests on unpoled "Chem-prep" PZT 95/5-2Nb ceramic within temperature range of -55 to 75ºC*, Rept. No. SAND2003-3651, Sandia National Laboratories, Albuquerque, NM.

Lee, M. Y. (2004), *Characterization of "chem-prep" PZT HF1035*, FY04 mid-year review presentation at C-6 conference, Albuquerque, NM.

Lee, M.Y., Montgomery, S.T., and J.H. Hofer (2004), *Phase transformation of poled "chem-prep" PZT 95/5-2Nb ceramic under quasi-static loading conditions*, Rept. No. SAND2004-4954, Sandia National Laboratories, Albuquerque, NM.

Lee, M. Y., Fossum, A., Costin, L. S. and D. Bronowski (2002), Frozen Soil Material Testing and Constitutive Modeling, Rept. No. SAND2002-0524, Sandia National Laboratories, Albuquerque, NM.

Lysne, P. C. and C. M. Percival (1975), *Electric energy generation by shock compression of ferroelectric ceramics: normal-mode response of PZT 95/5*, J. Appl. Phys., **46.** 1519-1526.

Voigt, J.A., Sipola, D. L., Tuttle, B. A. and M. T. Anderson (1999), *Nonaqueous solution synthesis process for preparing oxide powders of lead zirconate titanate and related materials*, U. S. Patent 5,908,802.

Yang, P. (2003, 2004), Personal communication.

Yang, P., Moore, R. H., Lockwood, S. J., Tuttle, B. A., Voigt, J. A., and T. W. Scofield (2003), *Chem-prep PZT 95/5 for neutron generator applications: the effect of pore former type and density on the depoling behavior of chemically prepared PZT 95/5 ceramics*, Rept. No. SAND2003-3866, Sandia National Laboratories, Albuquerque, NM.

Zeuch, D. H., Montgomery, S. T., Carlson, L. W. and D. J. Zimmerer (1995), *The effects of non-hydrostatic compression and applied electric field on the electromechanical behavior of poled PZT 95/5-2Nb ceramic during the $F_{R1} \rightarrow A_O$ polymorphic phase transformation*, Rept. No. SAND95-1951, Sandia National Laboratories, Albuquerque, NM.

Zeuch, D. H., Montgomery, S. T., and D. J. Holcomb (1999a), *The effects of nonhydrostatic compression and applied electric field on the electromechanical behavior of poled lead zirconate titanate 95/5-2Nb ceramic during the ferroelectric to antiferroelectric polymorphic transformation*, J. Mater. Res., **14.** 1814-1827.

Zeuch, D. H., Montgomery, S. T., Carlson, L. W., and J. M. Grazier (1999b), *Failure surfaces and related mechanical properties for poled and unpoled PZT 95/5-2Nb voltage bar ceramic*, Rept. No. SAND99-0635, Sandia National Laboratories, Albuquerque, NM.

Zeuch, D. H., Lee, M. Y., Costin, L. S., Wawersik, W. R., Grazier, J. M., Bronowski, D. R., and R. D. Hardy (1999c), *A high-pressure, low-temperature triaxial test apparatus*, International Mechanical Engineering Congress & Exposition of the ASME. Nashville, TN.

APPENDIX A-1

Hydrostatic Compression Test (HC) Plots for Unpoled PNZT-HF1035

- σ_a-axial stress
- ε_v - volumetric strain
- T-temperature

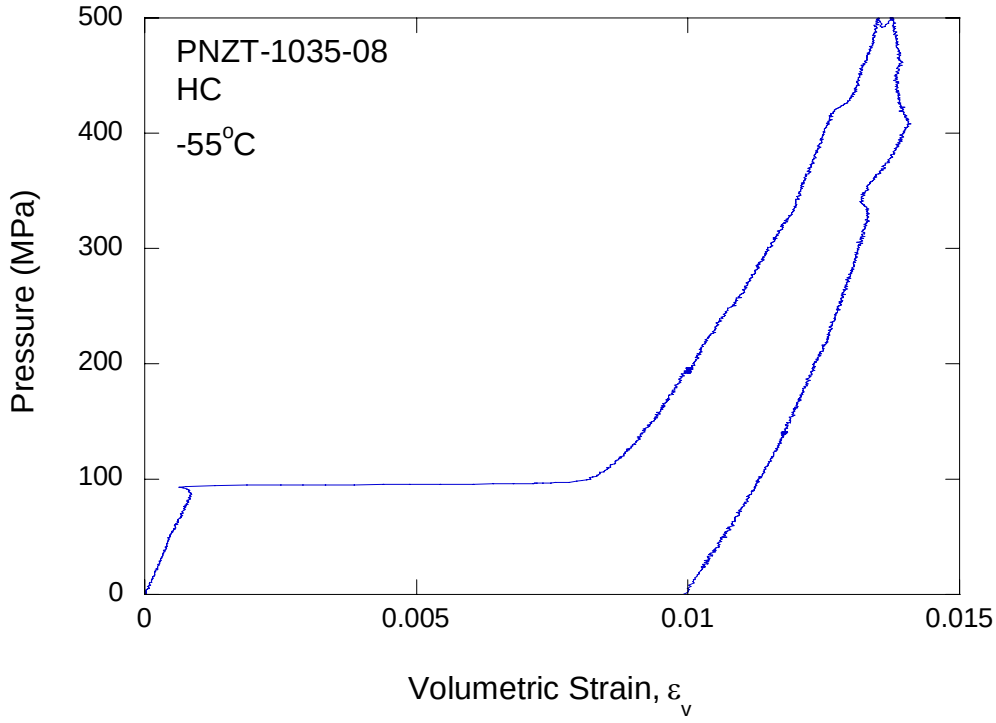
PNZT-1035-08
HC
-55°C
Pressure (MPa)
Volumetric Strain, ε_v
0
100
200
300
400
500
0
0.005
0.01
0.015

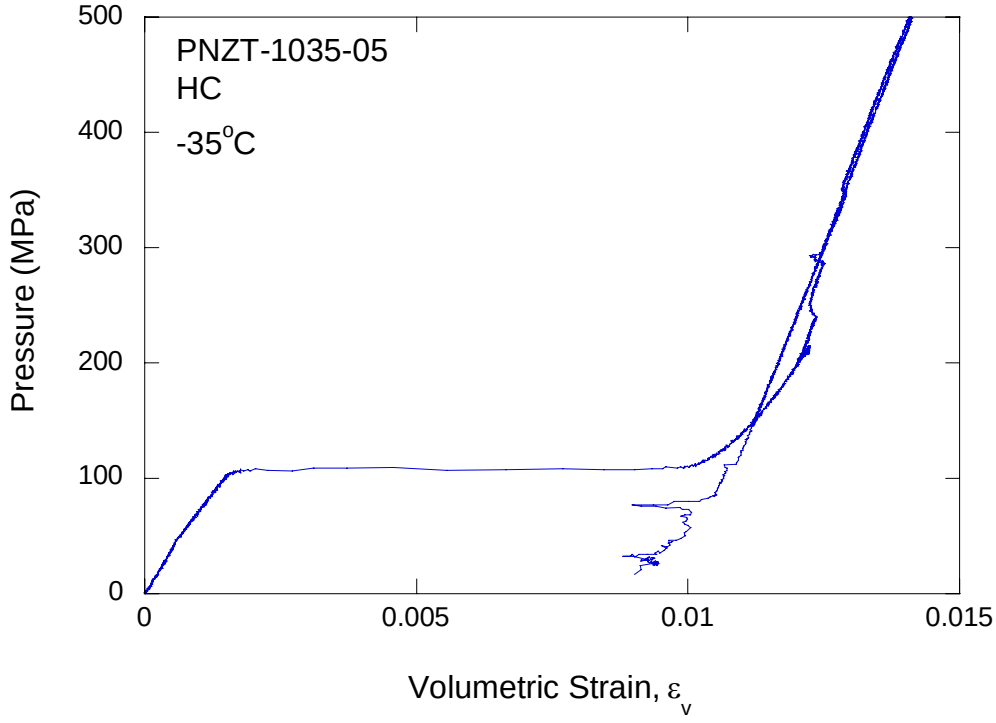
PNZT-1035-05
HC
-35°C
Pressure (MPa)
Volumetric Strain, ε_v
0
100
200
300
400
500
0
0.005
0.01
0.015

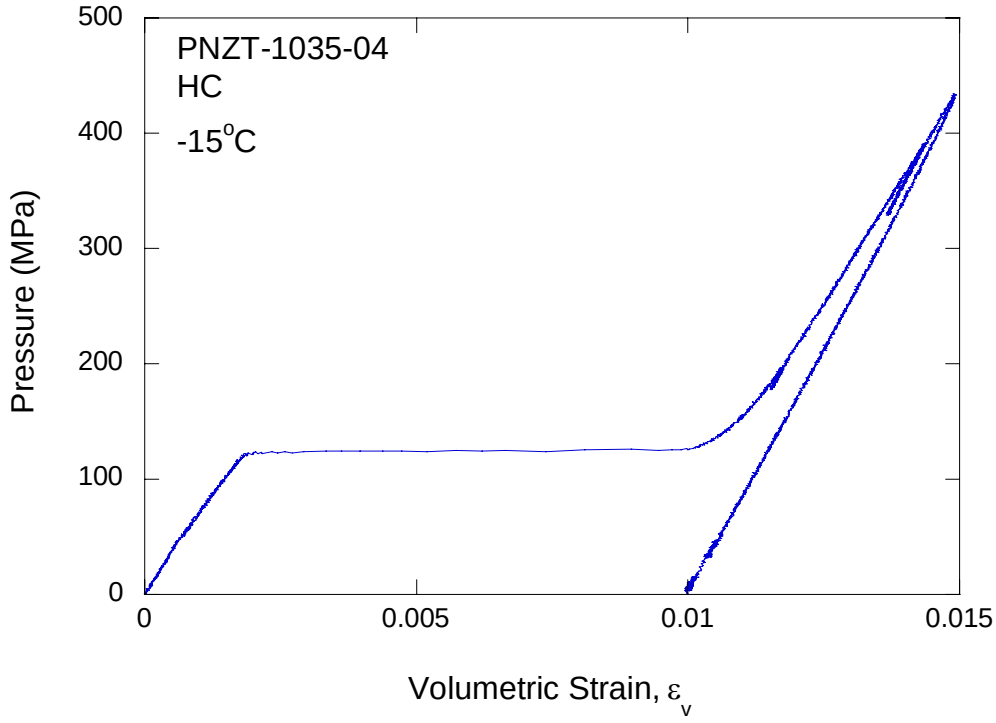
PNZT-1035-04
HC
-15°C
Pressure (MPa)
Volumetric Strain, ε_v
0
100
200
300
400
500
0
0.005
0.01
0.015

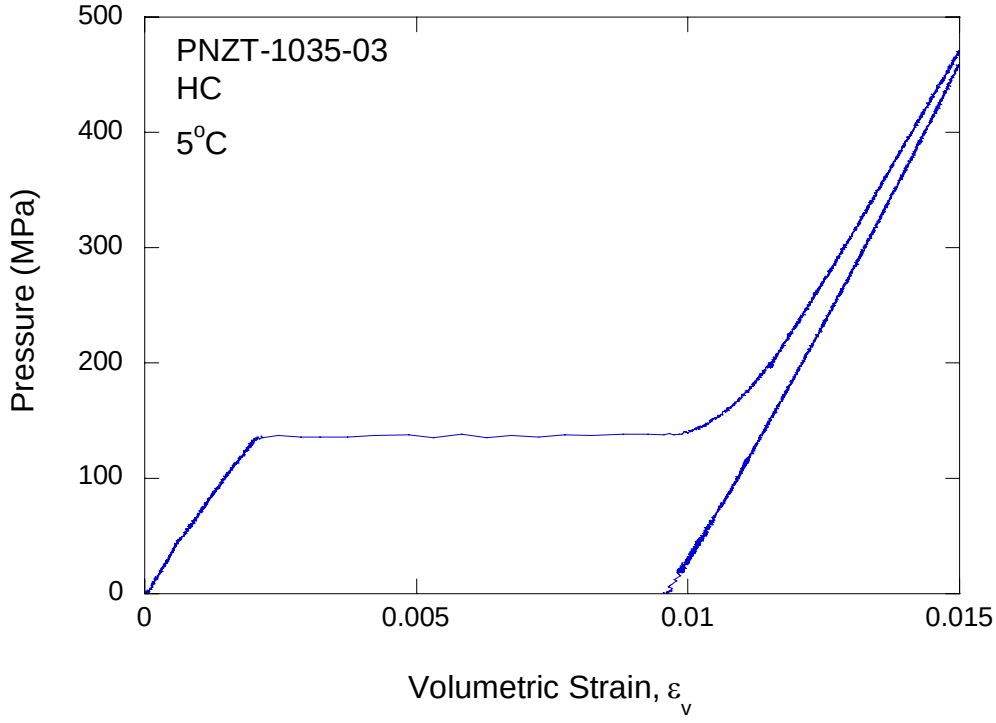
PNZT-1035-03
HC
5°C
Pressure (MPa)
Volumetric Strain, ε_v
0
100
200
300
400
500
0
0.005
0.01
0.015

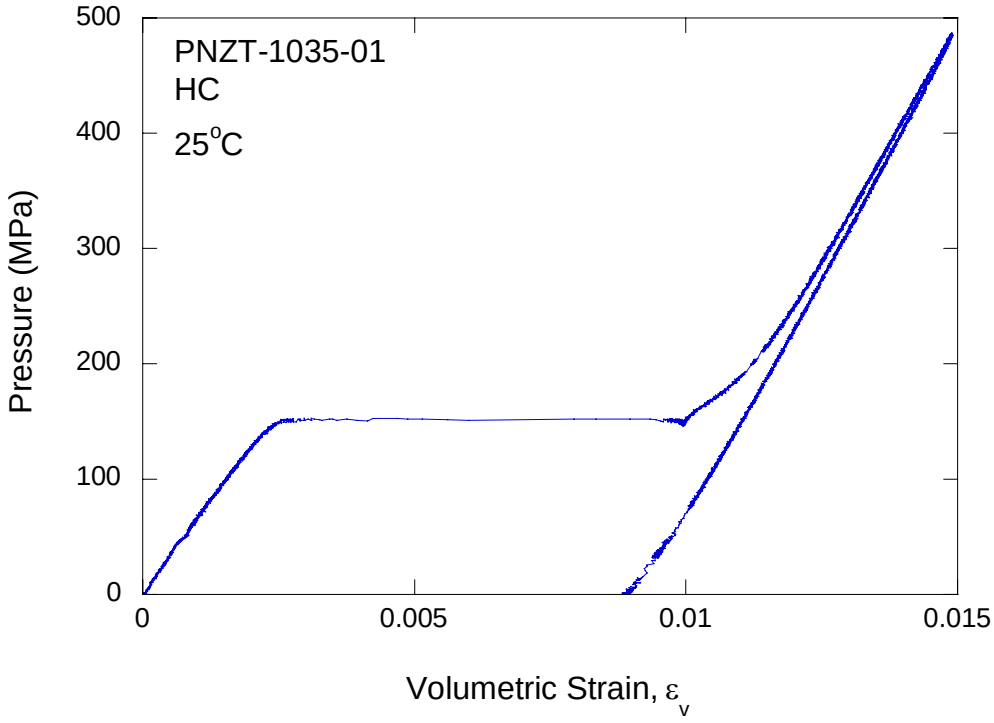
PNZT-1035-01
HC
25°C
Pressure (MPa)
Volumetric Strain, ε_v
0
100
200
300
400
500
0
0.005
0.01
0.015

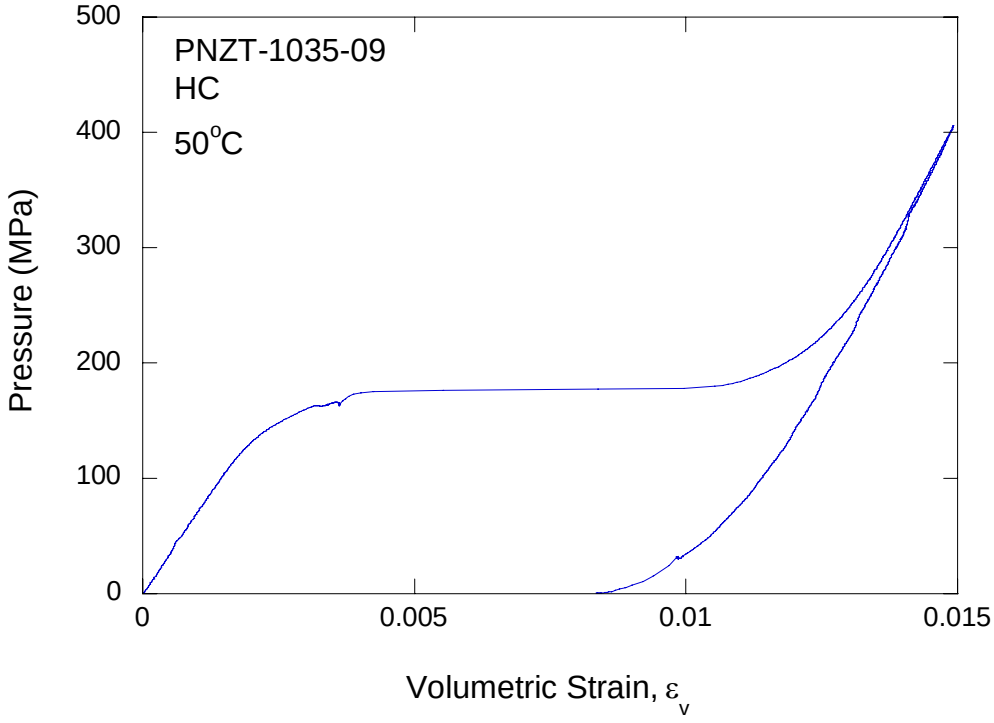
PNZT-1035-09
HC
50°C
Pressure (MPa)
Volumetric Strain, ε_v
0
100
200
300
400
500
0
0.005
0.01
0.015

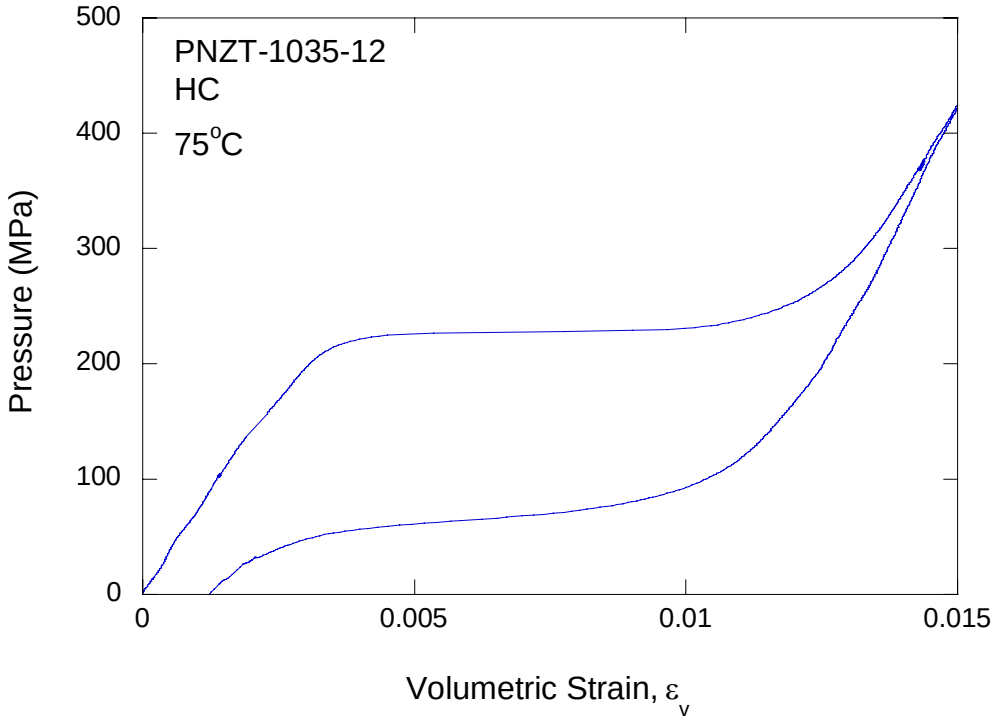
PNZT-1035-12
HC
75°C
Pressure (MPa)
500
400
300
200
100
0
0
0.005
0.01
0.015
Volumetric Strain, ε_v

APPENDIX A-2

Hydrostatic Compression Test (HC) Plots for Poled PNZT-HF1035

- σ_a-axial stress
- ε_a-axial strain
- $\varepsilon_{l\text{-parallel to poling}}$-lateral strain parallel to poling direction
- $\varepsilon_{l\text{-normal to poling}}$-lateral strain perpendicular to poling direction
- ε_v - volumetric strain
- T-temperature
- S-time in second

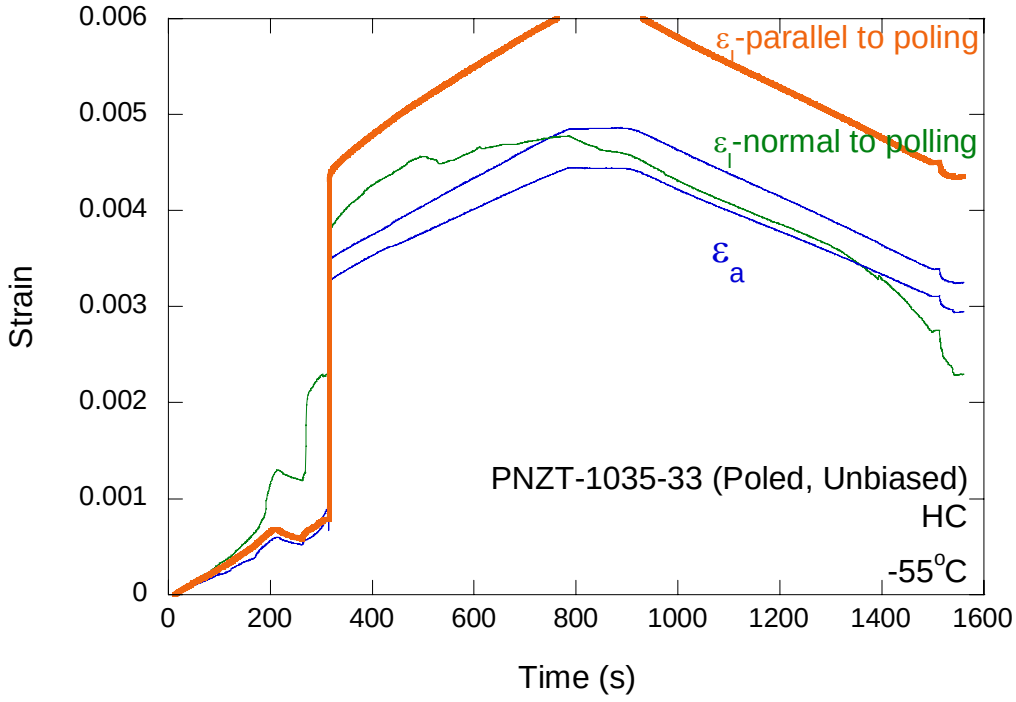
0.006
0.005
0.004
0.003
0.002
0.001
0
Strain
0
200
400
600
800
1000
1200
1400
1600
Time (s)
ε|-parallel to poling
ε|-normal to polling
εa
PNZT-1035-33 (Poled, Unbiased)
HC
-55°C

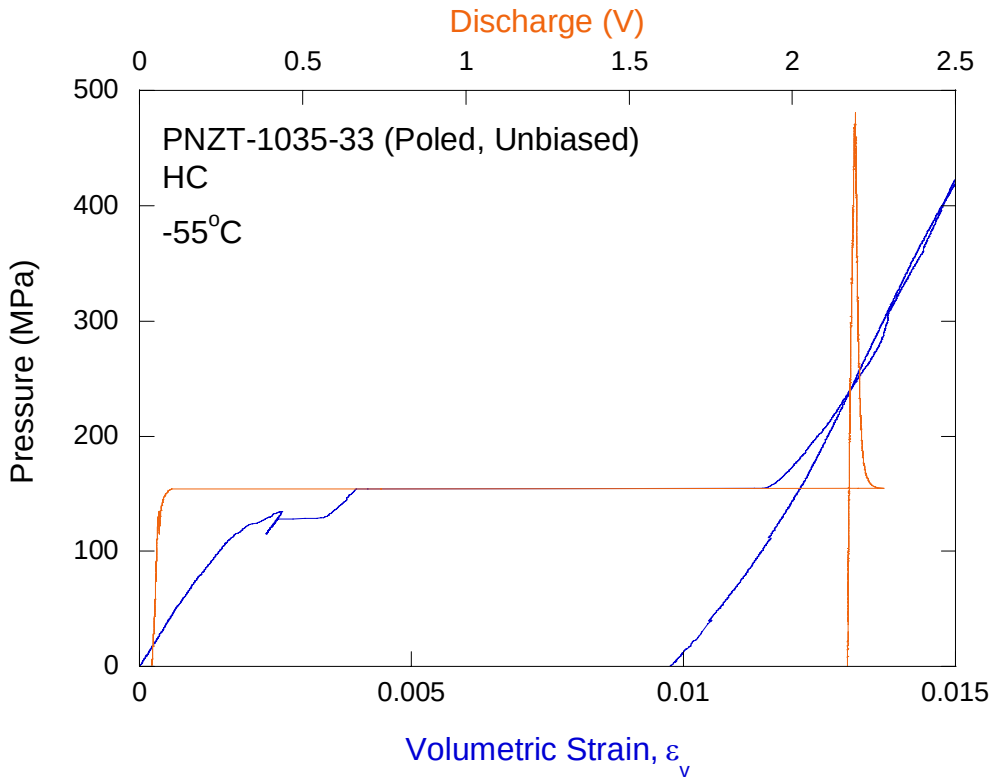
Discharge (V)
0
0.5
1
1.5
2
2.5
500
400
300
200
100
0
Pressure (MPa)
PNZT-1035-33 (Poled, Unbiased)
HC
-55°C
0
0.005
0.01
0.015
Volumetric Strain, εv

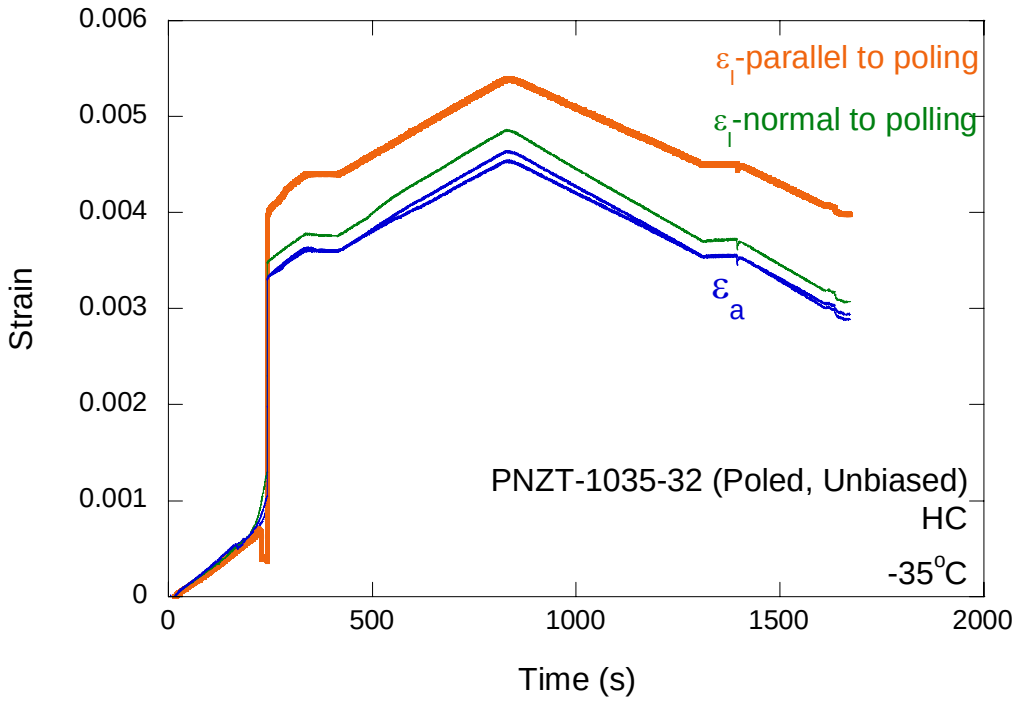
0.006
0.005
0.004
0.003
0.002
0.001
0
Strain
0
500
1000
1500
2000
Time (s)
ε_l-parallel to poling
ε_l-normal to polling
ε_a
PNZT-1035-32 (Poled, Unbiased)
HC
-35°C

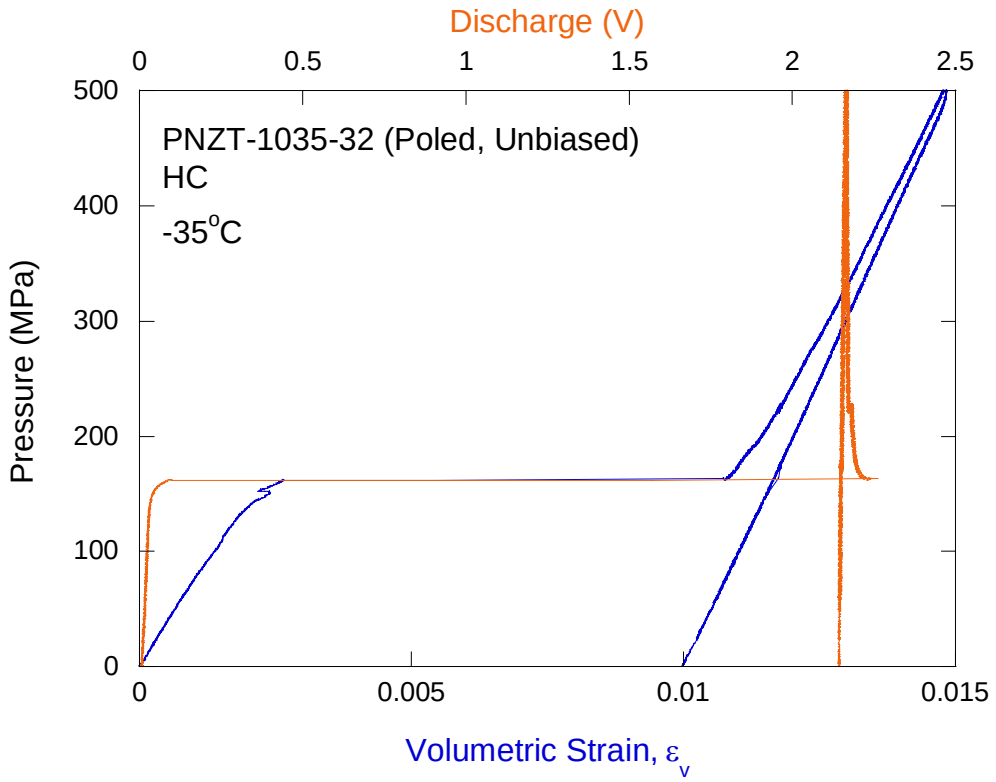
Discharge (V)
0
0.5
1
1.5
2
2.5
500
400
300
200
100
0
Pressure (MPa)
0
0.005
0.01
0.015
Volumetric Strain, ε_v
PNZT-1035-32 (Poled, Unbiased)
HC
-35°C

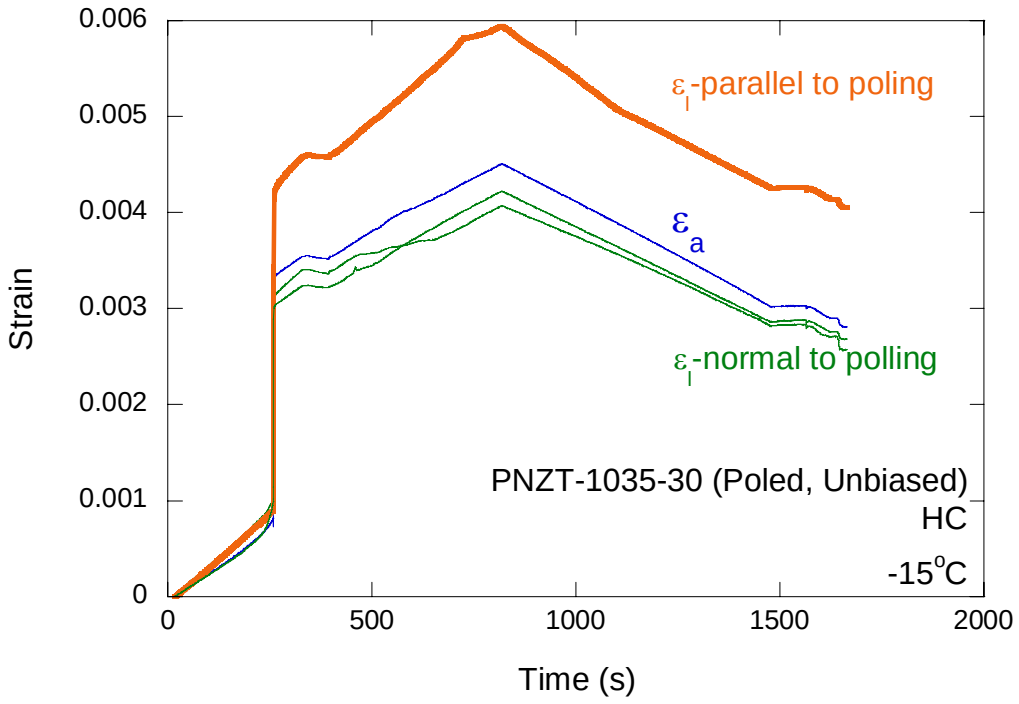
0.006
0.005
0.004
0.003
0.002
0.001
0
Strain
0
500
1000
1500
2000
Time (s)
ε_l-parallel to poling
ε_a
ε_l-normal to polling
PNZT-1035-30 (Poled, Unbiased)
HC
-15°C

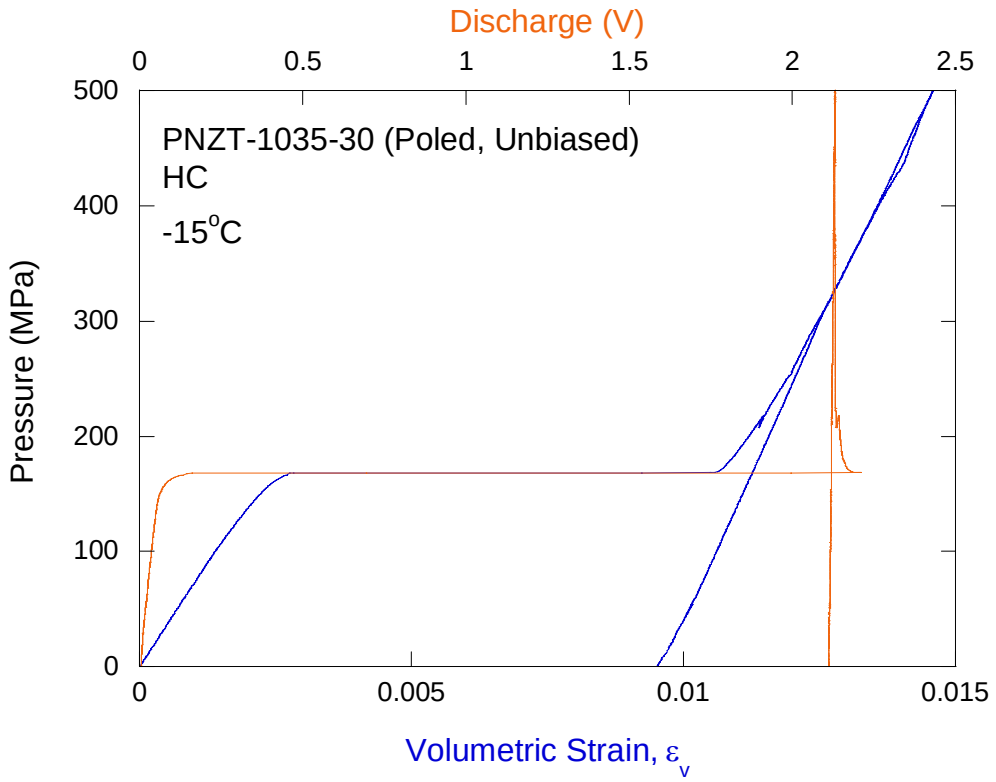
Discharge (V)
0
0.5
1
1.5
2
2.5
500
400
300
200
100
0
Pressure (MPa)
PNZT-1035-30 (Poled, Unbiased)
HC
-15°C
0
0.005
0.01
0.015
Volumetric Strain, ε_v

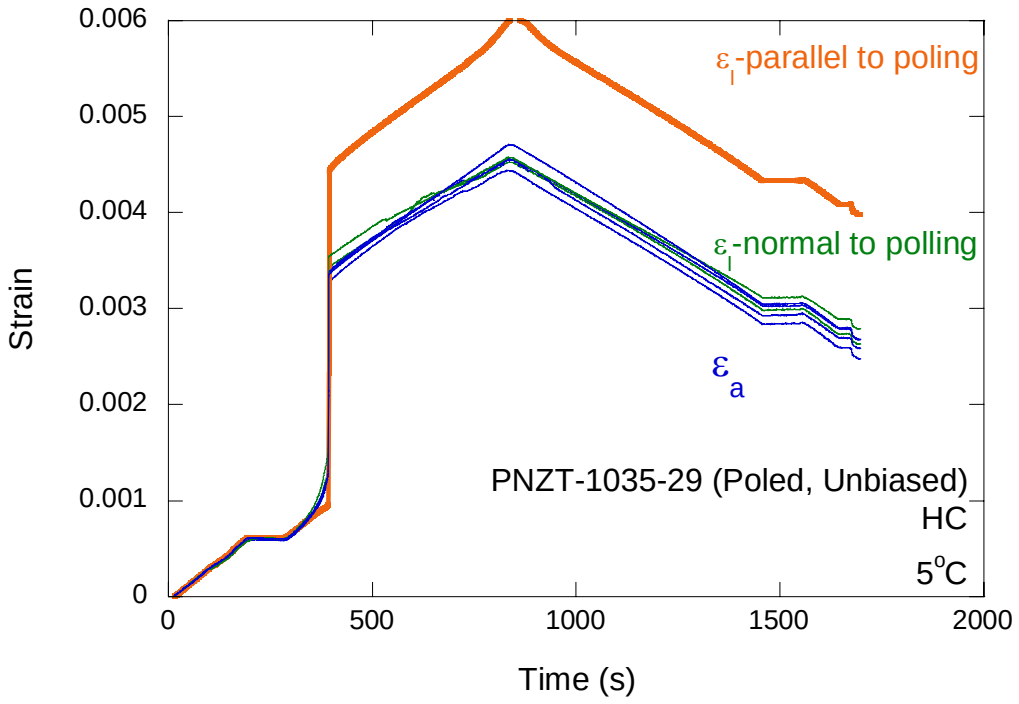
0.006
0.005
0.004
0.003
0.002
0.001
0
Strain
0
500
1000
1500
2000
Time (s)
ε_l-parallel to poling
ε_l-normal to polling
ε_a
PNZT-1035-29 (Poled, Unbiased)
HC
5°C

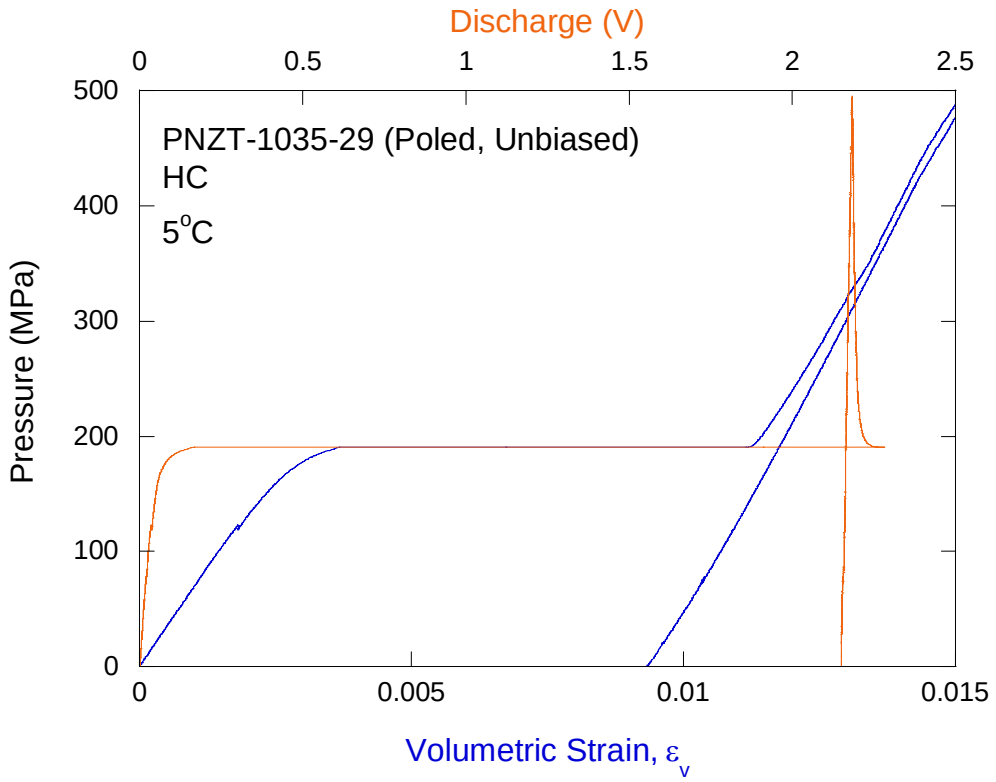
Discharge (V)
0
0.5
1
1.5
2
2.5
500
400
300
200
100
0
Pressure (MPa)
0
0.005
0.01
0.015
Volumetric Strain, ε_v
PNZT-1035-29 (Poled, Unbiased)
HC
5°C

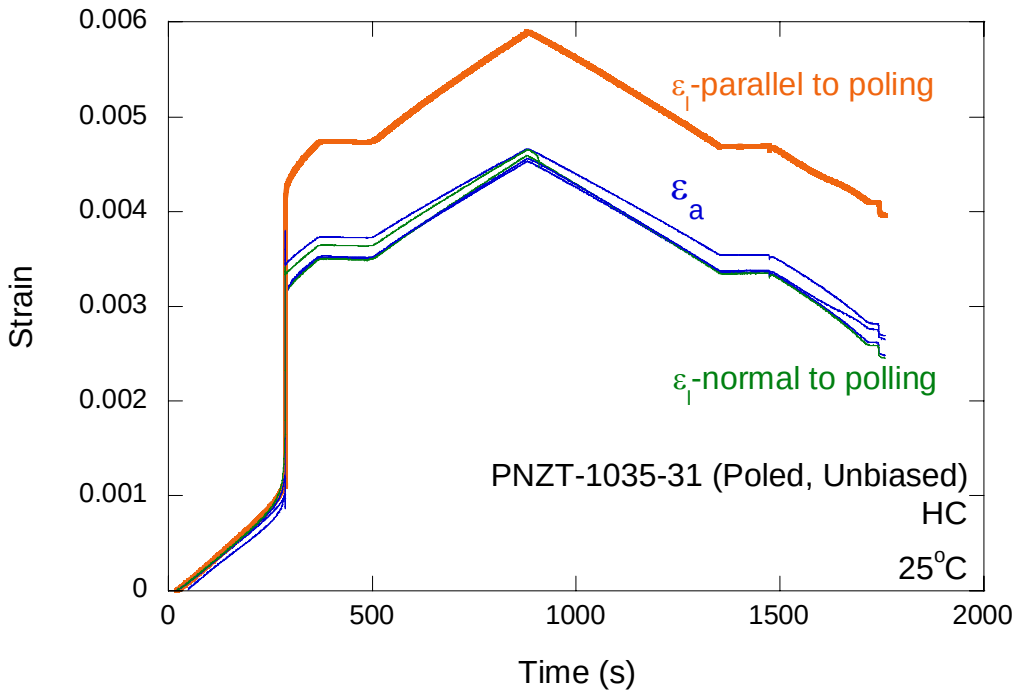
0.006
0.005
0.004
0.003
0.002
0.001
0
Strain
0
500
1000
1500
2000
Time (s)
ε_l-parallel to poling
ε_a
ε_l-normal to polling
PNZT-1035-31 (Poled, Unbiased)
HC
25°C

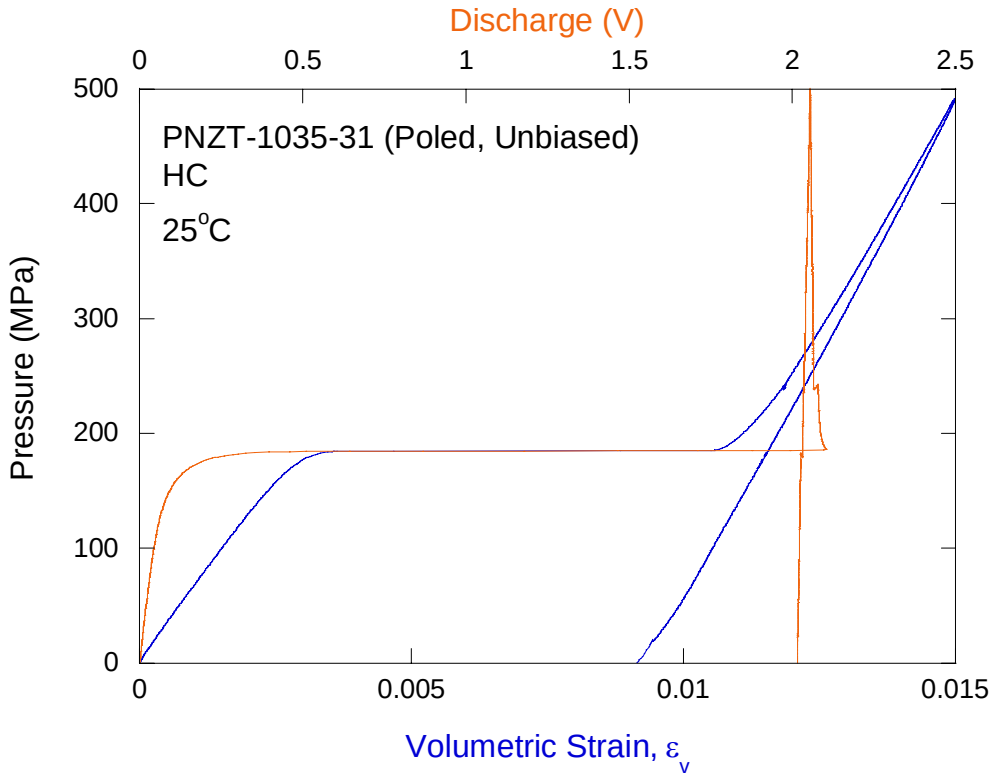
Discharge (V)
0
0.5
1
1.5
2
2.5
500
400
300
200
100
0
Pressure (MPa)
PNZT-1035-31 (Poled, Unbiased)
HC
25°C
0
0.005
0.01
0.015
Volumetric Strain, ε_v

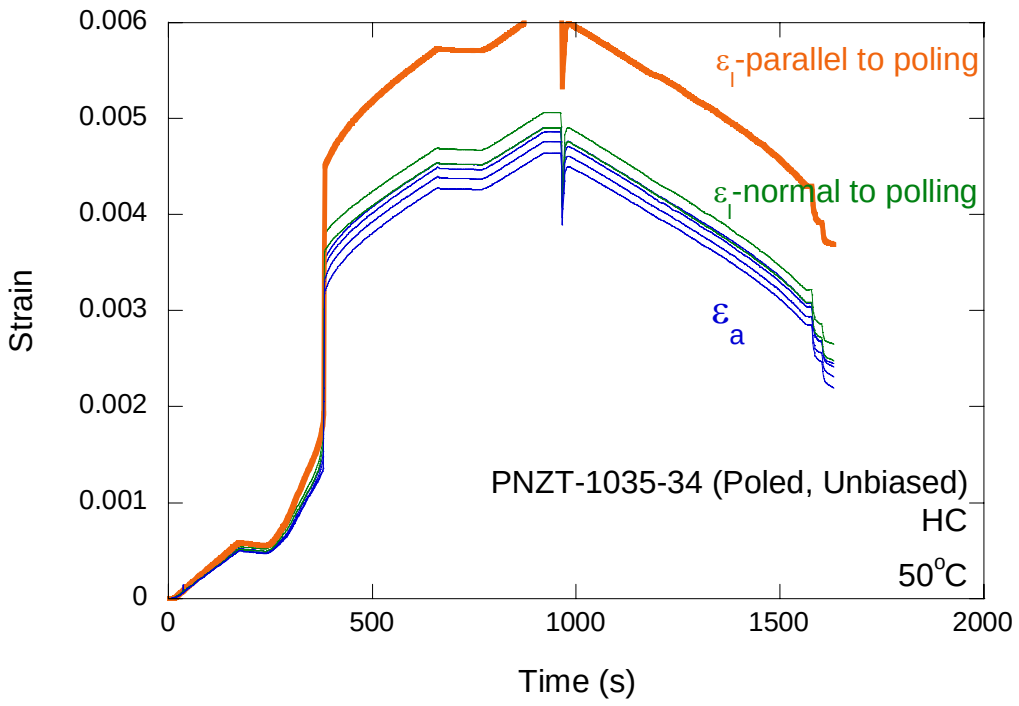
0.006
0.005
0.004
0.003
0.002
0.001
0
Strain
0
500
1000
1500
2000
Time (s)
ε_l-parallel to poling
ε_l-normal to polling
ε_a
PNZT-1035-34 (Poled, Unbiased)
HC
50°C

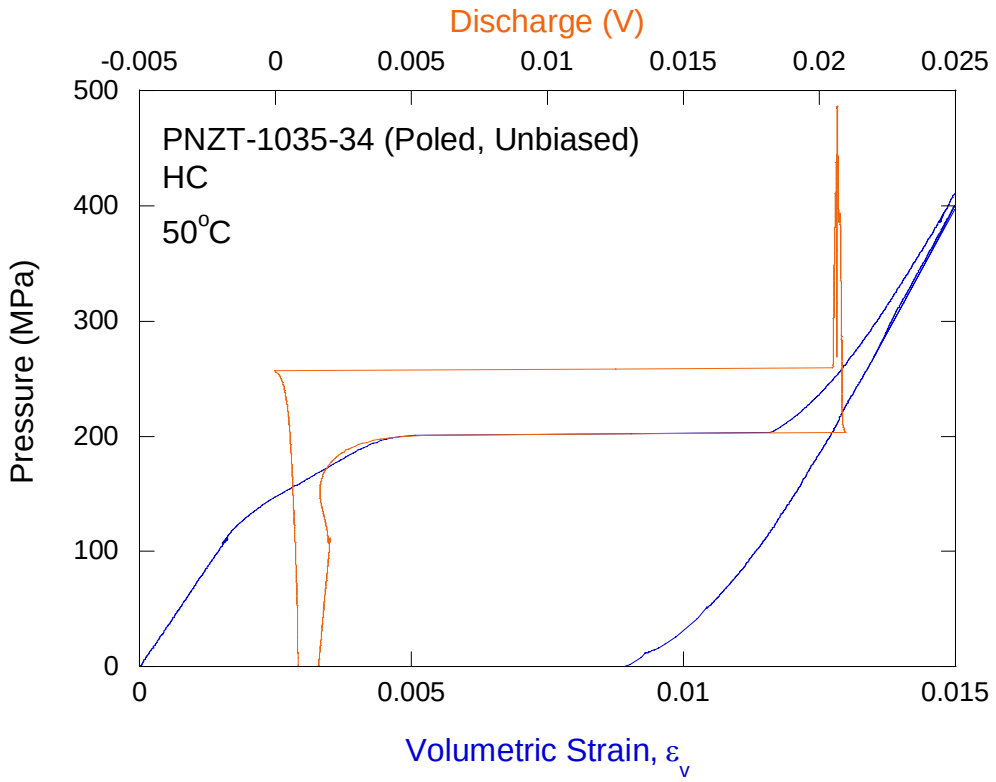
Discharge (V)
-0.005
0
0.005
0.01
0.015
0.02
0.025
500
400
300
200
100
0
Pressure (MPa)
0
0.005
0.01
0.015
Volumetric Strain, ε_v
PNZT-1035-34 (Poled, Unbiased)
HC
50°C

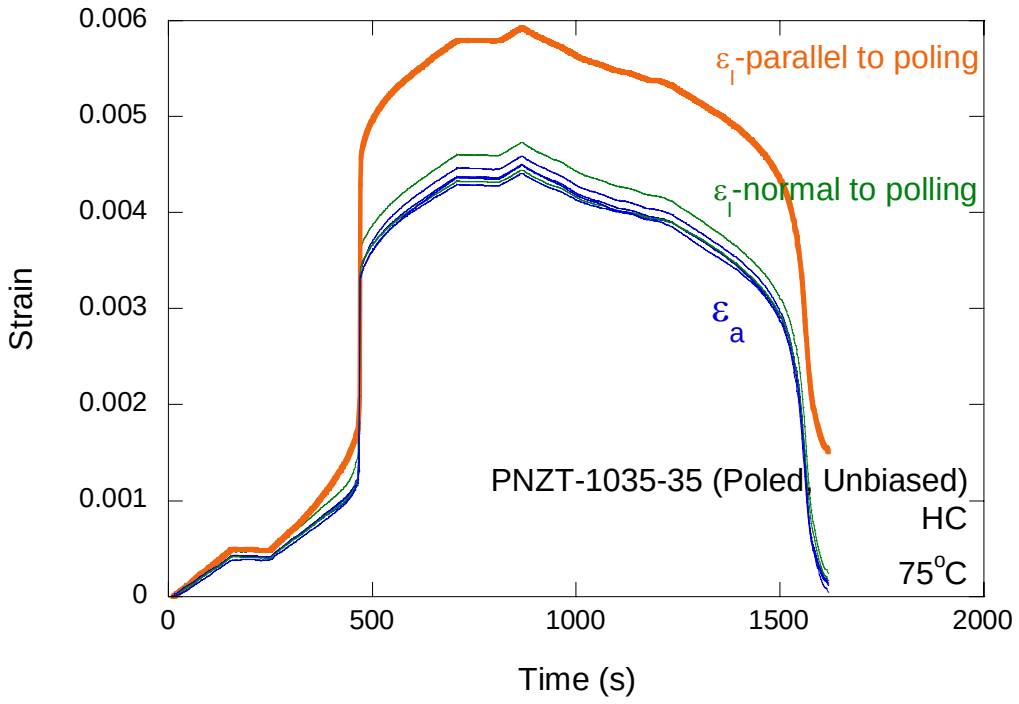
0.006
0.005
0.004
0.003
0.002
0.001
0
Strain
0
500
1000
1500
2000
Time (s)
ε_l-parallel to poling
ε_l-normal to polling
ε_a
PNZT-1035-35 (Poled, Unbiased)
HC
75°C

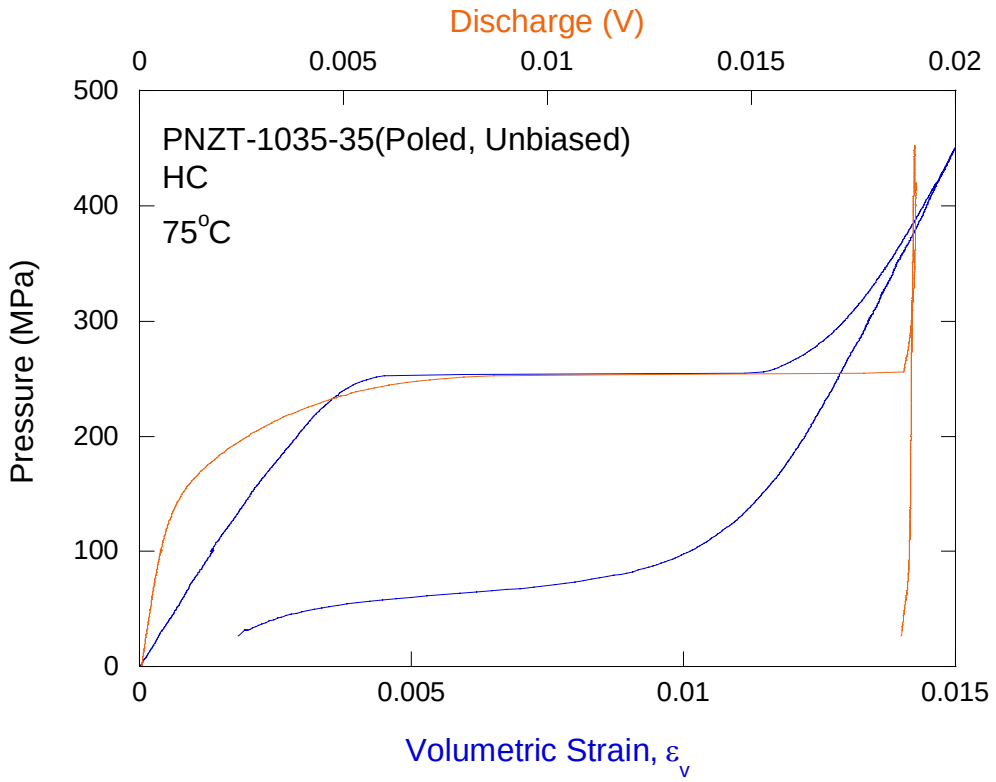
Discharge (V)
0
0.005
0.01
0.015
0.02
500
400
300
200
100
0
Pressure (MPa)
PNZT-1035-35(Poled, Unbiased)
HC
75°C
0
0.005
0.01
0.015
Volumetric Strain, ε_v

APPENDIX B-1

Uniaxial Compression Test (UC) Plots for Unpoled PNZT-HF1035

- σ_a-axial stress
- ε_a-axial strain
- ε_l-lateral strain
- ε_v-volumetric strain

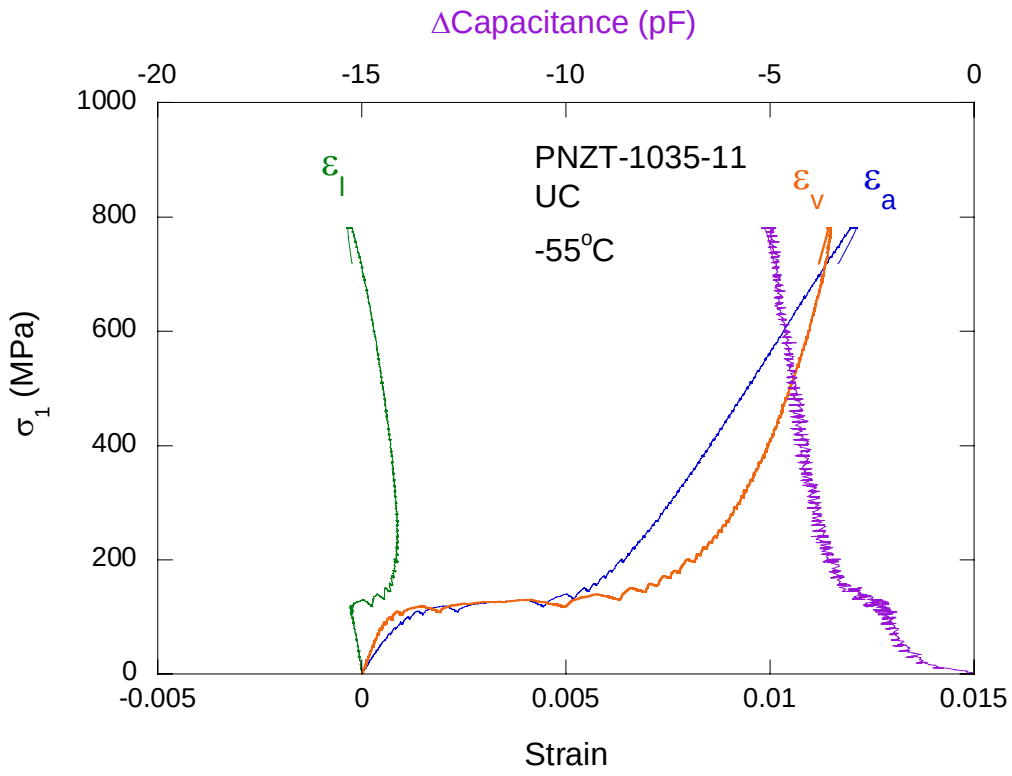
ΔCapacitance (pF)
-20
-15
-10
-5
0
1000
800
600
400
200
0
σ1 (MPa)
εl
εv
εa
PNZT-1035-11
UC
-55°C
-0.005
0
0.005
0.01
0.015
Strain

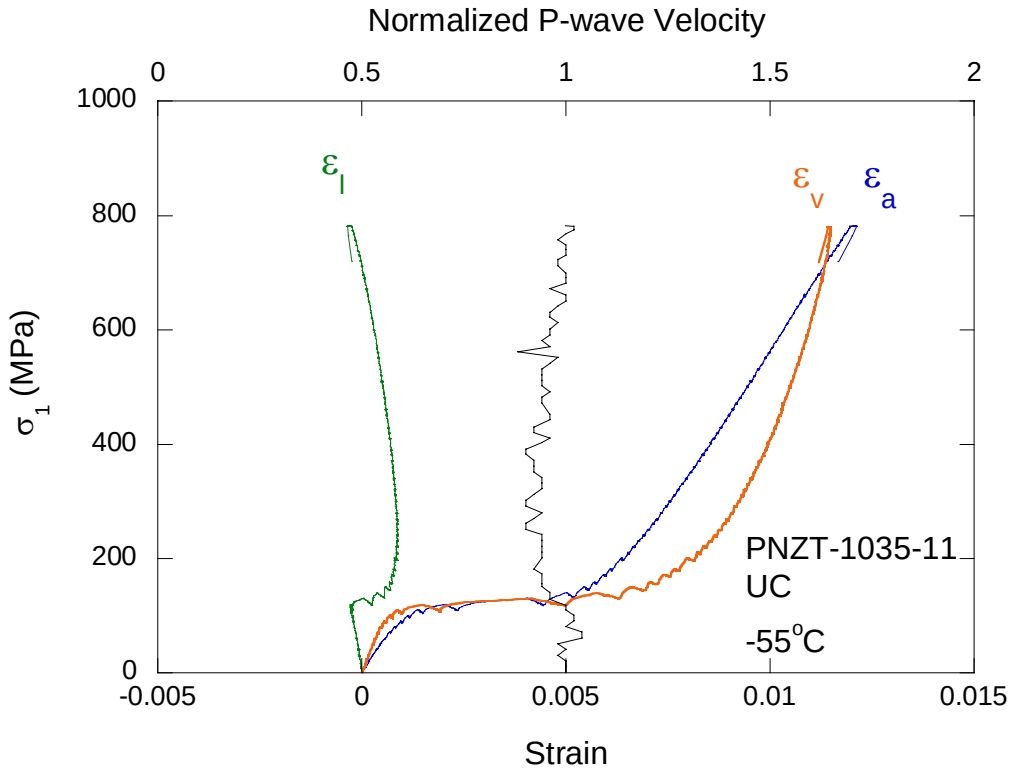
Normalized P-wave Velocity
0
0.5
1
1.5
2
1000
800
600
400
200
0
σ1 (MPa)
εl
εv
εa
PNZT-1035-11
UC
-55°C
-0.005
0
0.005
0.01
0.015
Strain

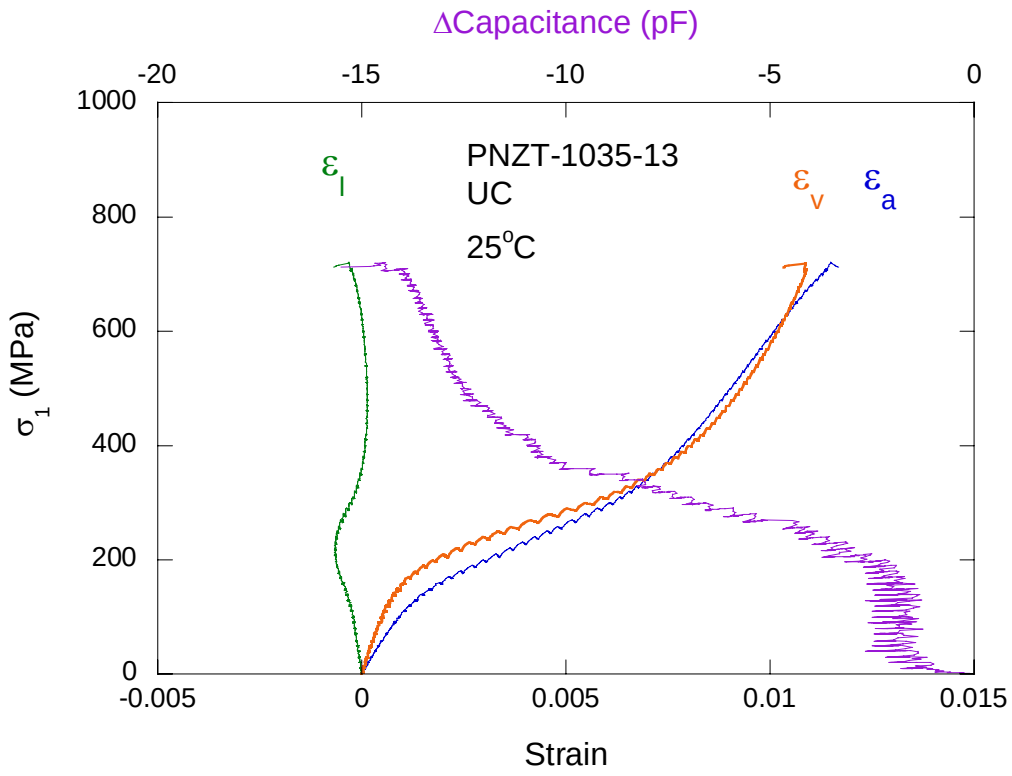
ΔCapacitance (pF)
-20
-15
-10
-5
0
1000
800
600
400
200
0
σ1 (MPa)
εl
PNZT-1035-13
UC
25°C
εv
εa
-0.005
0
0.005
0.01
0.015
Strain

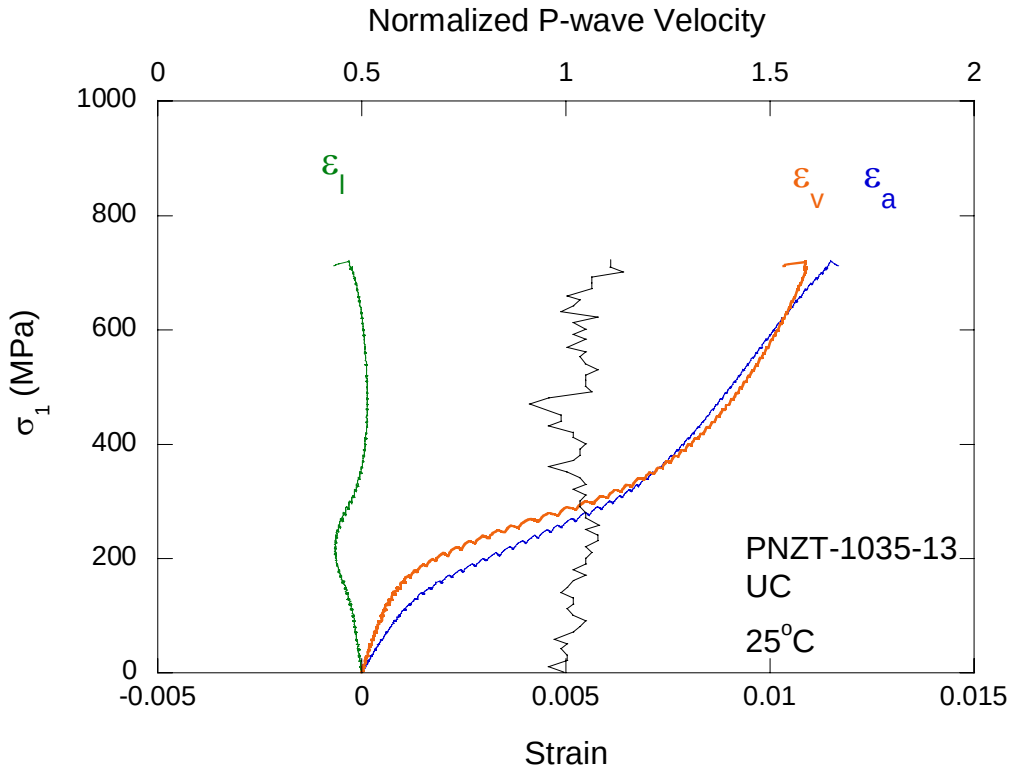
Normalized P-wave Velocity
0
0.5
1
1.5
2
1000
800
600
400
200
0
σ1 (MPa)
εl
εv
εa
PNZT-1035-13
UC
25°C
-0.005
0
0.005
0.01
0.015
Strain

APPENDIX B-2

Uniaxial Compression Test (UC) Plots for Poled PNZT-HF1035

- σ_a-axial stress
- ε_a-axial strain
- $\varepsilon_{l\text{-parallel to poling}}$-lateral strain parallel to poling direction
- $\varepsilon_{l\text{-normal to poling}}$-lateral strain perpendicular to poling direction

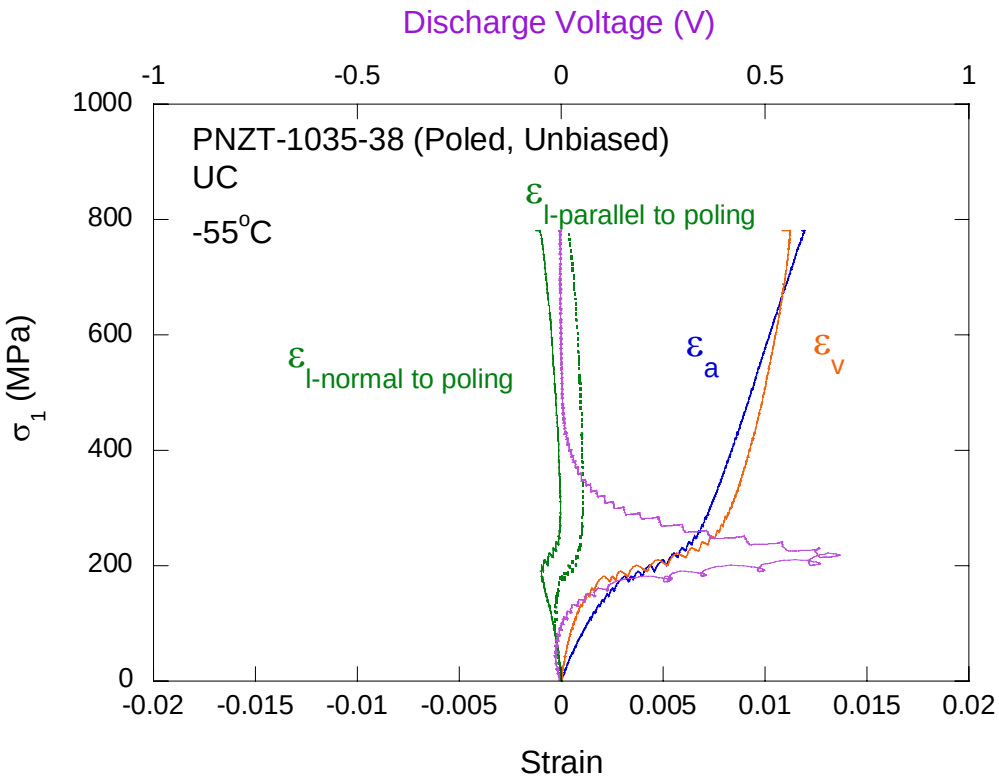
Discharge Voltage (V)
-1
-0.5
0
0.5
1
PNZT-1035-38 (Poled, Unbiased)
UC
-55°C
ε l-parallel to poling
ε l-normal to poling
ε a
ε v
σ 1 (MPa)
1000
800
600
400
200
0
-0.02
-0.015
-0.01
-0.005
0
0.005
0.01
0.015
0.02
Strain

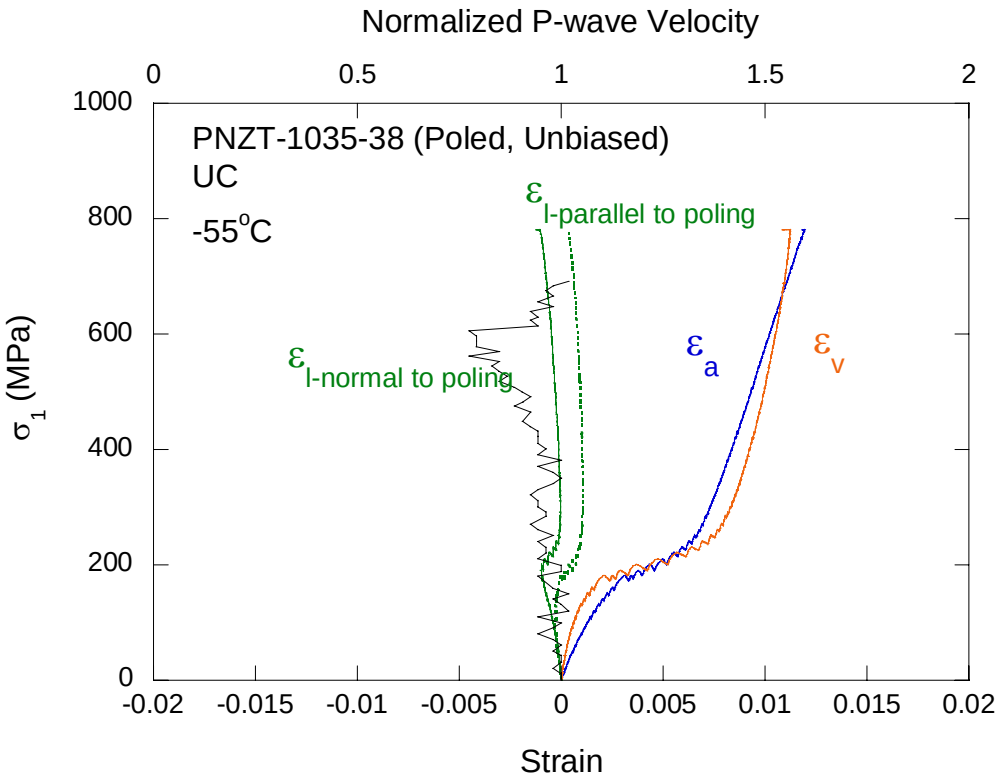
Normalized P-wave Velocity
0
0.5
1
1.5
2
PNZT-1035-38 (Poled, Unbiased)
UC
-55°C
ε l-parallel to poling
ε l-normal to poling
ε a
ε v
σ 1 (MPa)
1000
800
600
400
200
0
-0.02
-0.015
-0.01
-0.005
0
0.005
0.01
0.015
0.02
Strain

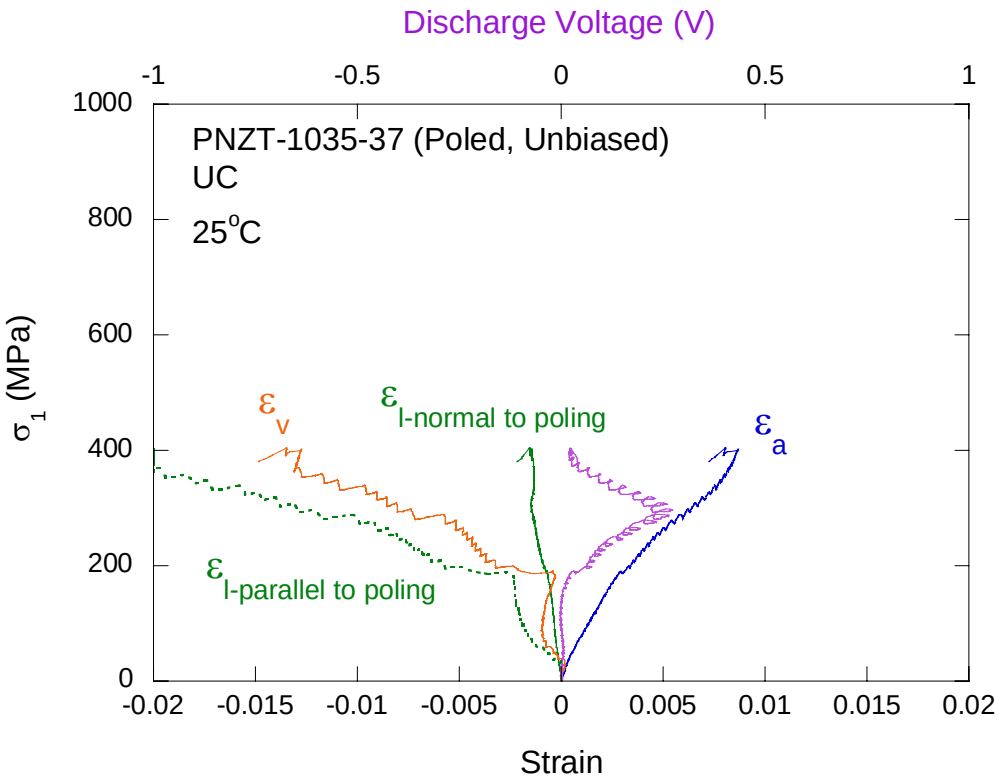
Discharge Voltage (V)
-1
-0.5
0
0.5
1
PNZT-1035-37 (Poled, Unbiased)
UC
25°C
σ1 (MPa)
εv
εl-normal to poling
εa
εl-parallel to poling
Strain

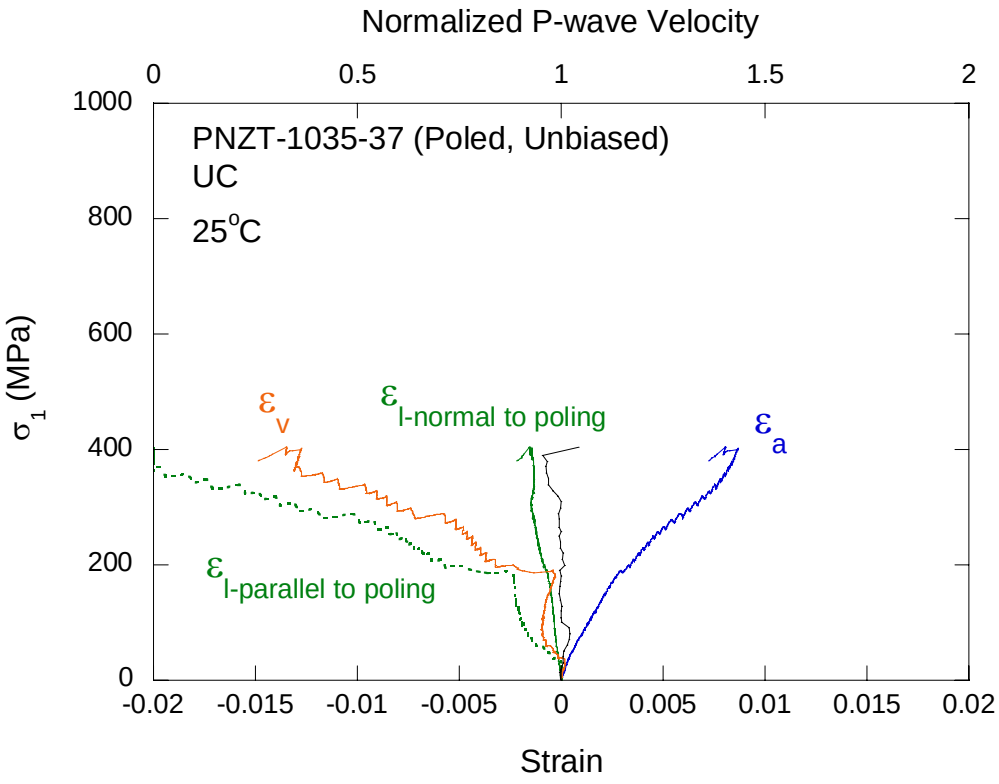
Normalized P-wave Velocity
0
0.5
1
1.5
2
PNZT-1035-37 (Poled, Unbiased)
UC
25°C
σ1 (MPa)
εv
εl-normal to poling
εa
εl-parallel to poling
Strain

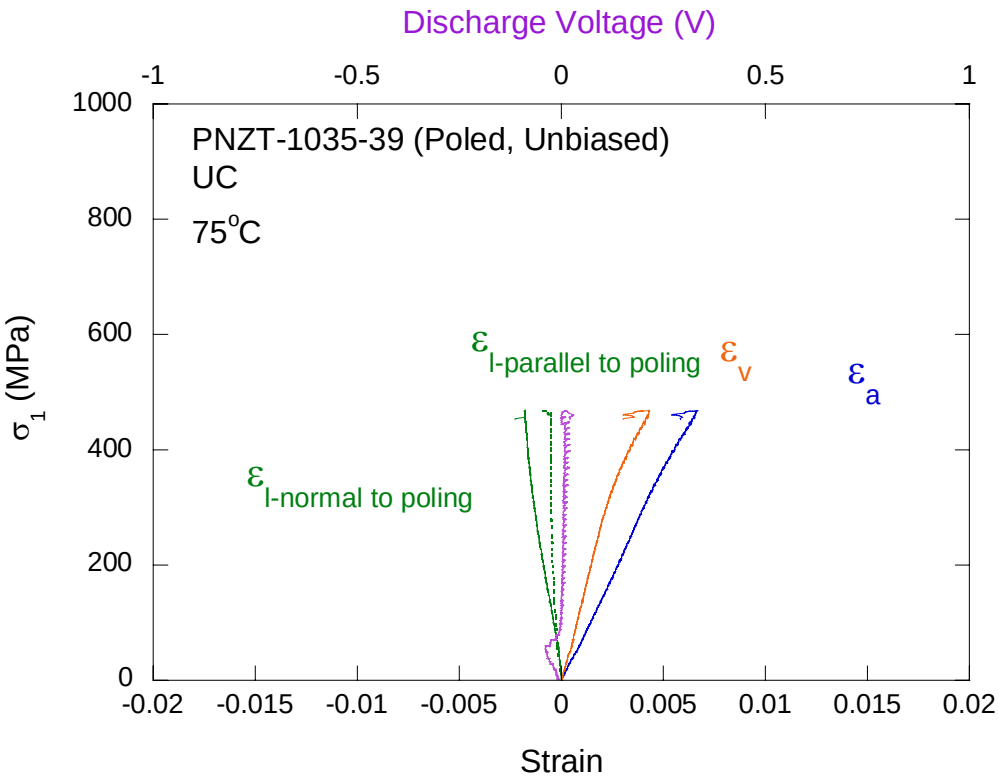
Discharge Voltage (V)
-1
-0.5
0
0.5
1
PNZT-1035-39 (Poled, Unbiased)
UC
75°C
ε l-parallel to poling
ε v
ε a
ε l-normal to poling
σ 1 (MPa)
1000
800
600
400
200
0
-0.02
-0.015
-0.01
-0.005
0
0.005
0.01
0.015
0.02
Strain

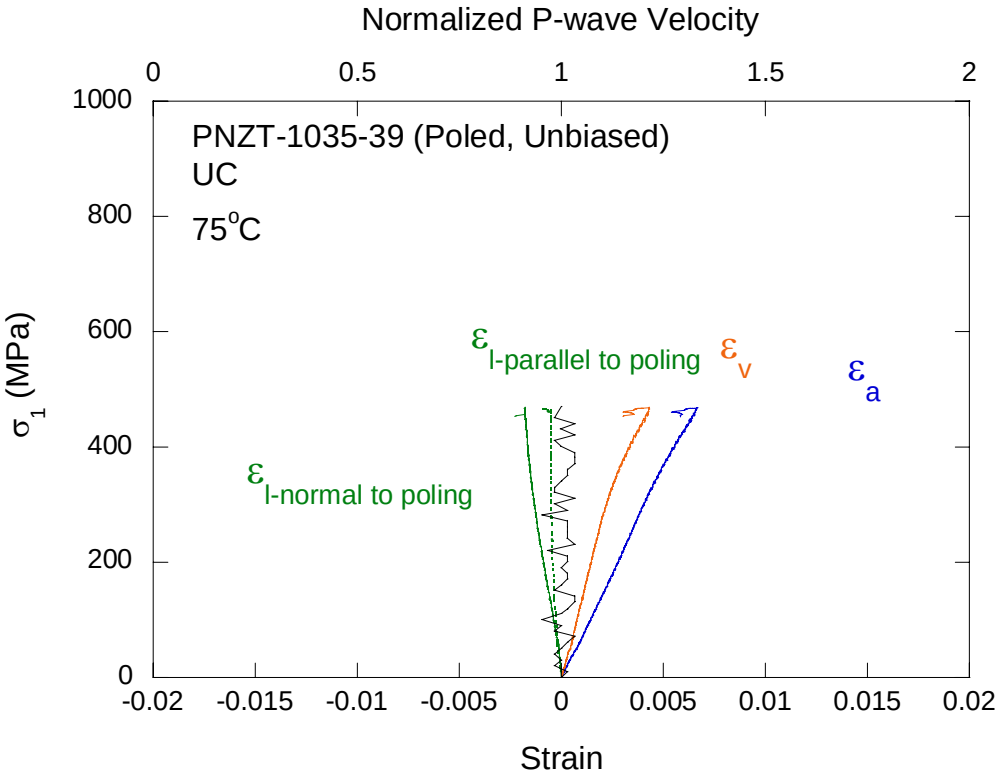
Normalized P-wave Velocity
0
0.5
1
1.5
2
PNZT-1035-39 (Poled, Unbiased)
UC
75°C
ε l-parallel to poling
ε v
ε a
ε l-normal to poling
σ 1 (MPa)
1000
800
600
400
200
0
-0.02
-0.015
-0.01
-0.005
0
0.005
0.01
0.015
0.02
Strain

APPENDIX C-1

Constant Stress Difference Test (CSD) Plots for Unpoled PNZT-HF1035

- σ_1- maximum principal stress acting in the long axis of the specimen,
- σ_3- confining pressure acting as the minor principal stress
- ε_a-axial strain
- ε_l -lateral strain

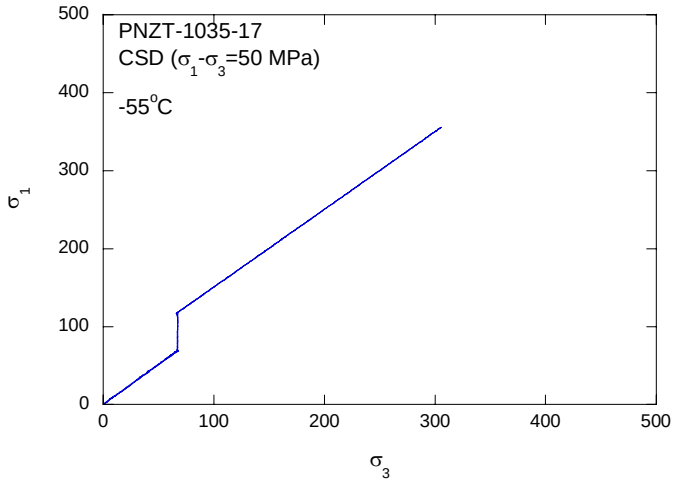
PNZT-1035-17
CSD (σ1-σ3=50 MPa)
-55°C
σ1
σ3
0
100
200
300
400
500

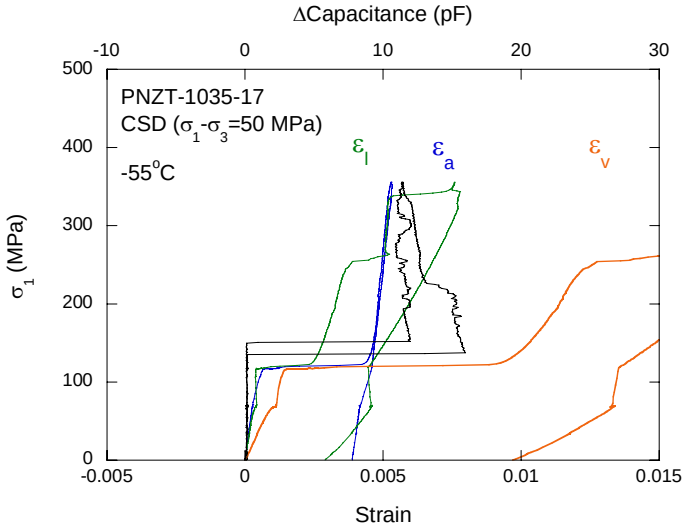
ΔCapacitance (pF)
-10
0
10
20
30
PNZT-1035-17
CSD (σ1-σ3=50 MPa)
-55°C
εl
εa
εv
σ1 (MPa)
Strain
-0.005
0
0.005
0.01
0.015

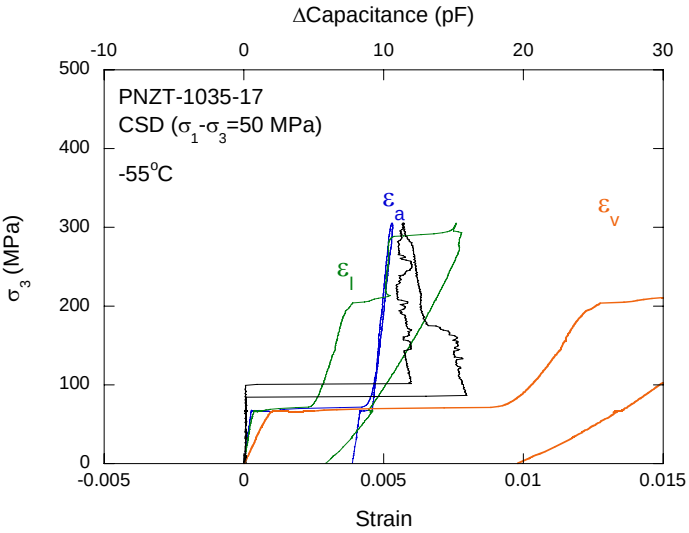
ΔCapacitance (pF)
-10
0
10
20
30
PNZT-1035-17
CSD (σ1-σ3=50 MPa)
-55°C
εa
εv
εl
σ3 (MPa)
Strain
-0.005
0
0.005
0.01
0.015

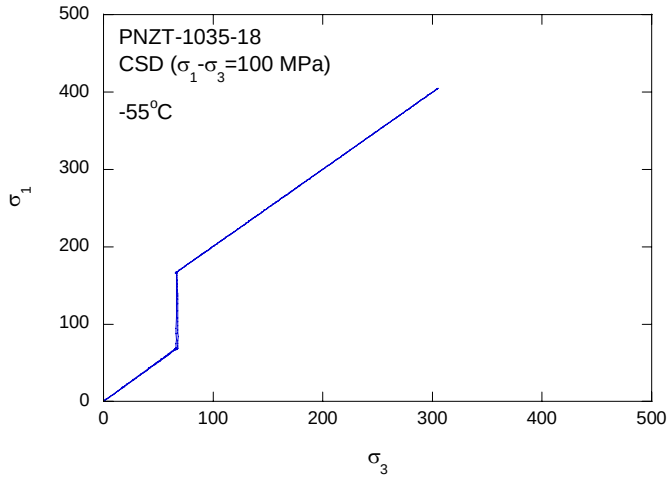
PNZT-1035-18
CSD (σ_1-σ_3=100 MPa)
-55°C
σ_1
σ_3
0
100
200
300
400
500

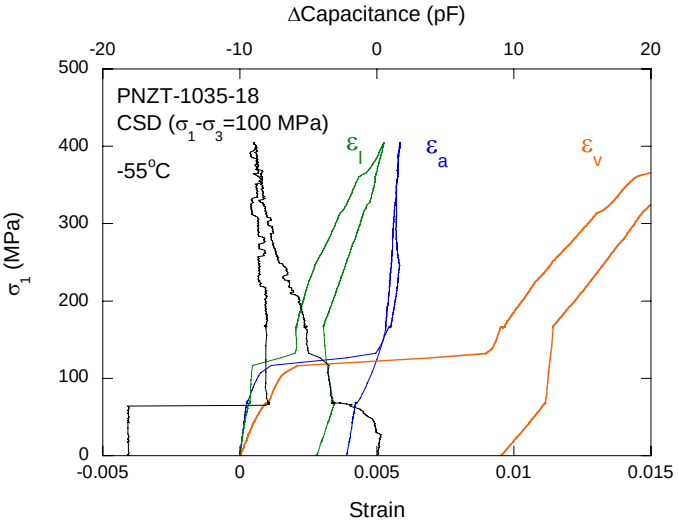
ΔCapacitance (pF)
-20
-10
0
10
20
PNZT-1035-18
CSD (σ_1-σ_3=100 MPa)
-55°C
ε_l
ε_a
ε_v
σ_1 (MPa)
Strain
-0.005
0
0.005
0.01
0.015

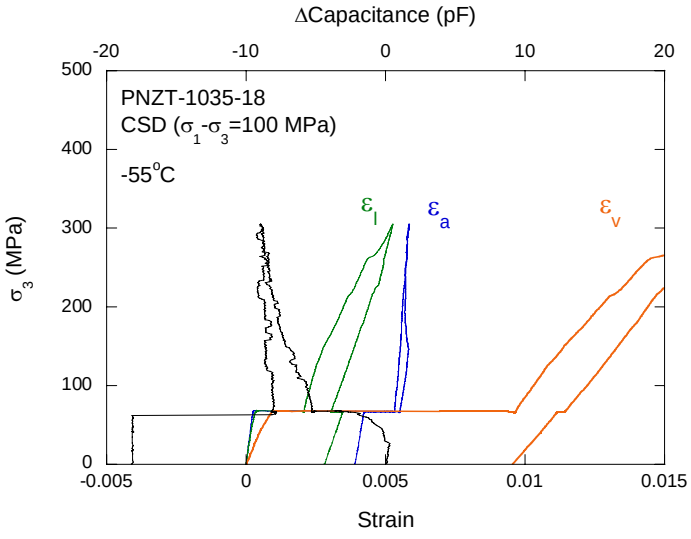
ΔCapacitance (pF)
-20
-10
0
10
20
PNZT-1035-18
CSD (σ_1-σ_3=100 MPa)
-55°C
ε_l
ε_a
ε_v
σ_3 (MPa)
Strain
-0.005
0
0.005
0.01
0.015

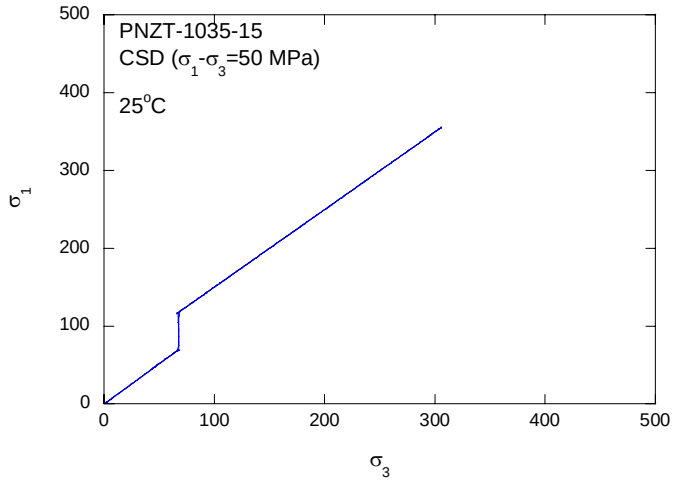
PNZT-1035-15
CSD (σ1-σ3=50 MPa)
25°C
σ1
σ3
0
100
200
300
400
500

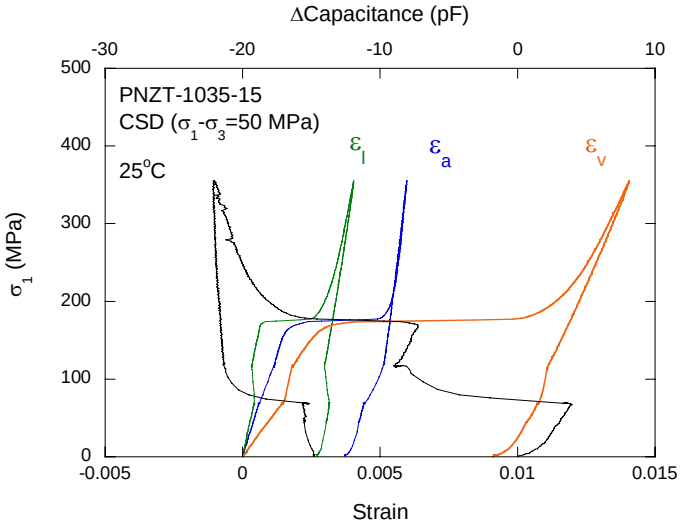
ΔCapacitance (pF)
-30
-20
-10
0
10
PNZT-1035-15
CSD (σ1-σ3=50 MPa)
25°C
εl
εa
εv
σ1 (MPa)
Strain
-0.005
0
0.005
0.01
0.015

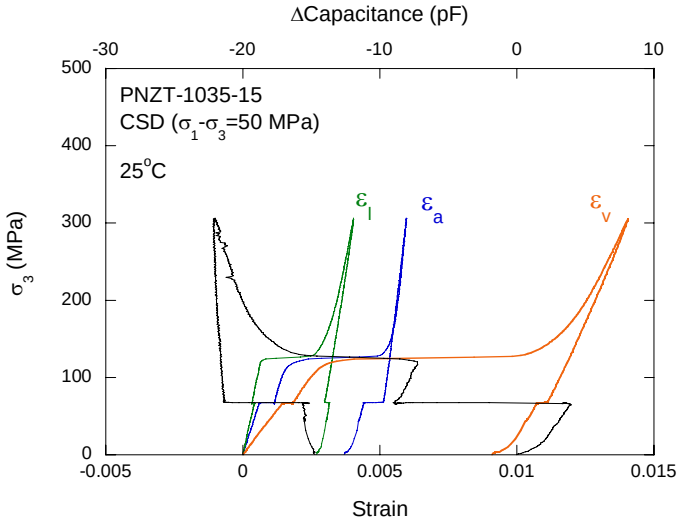
ΔCapacitance (pF)
-30
-20
-10
0
10
PNZT-1035-15
CSD (σ1-σ3=50 MPa)
25°C
εl
εa
εv
σ3 (MPa)
Strain
-0.005
0
0.005
0.01
0.015

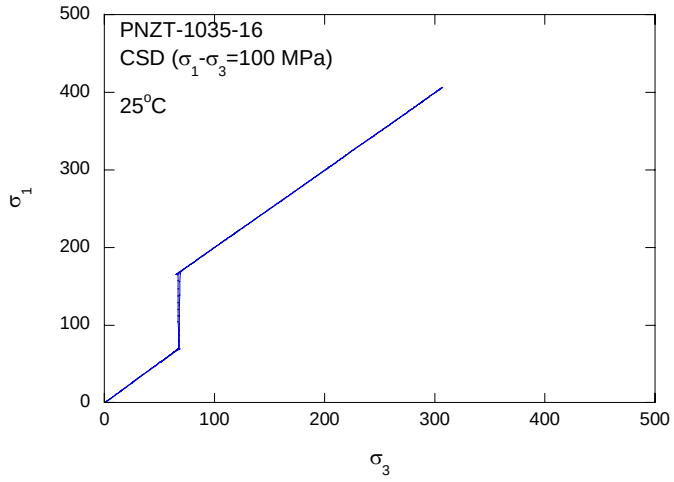
PNZT-1035-16
CSD (σ1-σ3=100 MPa)
25°C
σ1
σ3
0
100
200
300
400
500

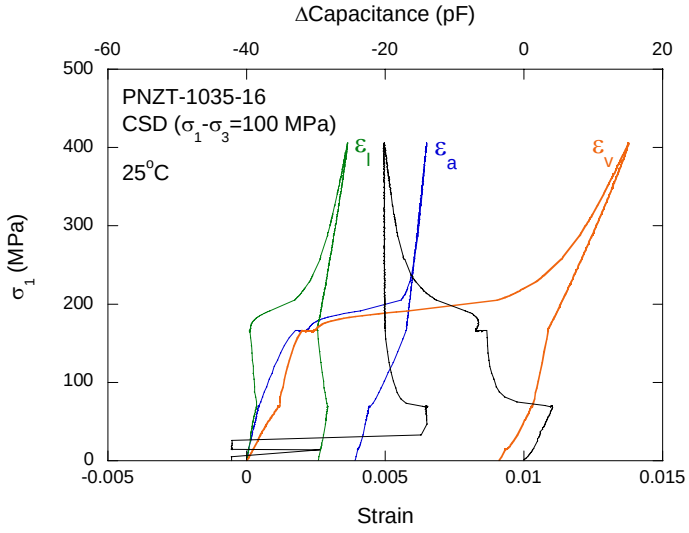
ΔCapacitance (pF)
-60
-40
-20
0
20
PNZT-1035-16
CSD (σ1-σ3=100 MPa)
25°C
εl
εa
εv
σ1 (MPa)
Strain
-0.005
0
0.005
0.01
0.015

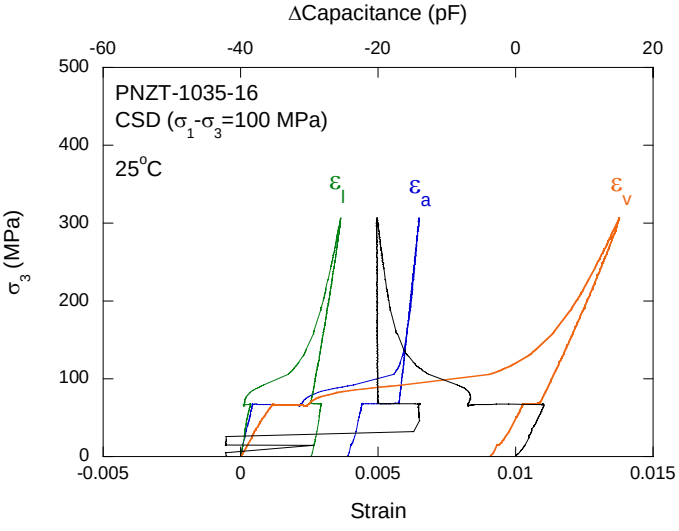
ΔCapacitance (pF)
-60
-40
-20
0
20
PNZT-1035-16
CSD (σ1-σ3=100 MPa)
25°C
εl
εa
εv
σ3 (MPa)
Strain
-0.005
0
0.005
0.01
0.015

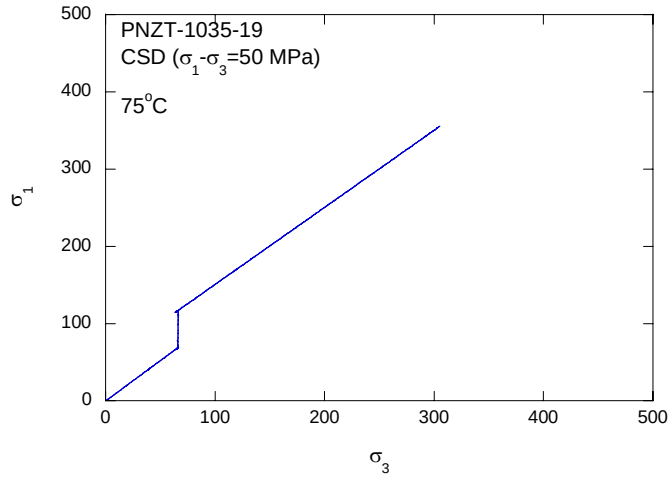
PNZT-1035-19
CSD (σ1-σ3=50 MPa)
75°C
σ1
σ3
0
100
200
300
400
500

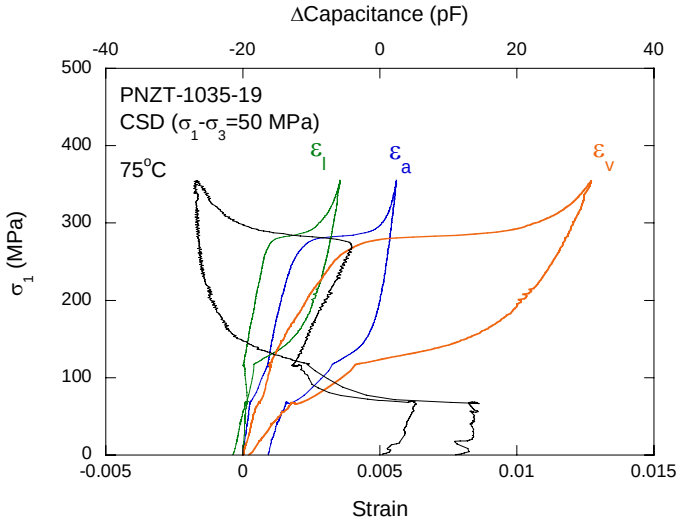
ΔCapacitance (pF)
-40
-20
0
20
40
PNZT-1035-19
CSD (σ1-σ3=50 MPa)
75°C
εl
εa
εv
σ1 (MPa)
Strain
-0.005
0
0.005
0.01
0.015

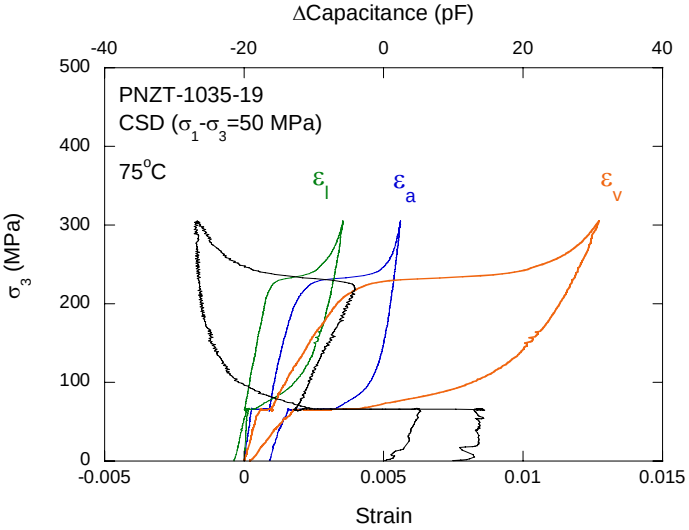
ΔCapacitance (pF)
-40
-20
0
20
40
PNZT-1035-19
CSD (σ1-σ3=50 MPa)
75°C
εl
εa
εv
σ3 (MPa)
Strain
-0.005
0
0.005
0.01
0.015

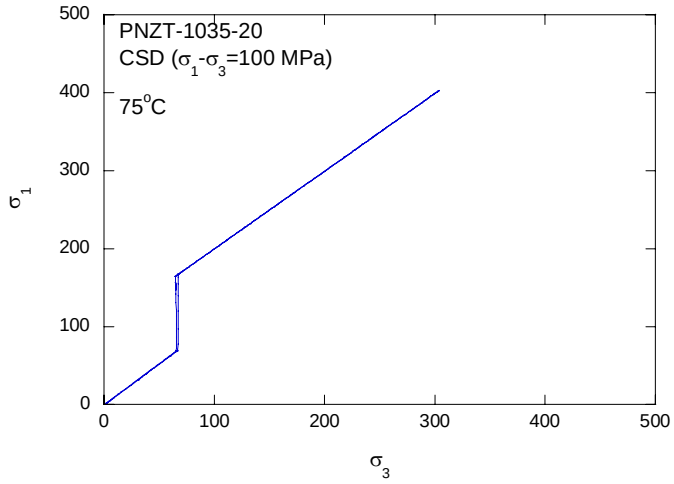
PNZT-1035-20
CSD (σ1-σ3=100 MPa)
75°C
σ1
σ3
0
100
200
300
400
500

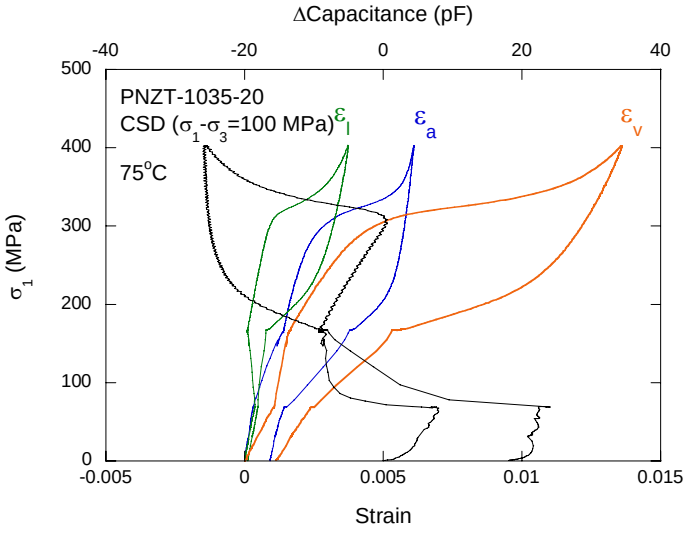
ΔCapacitance (pF)
-40
-20
0
20
40
PNZT-1035-20
CSD (σ1-σ3=100 MPa)
75°C
εl
εa
εv
σ1 (MPa)
Strain
-0.005
0
0.005
0.01
0.015

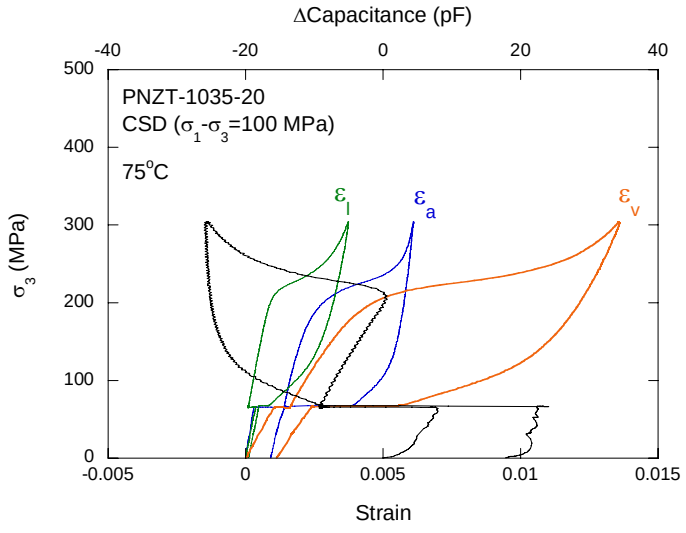
ΔCapacitance (pF)
-40
-20
0
20
40
PNZT-1035-20
CSD (σ1-σ3=100 MPa)
75°C
εl
εa
εv
σ3 (MPa)
Strain
-0.005
0
0.005
0.01
0.015

APPENDIX C-2

Constant Stress Difference Test (CSD) Plots for Poled PNZT-HF1035

- σ_1- maximum principal stress acting in the long axis of the specimen
- σ_3- confining pressure acting as the minor principal stress
- ε_a-axial strain
- $\varepsilon_{l\text{-parallel to poling}}$-lateral strain parallel to poling direction
- $\varepsilon_{l\text{-normal to poling}}$-lateral strain perpendicular to poling direction

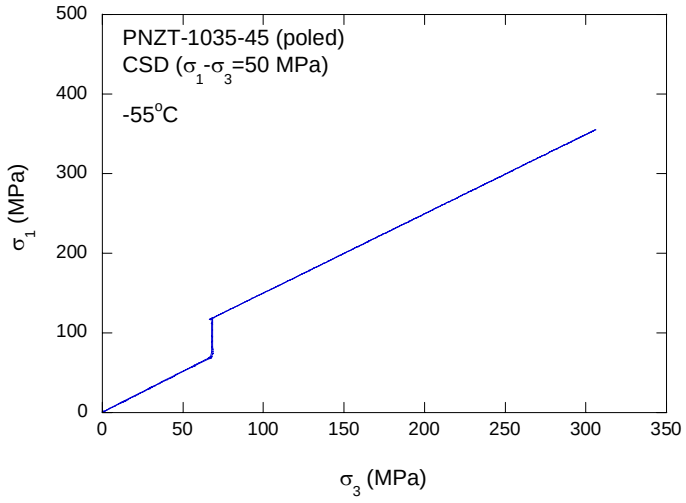
PNZT-1035-45 (poled)
CSD (σ1-σ3=50 MPa)
-55°C
σ1 (MPa)
σ3 (MPa)
0
100
200
300
400
500
0
50
100
150
200
250
300
350

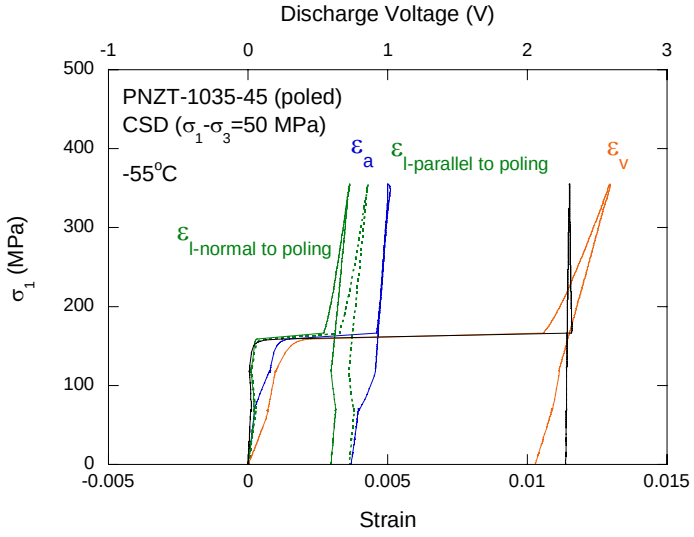
Discharge Voltage (V)
PNZT-1035-45 (poled)
CSD (σ1-σ3=50 MPa)
-55°C
εa
εl-parallel to poling
εv
εl-normal to poling
σ1 (MPa)
Strain
-1
0
1
2
3
-0.005
0
0.005
0.01
0.015

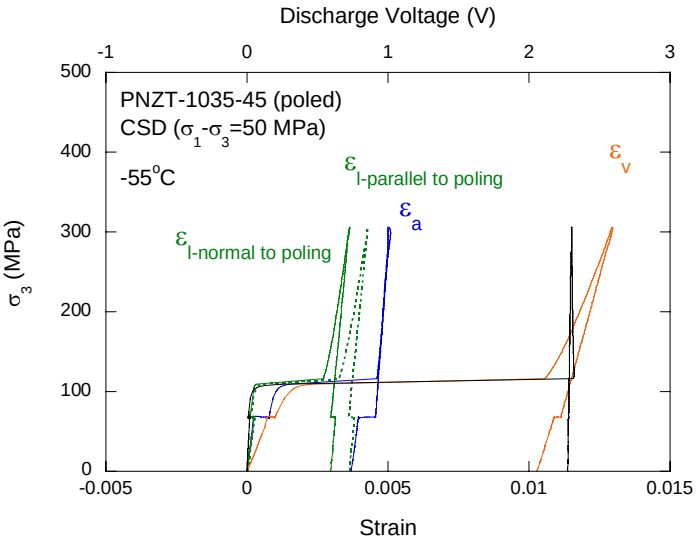
Discharge Voltage (V)
PNZT-1035-45 (poled)
CSD (σ1-σ3=50 MPa)
-55°C
εl-parallel to poling
εv
εa
εl-normal to poling
σ3 (MPa)
Strain
-1
0
1
2
3
-0.005
0
0.005
0.01
0.015

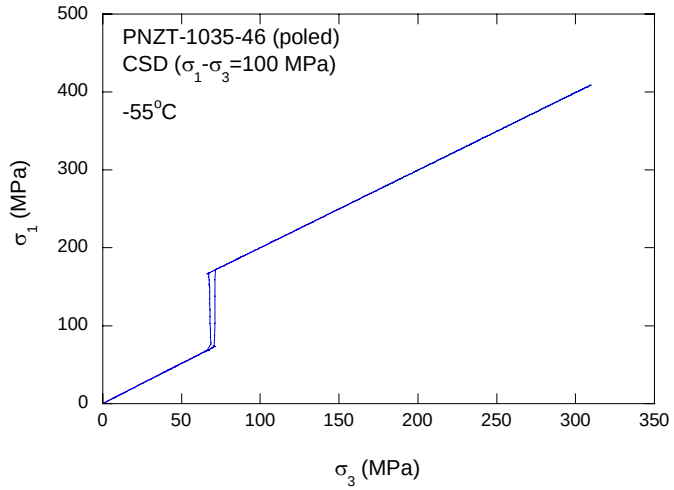
PNZT-1035-46 (poled)
CSD (σ1-σ3=100 MPa)
-55°C
σ1 (MPa)
σ3 (MPa)
0
100
200
300
400
500
0
50
100
150
200
250
300
350

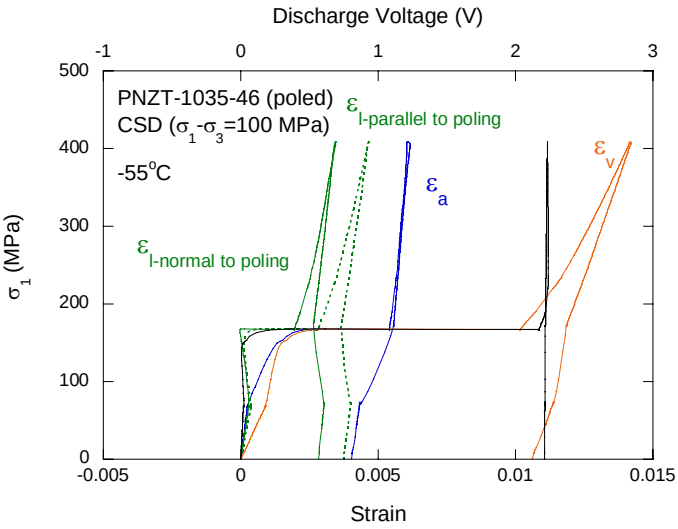
Discharge Voltage (V)
PNZT-1035-46 (poled)
CSD (σ1-σ3=100 MPa)
-55°C
εl-parallel to poling
εa
εv
εl-normal to poling
σ1 (MPa)
Strain
-1
0
1
2
3
0
100
200
300
400
500
-0.005
0
0.005
0.01
0.015

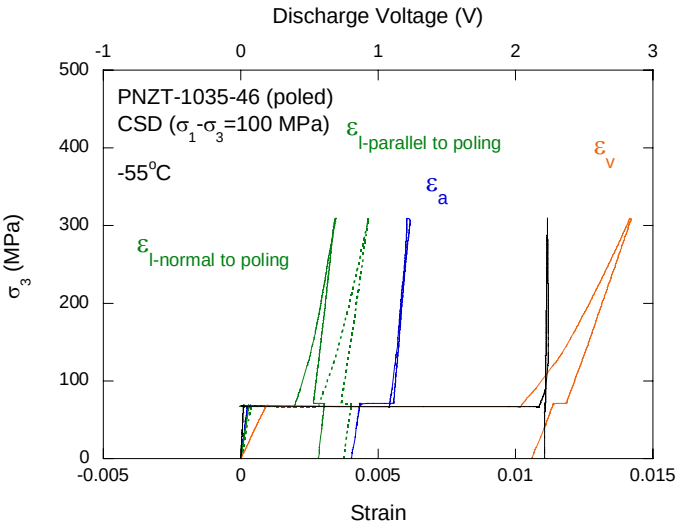
Discharge Voltage (V)
PNZT-1035-46 (poled)
CSD (σ1-σ3=100 MPa)
-55°C
εl-parallel to poling
εa
εv
εl-normal to poling
σ3 (MPa)
Strain
-1
0
1
2
3
0
100
200
300
400
500
-0.005
0
0.005
0.01
0.015

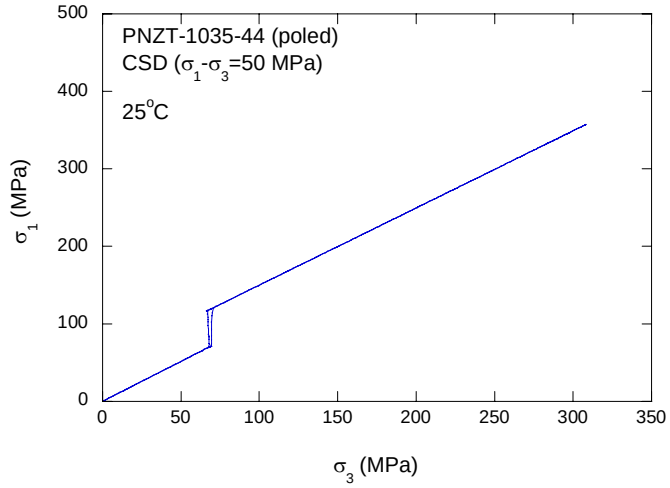
PNZT-1035-44 (poled)
CSD (σ1-σ3=50 MPa)
25°C
σ1 (MPa)
σ3 (MPa)
0
100
200
300
400
500
0
50
100
150
200
250
300
350

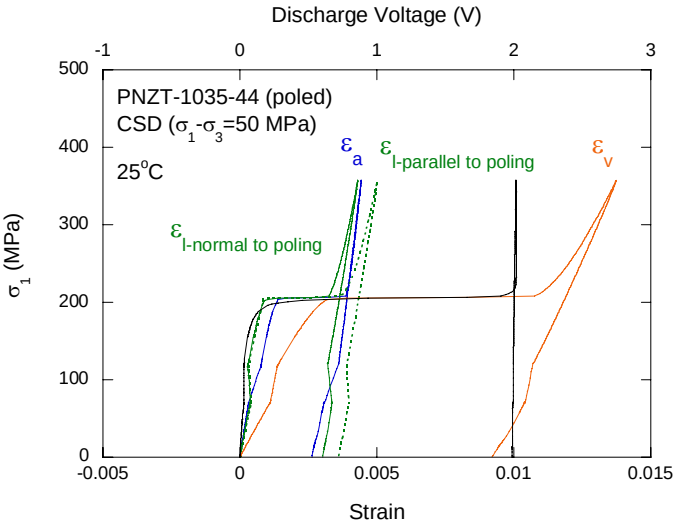
Discharge Voltage (V)
PNZT-1035-44 (poled)
CSD (σ1-σ3=50 MPa)
25°C
εa
εl-parallel to poling
εv
εl-normal to poling
σ1 (MPa)
Strain
-1
0
1
2
3
-0.005
0
0.005
0.01
0.015

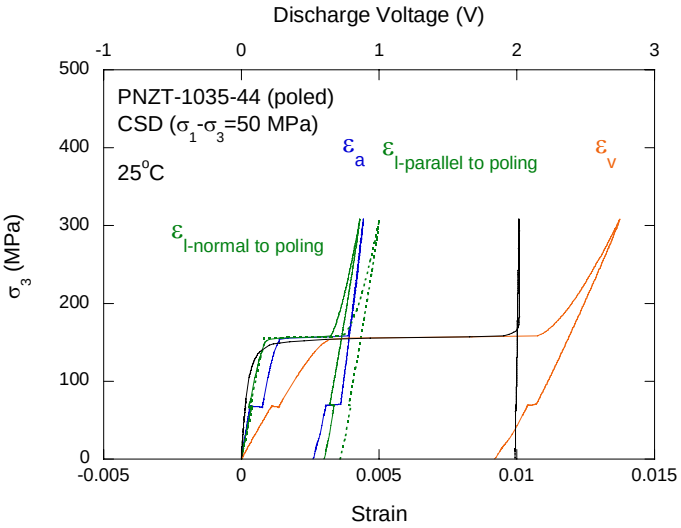
Discharge Voltage (V)
PNZT-1035-44 (poled)
CSD (σ1-σ3=50 MPa)
25°C
εa
εl-parallel to poling
εv
εl-normal to poling
σ3 (MPa)
Strain
-1
0
1
2
3
-0.005
0
0.005
0.01
0.015

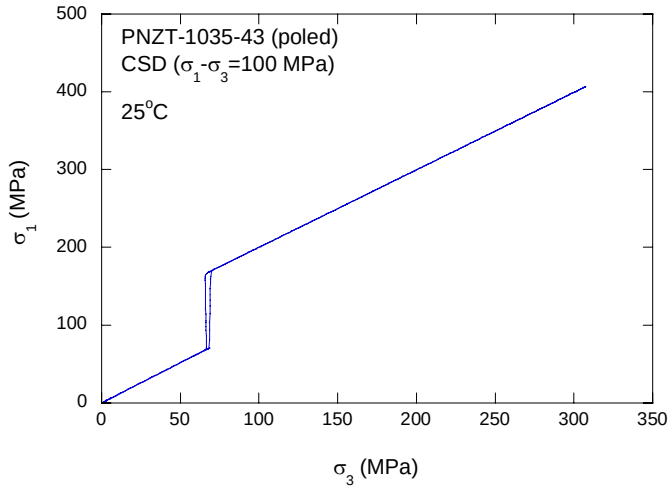
PNZT-1035-43 (poled)
CSD (σ1-σ3=100 MPa)
25°C
σ1 (MPa)
σ3 (MPa)
0
100
200
300
400
500
0
50
100
150
200
250
300
350

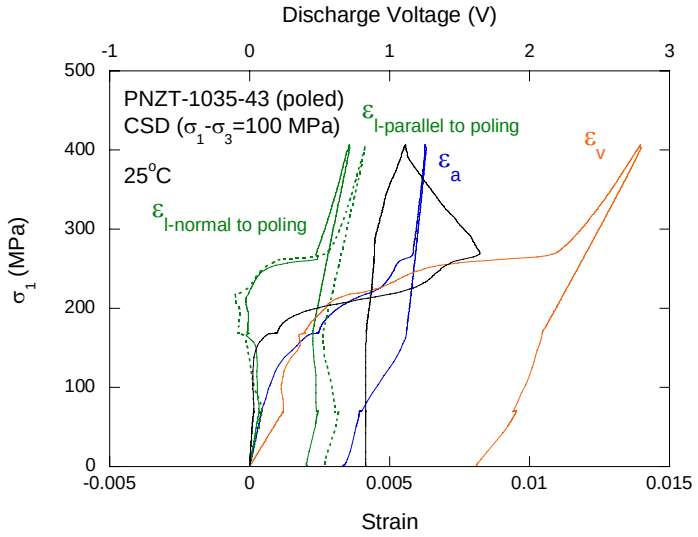
Discharge Voltage (V)
PNZT-1035-43 (poled)
CSD (σ1-σ3=100 MPa)
25°C
εl-parallel to poling
εa
εv
εl-normal to poling
σ1 (MPa)
Strain
-1
0
1
2
3
-0.005
0
0.005
0.01
0.015

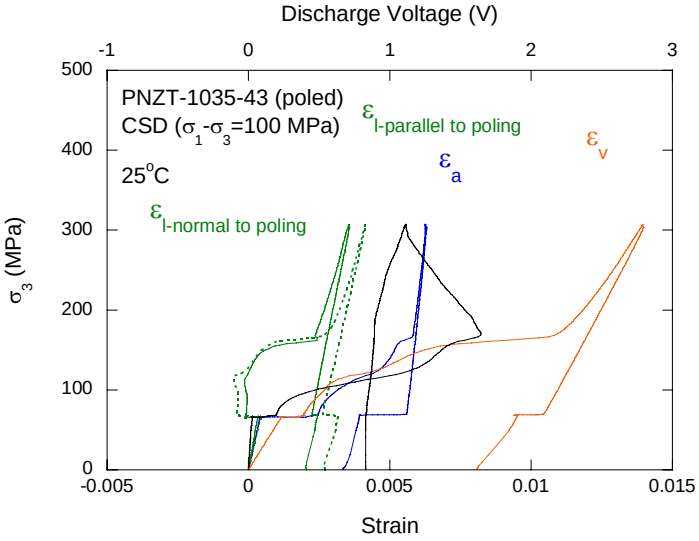
Discharge Voltage (V)
PNZT-1035-43 (poled)
CSD (σ1-σ3=100 MPa)
25°C
εl-parallel to poling
εa
εv
εl-normal to poling
σ3 (MPa)
Strain
-1
0
1
2
3
-0.005
0
0.005
0.01
0.015

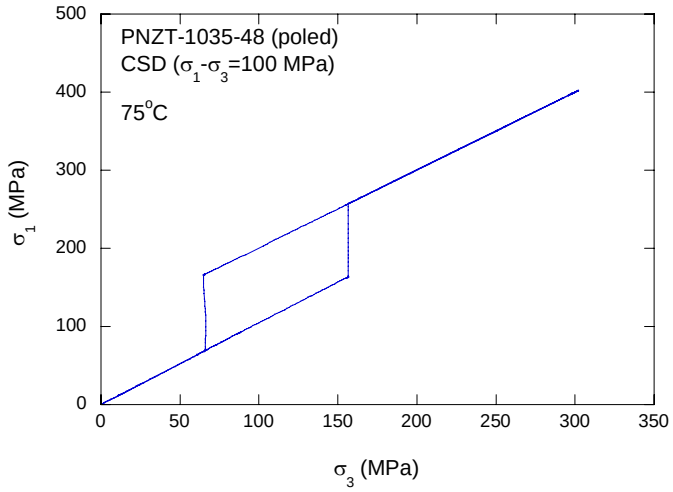
PNZT-1035-48 (poled)
CSD (σ1-σ3=100 MPa)
75°C
σ1 (MPa)
σ3 (MPa)
0
100
200
300
400
500
0
50
100
150
200
250
300
350

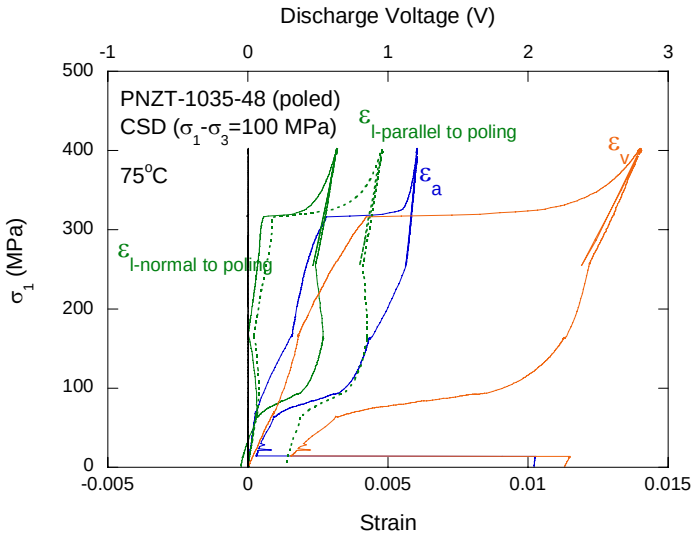
Discharge Voltage (V)
PNZT-1035-48 (poled)
CSD (σ1-σ3=100 MPa)
75°C
εl-parallel to poling
εa
εv
εl-normal to poling
σ1 (MPa)
Strain
-1
0
1
2
3
-0.005
0
0.005
0.01
0.015

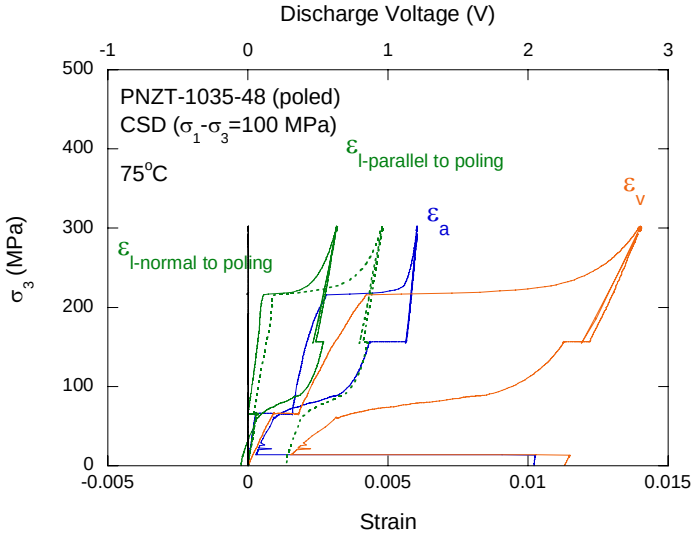
Discharge Voltage (V)
PNZT-1035-48 (poled)
CSD (σ1-σ3=100 MPa)
75°C
εl-parallel to poling
εa
εv
εl-normal to poling
σ3 (MPa)
Strain
-1
0
1
2
3
-0.005
0
0.005
0.01
0.015

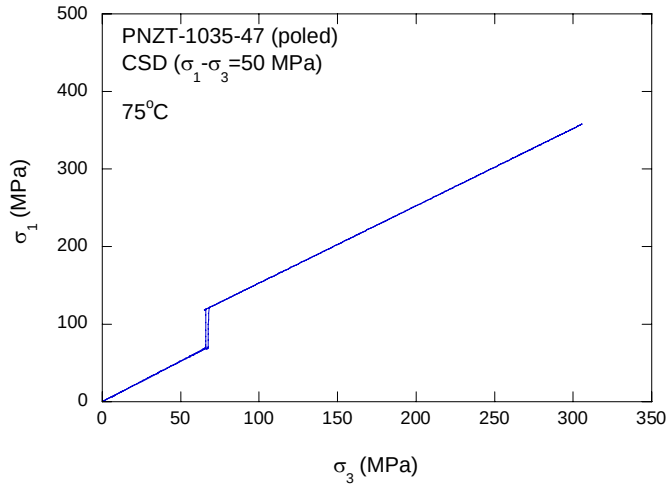
PNZT-1035-47 (poled)
CSD (σ1-σ3=50 MPa)
75°C
σ1 (MPa)
σ3 (MPa)
0
100
200
300
400
500
0
50
100
150
200
250
300
350

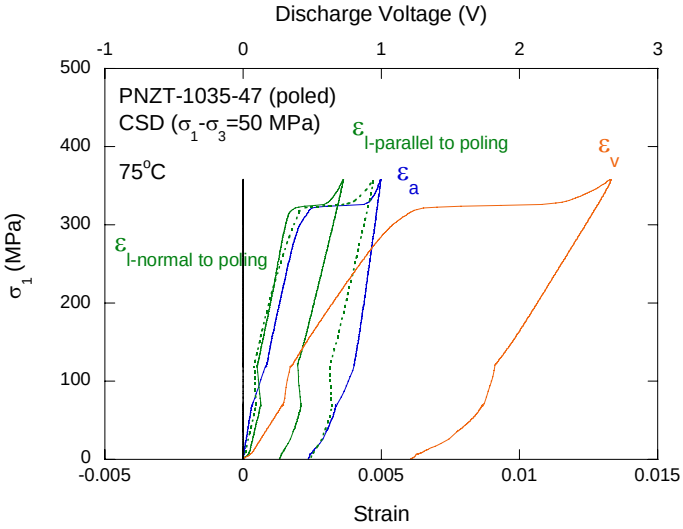
Discharge Voltage (V)
PNZT-1035-47 (poled)
CSD (σ1-σ3=50 MPa)
75°C
εl-parallel to poling
εa
εv
εl-normal to poling
σ1 (MPa)
Strain
-1
0
1
2
3
0
100
200
300
400
500
-0.005
0
0.005
0.01
0.015

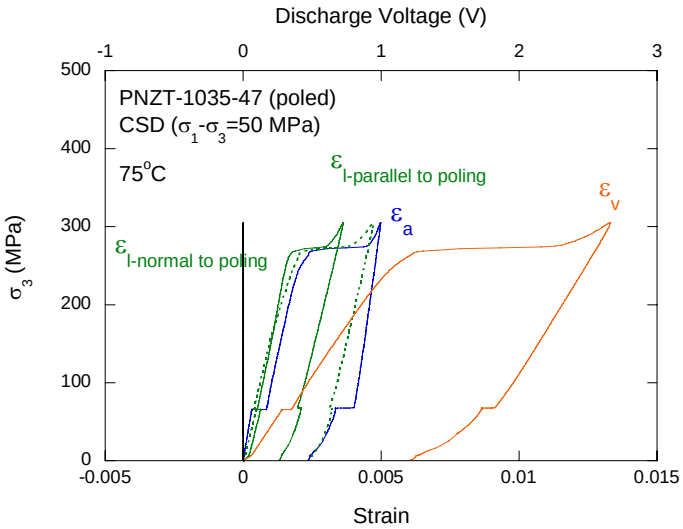
Discharge Voltage (V)
PNZT-1035-47 (poled)
CSD (σ1-σ3=50 MPa)
75°C
εl-parallel to poling
εa
εv
εl-normal to poling
σ3 (MPa)
Strain
-1
0
1
2
3
0
100
200
300
400
500
-0.005
0
0.005
0.01
0.015

DISTRIBUTION

Sandia National Laboratories
P.O. Box 5800
Albuquerque, NM 87185

1	MS 0868	K. G. McCaughey, 2700
1	MS 0871	C. L Renschler, 2720
1	MS 0335	J. P. Brainard, 2720
1	MS 0521	R. A. Damerow, 2720
1	MS 0869	M. A. El, 2722
1	MS 0867	M. O. Eatough, 2725
1	MS 0867	J. F. Browning, 2725
1	MS 0335	B. H. Cole, 2725
1	MS 0335	J. M. Elizando-Decanini, 2725
1	MS 0867	L. I, Espada, 2725
1	MS 0867	R. M. Ferrizz, 2725
5	MS 0335	S. T. Montgomery, 2725
1	MS 0335	T. W. Scofield, 2725
1	MS 0378	J. Robbins, 1435
1	MS 0512	T. E. Blejwas, 2500
1	MS 0515	L. A. Paz, 2723
1	MS 0515	C. A. Busick, 2723
1	MS 0515	E. B. Duckett, 2723
1	MS 0515	T. A. Haverlock, 2723
1	MS 0515	R. J. Stiers, 2723
1	MS 0515	B. J. Wells, 2723
1	MS 0527	E. P. Royer, 2724
1	MS 0527	S. C. Hwang, 2724
1	MS 0701	P. J. Davies, 6100
1	MS 0735	S. A. McKenna, 6115
1	MS 0751	R. M. Brannon, 6117
1	MS 0751	L. S. Costin, 6117
1	MS 0751	D. J. Holcomb, 6117
5	MS 0751	M. Y. Lee, 6117
1	MS 0751	T. W. Pfeifle, 6117
1	MS 0834	J. S. Lash, 1514
1	MS 0834	L. A. Mondy, 1514
1	MS 0834	R. R. Roa, 1514
1	MS 0828	M. Pilch, 1533
1	MS 0888	D. B. Adolf, 1821
1	MS 0889	J. S. Glass, 1825
1	MS 1181	J. L. Wise, 1646
1	MS 1181	L. C. Chhabildas, 1647
1	MS 1181	M. D. Furnish, 1647
1	MS 1245	T. J. Gardner, 2454

1	MS 1245	S. J. Lockwood, 2454
1	MS 1245	R. H. Moore, 2454
1	MS 1245	P. Yang, 2454
1	MS 1245	C. S. Watson, 2454
1	MS 1421	M. U. Anderson, 1111
1	MS 1421	R. E. Setchell, 1111
2	MS 9018	Central Tech. Files, 8944
2	MS 0899	Technical Library, 4536
2	MS 0731	823/Library, 6850

P.O. Box 808
Livermore, CA 94551

Roger Logan, L-25

Los Alamos National Laboratory
P.O. Box 1663
Los Alamos, NM 87545

Bill Bearden MS F602
Steve Girrens, ESA-EA, P946
Dick Macek MS P946

Kevin C. Greenaugh
Department of Energy/Defense Programs
Director, Division of System Simulation & Validation
1000 Independence Ave., SW
Washington DC 20585

Bill-Roy Harrison
Department of Energy/Defense Programs
Program Manager, Weapons Systems Engineering Certification Campaign
19901 Germantown Rd
Germantown, MD 20874

Diane Bird
Weapons Assessments and Development
Supervisory General Engineer
1000 Independence Ave.
NA-115.1
Washington DC 2058

Sandia National Laboratories